University of Southampton

Faculty of Engineering and Physical Sciences

School of Engineering

Mechatronics Group

A Hybrid Energy Storage System comprising a Small-Scale Compressed air Energy Storage System and a Battery

By

Phaisan Omsin

Thesis for the degree of Doctor of Philosophy

November 2020

University of Southampton
<u>Abstract</u>
Faculty of Engineering and Physical Sciences
Mechatronics Group
<u>Doctor of Philosophy</u>
A HYBRID ENERGY STORAGE SYSTEM COMPRISING A SMALL-SCALE COMPRESSED AIR ENERGY STORAGE SYSTEM AND A BATTERY
by
Phaisan Omsin

The thesis investigates the control and component sizing of a stand-alone hybrid alternative energy storage system (HES) comprising a small-scale compressed air energy storage (SS-CAES) and a battery for renewable energy application such as a photovoltaic (PV) system. These systems can be considered as an eco-friendly power generation system since both energy source and storage systems have the benefit of having a small environmental footprint.

The thesis starts with developing the simulation models of an SS-CAES system and its maximum power point tracking (MPPT) controller. MPPT speed controller was designed by using state-space averaging and small signal analysis. The controller was also compared with a maximum efficiency tracking (MEPT) controller. The results show that the maximum power point (MPP) is close to the maximum efficiency point and the loss of efficiency is small around 1-3%. But the MPP is much easier to implement and less sensitive to parameter uncertainty.

The MPPT controller shows a good performance to control the SS-CAES operating at the MPP. However, the SS-CAES has a very narrow maximum efficiency peak. A significant drop of efficiency results from a small deviation from the MPP. The battery was added to resolve this issue by buffering fast load changing while enabling the SS-CAES to operate at the MPP. A bidirectional converter is used to connect the battery to the load and maintain a constant output voltage; a cascaded PI voltage controllers is used. The SS-CAES combining with the battery is so called the hybrid system. The hybrid system is compared to a SS-CAES only system in constant voltage mode. The output power of the proposed hybrid system is matched with the load demand perfectly and the output voltage reaches the reference faster than one of the SS-CAES. By using the MPPT controller, the efficiency of the SS-CAES in hybrid system is greater than that in voltage mode.

A typical house in the Southern region of the UK is used as a case study to determine the component's sizes of the HES and PV systems under two scenarios: the HES only system supplies the power to the load demand for a day and the HES system connected in parallel to the PV system supplies the power to the load demand. A sizing method is proposed by using the difference between the generated and demand powers during a day. The criteria is that the excess energy is greater than the deficit one. For the HES only system supplies the power to the load demand, the difference of total excess and deficit energies is considered to determine the power rate of the air motor which is available in commercial companies, while the battery size is estimated from the deficit. The results show that the 270 W of the air motor and the 1500 Whr-battery were the selected sizes, which generate sufficient power for this demand and meet the criteria.

For another scenario, the sizing method mentioned above is used to determine the components' sizes of the whole system. 41 PV panels are the selected number, which provide the total excess energy greater than the deficit one while it supplies the load demand. The excess energy is stored in the 2.8 m^3 air tank within 7 hour at 20 bar by the 720 W of compressor. The deficit one is used to determine the air motor size, which is used when the PV is unavailable. The 353.8 W of the air motor is selected to supply to the load for 17 hours. In case of peak demand, the 900 Whr-battery is required since the PV and CAES system are unable to meet the load. The sizing method developed in this work can be used as the guideline for other load profile, e.g. the shop or office building.

Table of Contents

List of Tables

List of Figures

List of Figures

List of Figures

x

Research Thesis: Declaration of Authorship

Print name: PHAISAN OMSIN

Title of thesis: A HYBRID ENERGY STORAGE SYSTEM COMPRISING A SMALL-SCALE COMPRESSED AIR ENERGY STORAGE SYSTEM AND A BATTERY

I declare that this thesis and the work presented in it are my own and has been generated by me as the result of my own original research.

I confirm that:

1. This work was done wholly or mainly while in candidature for a research degree at this University;
2. Where any part of this thesis has previously been submitted for a degree or any other qualification at this University or any other institution, this has been clearly stated;
3. Where I have consulted the published work of others, this is always clearly attributed;
4. Where I have quoted from the work of others, the source is always given. With the exception of such quotations, this thesis is entirely my own work;
5. I have acknowledged all main sources of help;
6. Where the thesis is based on work done by myself jointly with others, I have made clear exactly what was done by others and what I have contributed myself;
7. Parts of this work have been published as: [please list references below]:

A hybrid SS-CAES System with a Battery, in *ECTI-CON 2019*, 2019, pp. 3–6.

Control and Sizing of a Hybrid Battery and Compressed Air Energy Storage system, in *SPIES 2020*, 2020, pp. 193-198.

Signature…………………………………………………………………Date………………11/11/2020………….

Acknowledgements

First of all, I would like to express my gratitude to my PhD supervisors, Professor Suleiman M. Sharkh and Dr Mohamed Moshrefi-Torbati for their enormous patience, guidance, support and encouragement during the period of my PhD career. Without them, I could not find the correct way and could not improve the research skills for becoming a good researcher.

I am also grateful to Dr Vorrapath Kokaew who has guided me about his research and given me some examples to do so for gaining my knowledge in this research area.

I would like to thank Royal Thai Navy who gave me the great opportunity and their financial support throughout the PhD career. Without their support, this research could not be done.

I would also like to thank my friends: Prin, Sarawuth, Natchalee and Wetarin's family for their support in the delightful atmosphere for my UK's life.

Finally, I could not finish my PhD without my family's support. I would like to thank my parents, lovely wife and daughter. They watched me from a distance while I have been working to achieve the goal. They deserve a massive thanks for their patience, understanding, and encouragement. I would like to dedicate this project to my lovely family.

Symbols and Abbreviations

Symbols

B_t .... Total viscous friction coefficient

C_o .... Capacitance

C_p .... Specific heat at constant pressure

C_v .... Specific heat at constant volume

D .... Duty cycle

e_{ag} .... Back electromagnetic force

ED .... Energy deficit

ED_a .... Energy deficit for selecting the air motor size

ED_b .... Energy deficit for battery size

EDF .... Energy difference

E_{dif} .... Deficit energy

E_{ex} .... Excess energy

E_g .... Band gap for silicon

f_s .... Switching frequency

G .... Solar irradiance

G_{id} .... Transfer function of the duty cycle-to-inductor current

G_{ig} .... Transfer function of the input voltage-to-inductor current

G_{iv} .... Transfer function of the output voltage-to-inductor current

G_{ref} .... Reference solar irradiance

G_{vd} .... Transfer function of the duty cycle-to-output voltage

H_f .... Digital low pass filter

i_{ag} .... Generator's armature current

I_b .... Battery current

I_{bref} .... Battery current reference

Symbols and Abbreviations

I_{ch} .... Charging current

I_d .... Junction diode current

I_{disch} .... Discharging current

I_L .... Inductor's current

I_{RS} .... Reverse saturation current

I_{ph} .... Photovoltaic current

I_{ref} .... Current reference

I_s .... Saturation current of the diode

I_{sc} .... Short-circuit current

I_{sh} .... Shunt current

J_t .... Combined moment of inertia of the air motor and generator

k .... Boltzmann's constant

K_I .... Short-circuit current temperature coefficient

K_e .... Generator's torque constant

K_m .... Back emf constant

L .... Inductance

m .... Mass of air

M_v .... DC voltage conversion gain

n .... Ideality factor of the diode

P .... Pressure

P_{am} .... Mechanical power

P_{batt} .... Power stored by the battery

P_{CAES} .... Generated power by the CAES

P_{dem} .... Demand power

P_{diff} .... Power difference

P_{fc} .... Mechanical loss

p_i .... Variable pressure

P_{pv} .... Power of the PV

q .... Electron charge

R .... Specific gas constant

r_{ag} .... Generator's armature resistance

R_L .... Resistive load

T .... Temperature

T_0 .... Stall torque

T_{am} .... Mechanical torque

T_{eg} .... Load torque

T_{ref} .... Reference temperature

T_{sc} .... Sampling period

V .... Volume of air

V_o .... Converter's output power

V_{oc} .... Open-circuit voltage

V_{ref} .... Voltage reference

V_T .... Thermal voltage

$\dot{V}_a$ .... Air consumption

$\dot{V}_{max}$ .... Maximum air consumption

W .... Work done by the system

η .... Efficiency of the converter

η_{am} .... Efficiency of the air motor

η_c .... Compressor efficiency

η_{pv} .... Efficiency of the PV module

ω_r .... Rotational speed

ω_{r0} .... Free speed

ω_{ref} .... Speed reference

ΔI_L .... Peak-to-peak inductor current ripple

ΔV_o .... Peak-to-peak output voltage ripple

γ .... Isentropic exponent

Abbreviations

AA-CAES .... Advanced adiabatic compressed air energy storage

A-CAES .... Adiabatic compressed air energy storage

AIC... Absorbed and injected current method

CAES .... Compressed air energy storage

CAES-AI .... CAES system with air injection

CAES-AI-BCE .... CAES-AI with bottoming cycle air expander

CAES-AI-HPE......................... CAES-AI with the HP air expander

C-HyPES................................ Closed cycle hydro pneumatic energy storage

CV.. Constant voltage

E$_{Charged}$................................. Charged energy

E$_{Discharged}$.............................. Discharging energy

EES .... Electrical energy storage

ESS .... Energy storage system

HES.. Hybrid energy storage

HP.. High pressure

ICAES .... Isothermal compressed air energy storage

INC .... Incremental conductance

KCL .... Kirchhoff's current

KVL .... Kirchhoff's voltage

LP .... Low pressure

MEP....................................... Maximum efficiency point

MEPT..................................... Maximum efficiency point tracking

MPP....................................... Maximum power point

MPPT..................................... Maximum power point tracking

OCAES .... Ocean compressed air energy storage

O-HyPES ....Open cycle hydro-pneumatic energy storage

P&O ....Perturb and observe

PM DC ....Permanent magnet direct current

PV ....Photovoltaic

PWM ....Pulse-width modulation

RWE.....................................Renewable energy

SS-CAES ....Small-scale compressed air energy storage

TES.......................................Thermal energy storage

TRU......................................Thermal recovery unit

UWCAES ....Underwater compressed air energy storage

ZOH ....Zero-order hold

Chapter 1 **Introduction**

1.1 Problem Statement

A large-scale compressed air energy storage (CAES) is considered as a mature energy storage technology, which has been operating for many years. Compressed air is stored in underground caverns by compressors. Then, it is released through a turbine to generate electricity at MW-size, depending on demand. The diagram of a CAES system, which was used in commercial plants such as the McIntosh power plants is shown in Fig. 1.1 [1]. The air is compressed by two compressor states and injected into the cavern. The cooling system is used to reduce the temperature of the compressed air to improve the efficiency. For the expansion process, the compressed air is heated before it passes through the turbines connected to the electrical generator. Moreover, waste heat is recuperated to reduce the environment impact [2], [3]. However, combusting fossil fuel leads to the greenhouse gas emission.
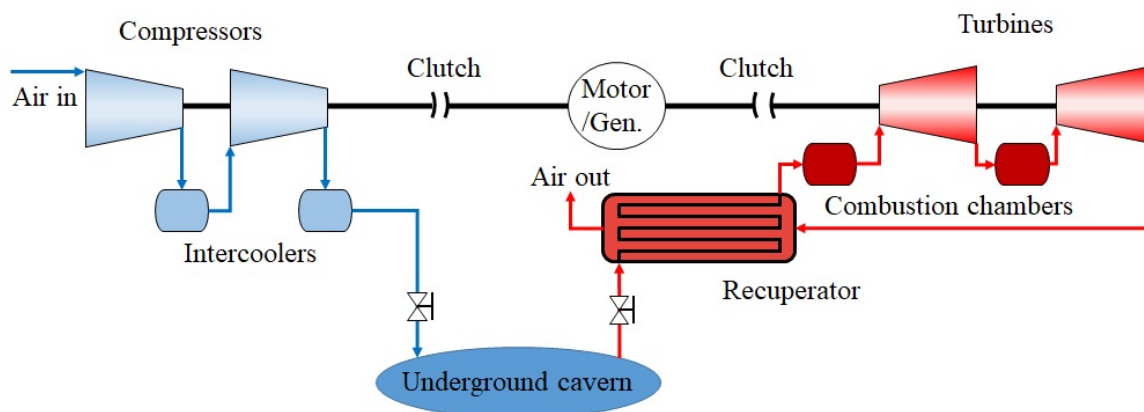
Figure 1.1 Overview of a traditional CAES [1]

Beside, small-scale compressed air energy storage (SS-CAES) systems have been developed for stand-alone applications. It is different from the large scale CAES in that the air turbine is replaced by an air motor. The governing principles of the system are similar to a large-scale CAES with significant advantage of environmental friendly [4]. It is also a more flexible option that uses the over-ground cylinder with proper size for storing sufficient energy instead of the underground caverns. Although the energy and power densities of the SS-CAES is similar to that of the large-scale CAES, its power level is usually at kW-size, which has much lower power rating and rating capacity shown in Table 1 [1], [5], [6].

	Energy density	Power density	Power rating	Rated capacity
Large CAES	2-6 Wh/l	0.5-2 W/l	110-290 MW	580-2860 MWh
Small CAES	2-6 Wh/l	0.5-2 W/l	0.003-3 MW	0.002-0.01 MWh

Table 1 Comparison of different scale CAES [1], [5]

Various researches on this system have been carried out and published in terms of reducing the environmental impact and improving the efficiency. For example, a thermal energy storage (TES) is used instead of the combustion chamber, e.g., an adiabatic CAES proposed by Bullough et al. [7] as illustrated in Fig.1.2. During the off-peak demand period, electricity is supplied to the motor driving the compressor. Wasted heat from the compression process is captured in a thermal energy storage (TES). In the expansion process, the compressed air is preheated by the TES before it is delivered to the turbine during peak demand periods. This concept design of the CAES eliminates the need for additional fuel resulting in low environmental impact. Since the heat of the compression process is used to reheat the air in the expansion process, The CAES type can have its high cycle efficiency close to 70% [8], [9].
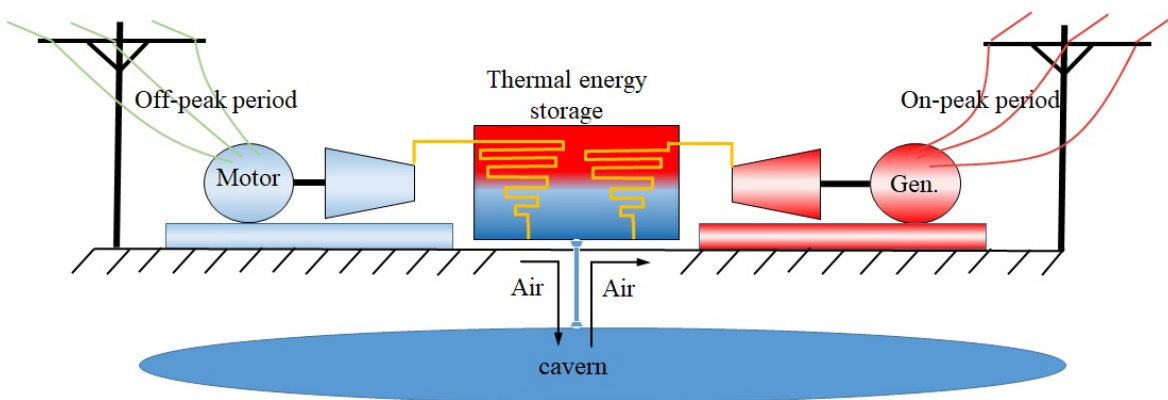
Figure 1.2 Schematic diagram of AA-CAS plant [7]

Alternatively, the water or other liquids were combined into the compression and expansion processes in order to maintain the temperatures of both processes. It is used as a liquid piston or a liquid spray, which increases the surface of the heat exchanger, for speeding up the heat transfer process [8]. The work using this method was proposed by Zhang et al. [10]. A quasi-isothermal expander for the isothermal CAES system was introduced and compared its outcomes with an adiabatic expansion. The model was designed based on adiabatic modelling, which the water droplets were sprayed into the cylinder during the expansion process shown in Fig 1.3. The results presented that the temperature difference between the inlet and outlet of the quasi-isothermal

expander was reduced around 90% of that of adiabatic process. As a result, the specific work increases 15.7% when compared with that of the adiabatic condition.
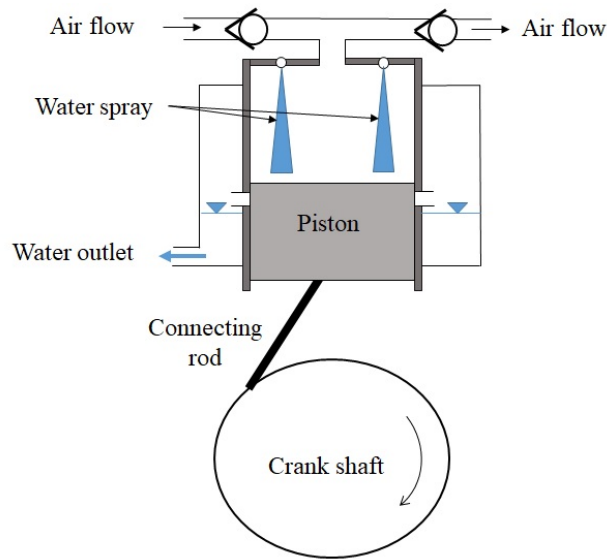
Figure 1.3 Schematic diagram of water spray method of isothermal CAES [10], [11]

Fortunately, an electrical control system can further improve the performance of the system by ensuring that the output power operates at the maximum efficiency point. A significant work using maximum efficiency point tracking (MEPT) for the SS-CAES was carried out by Lemofouet-Gats [12]; on the system shown in Fig. 1.4. The MEPT was designed to control a hydro-pneumatics storage system hybridised with a supercapacitor bank. However, many sensors such as pressure, speed and flow are required for the controller, which is difficult for accurate real time tracking, relying on approximation of losses and models with uncertain parameters.
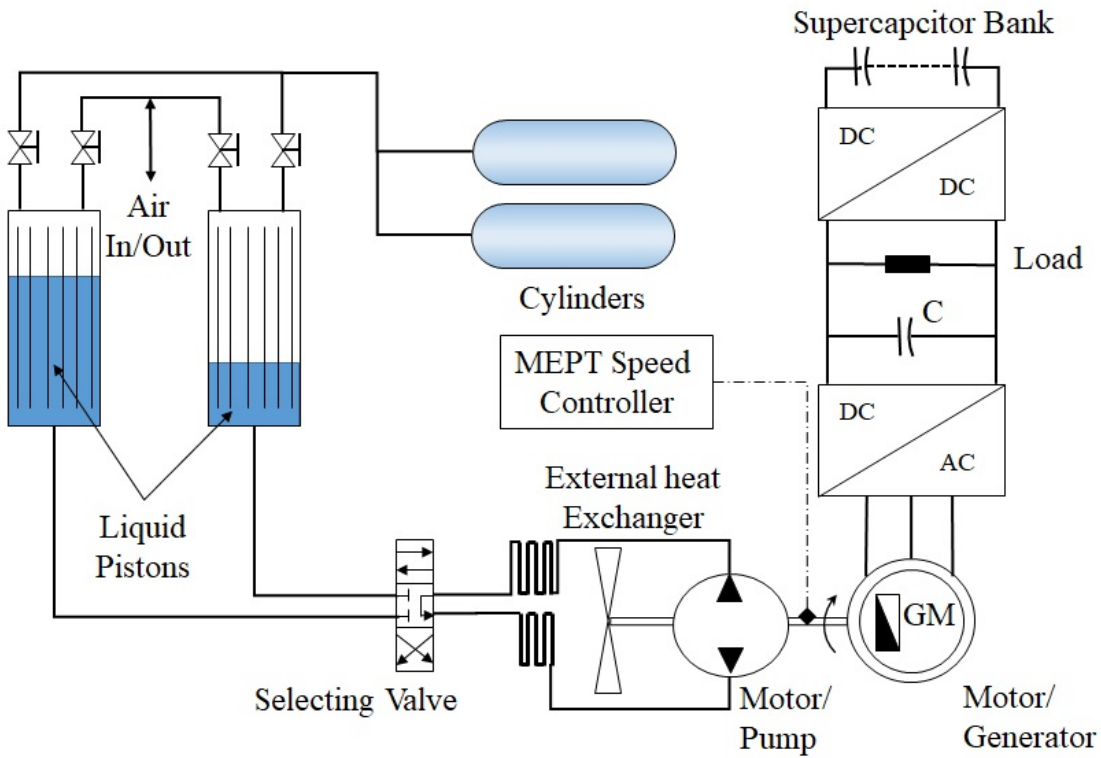
Figure 1.4 Diagram of hybrid, hydro-pneumatics and supercapacitor storage system [12]

Another interesting strategy of the control system is a maximum power point tracking (MPPT). It requires small number of sensors since it measures output power directly resulting in the ease for real time tracking [13]. An interesting work employing the MPPT controlling the SS-CAES system was carried out by Kokaew [14]. A maximum power point tracking (MPPT) and speed controller, which has similar efficiency to that of the MEPT controller for the system was proposed as illustrated in Fig. 1.5. The MPPT controller is designed by using a hybrid perturb and observe (P&O) method to determine the speed operating point of the air motor corresponding to the MPP [4], [13], [14]. This work has been done by carrying out both simulations and experiments, which is assumed under isothermal condition without losses and unlimited air in the storage. The controller was demonstrated to have good performance for real-time tracking of the maximum power. The CAES, however, is slow to react to electrical load changes because it is a mechanical system. It also has a very narrow maximum efficiency peak and a significant drop of efficiency results from a small deviation from the MEPT/MPPT. When it is connected to various load levels, the SS-CAES does not have the potential to resolve these issues leading to lack of power quality. Additionally, the components' sizing were not considered in his study.
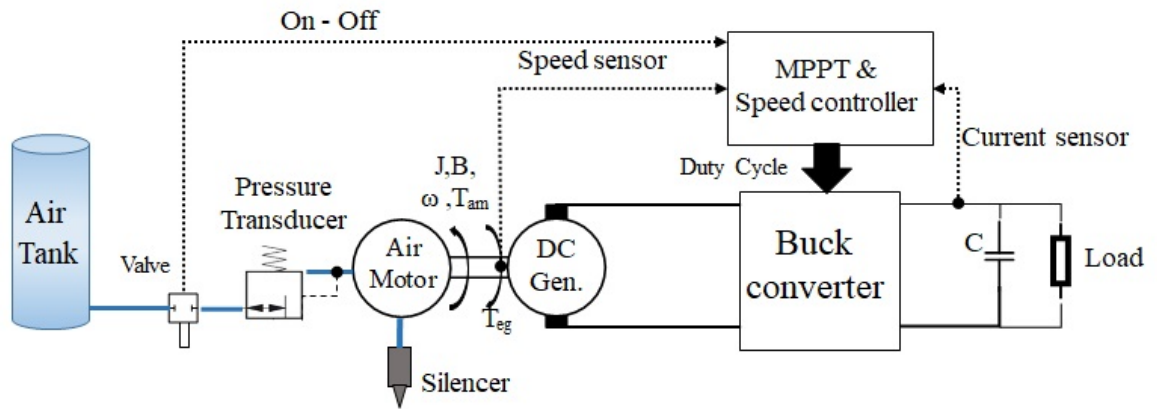
Figure 1.5 SS-CAES system with MPPT speed controller [14]

The air tank size was estimated for the solar home system, which is proposed by Setiawan [15] shown in Fig. 1.6. The photovoltaic (PV) system controlled by the MPPT controller was used to drive the compressor for compressed air into the tank. The air motor and dc generator were selected from the commercial industry. The air tank size was determined to store sufficient energy for running the SS-CAES within the selected backup period. The results showed that the tank size of 18 m^3 is required to store the energy for the load of 30 W within 12 hours, which can be installed in rural area. However, the component size for recharging the SS-CAES, such as the PV system and compressor, were not considered in this study.
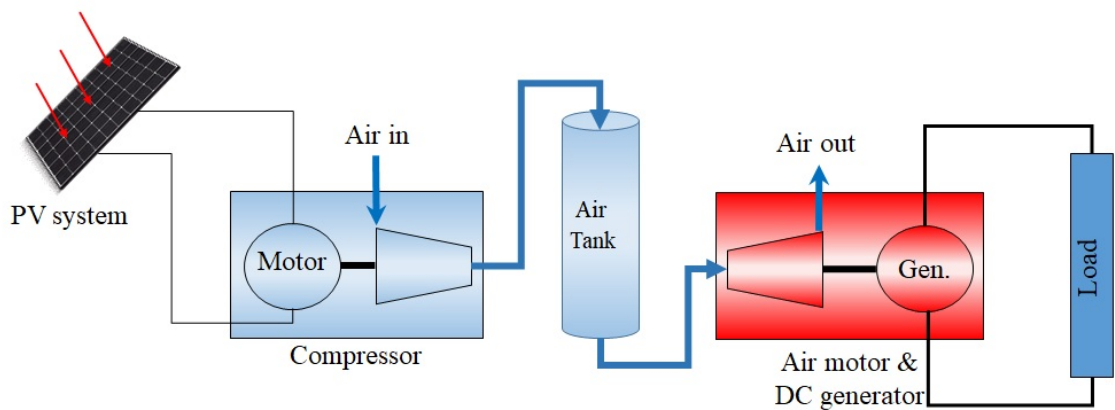
Figure 1.6 Diagram of solar home system with CAES [15]

A study of hybrid system using CAES, which is used for an electric vehicle application, have been proposed by Kucuk et al. [16]. The CAES was modelled by Matlab/Simulink, which acted as an auxiliary source, while the battery model was used in ADVISOR, which served as a main energy source. The performance of an electric vehicle using the hybrid system was compared with that employing only li-on battery. The obtained results illustrated that the CAES system improved the battery SOC from 0.25 to 0.55 for the urban dynamometer drive schedules (UDDS) driving cycle.

The distance that the vehicle can run to also increased. However, the components' size is outside the scope of this study, the tank size was selected and kept constant.

It is clear that using only SS-CAES system with the controller has some issues as mentioned above. The system's performance can be improved by hybridizing with other storage devices such as batteries and supercapacitors. Also, the system's components need to be sized for storing sufficient energy for selected load demand. In this thesis, a hybrid energy storage (HES) system comprising the SS-CAES system and a battery is investigated, as shown in Fig. 1.7. The SS-CAES is used as primary energy source, which operates at the maximum power point, while a battery will resolve the load fluctuation issue, which operates in the constant voltage mode. Moreover, the SS-CAES system is normally integrated with renewable energy technologies such as wind and PV systems for recharging. The system's components, e.g., air tank, air motor, compressor and battery, need to be sized for ensuring sufficient stored energy that is a significant information for the users' interested in implementing this storage system.
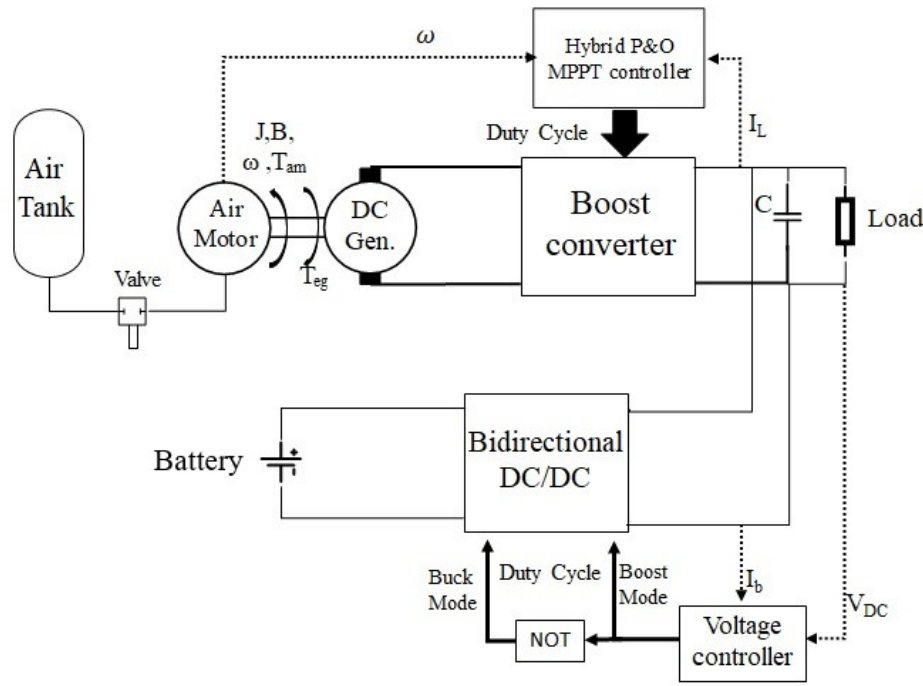
Figure 1.7 Configuration of proposed hybrid energy storage system

1.2   Aims and objectives

The thesis aims to improve the performance of a SS-CAES system by combining it with a battery and hence producing an HES system. The study focuses on the system's implementation, i.e., how to design the hybrid system and how to estimate the system's component sizes. To achieve the goal, the research tasks can be summarised into the following objectives:

1. Develop a SS-CAES system and its MPPT controller. This process focuses on understanding how the system works, how to build the system model and how to design the MPPT controller.

2. To design the HES system based on SS-CAES and a battery in the discharging process. The system is connected to a variable load. The control system of the battery is designed to maintain the output voltage while the SS-CAES is controlled by the MPPT. The component sizes are determined by using the fluctuating load demand in a given household.

3. To design the photovoltaic (PV) system to charge SS-CAES. The PV system is controlled by the MPPT controller. This process focuses on the component sizes of the hybrid system when the generated power is greater than a specific load demand.

4. To design the HES system comprising SS-CAES with a battery connected with the PV system. The process aims to estimate the components sizes for the discharging process such as the air motor and the battery.

1.3   Thesis novel contributions

The novel contributions of this thesis are:

The development of an alternative HES system comprising SS-CAES system with the battery. The SS-CAES model can deal with the fluctuating load demand by employing the battery, which compensates the current to maintain the output voltage under a variable, fluctuating load demand. This work has been published in the following IEEE journal paper.

P. Omsin, S. M. Sharkh and M. Moshrefi-Torbati, "A Hybrid SS-CAES System with a Battery," *2019 16th International Conference on Electrical Engineering/Electronics, Computer, Telecommunications and Information Technology (ECTI-CON)*, Pattaya, Chonburi, Thailand, 2019, pp. 159-162[17] .

A novel sizing method for the HES system in the discharging process that produces component sizes for the energy storage in order to supply sufficient power to a given load demand. This work has been published in the following IEEE journal paper.

P. Omsin, S. M. Sharkh and M. Moshrefi-Torbati, "Control and Sizing of a Hybrid Battery and Compressed Air Energy Storage system," *2020 2nd International Conference on Smart Power & Internet Energy Systems (SPIES)*, Bangkok, Thailand, 2020, pp. 193-198 [18].

A novel sizing method for an alternative combination of a PV system with an HES system comprising SS-CAES and the battery that estimate the component sizes in both charging and discharging processes. The system components are sized properly to match the load demand.

1.4   Thesis structure

This thesis is divided into seven chapters. Chapter 1 is the introduction of this thesis that contains a problem statement, aim and objectives and novel contributions of the research. Chapter 2 is the literature review which presents the developments of the CAES system and hybrid energy storage system. The models of the SS-CAES system and MPPT speed controller are presented in chapter 3. The system is considered in the discharging process supplying power to a constant resistive load that is controlled by the MPPT controller. Chapter 4 presents an HES system comprising SS-CAES system with a battery. The control system of the battery is designed to maintain the output voltage of the system. This work has been published in an IEEE journal paper [17]. Chapter 5 presents the charging process of the SS-CAES system by using the PV system that mainly focuses on the component sizing for a specific load demand. Chapter 6 is concerned with the component sizing of the PV system combined with the HES system in the discharging process, which provides the sufficient power for a selected load demand. The last chapter discusses the conclusions of this work and recommends areas for the future research.

Chapter 2   Literature review

2.1 CAES system

CAES is an interesting energy storage system since it has advantages of being environmentally friendly. CAES is used to convert excess grid electricity into stored pneumatic energy in underground caverns to be discharged later. It consists of six components as shown in Fig. 2.1 [19]: air compressor; generator/motor; turbine train; control unit; auxiliary equipment and containers. The operation of a CAES system has two separated processes of compression and expansion. The compression process occurs when power demand is low and excess electrical energy is stored by compressing air in the pressure vessels or caverns. During the expansion process, the compressed air is released, heated and expanded through turbines coupled to an electrical generator [3].
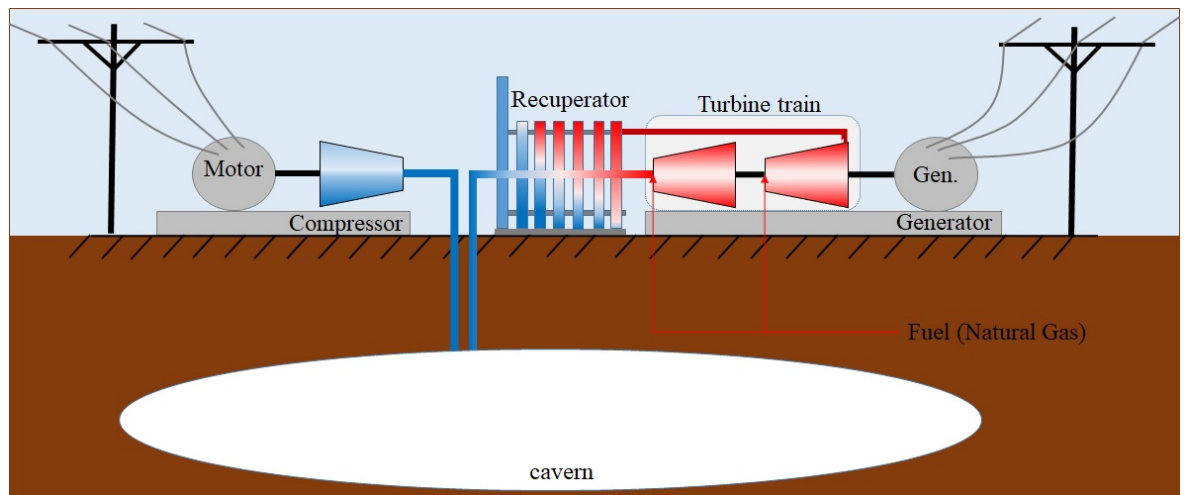
Figure 2.1 Components of a CAES system [19]

In actual applications, the air conversions in both compression and expansion processes are explained based on the thermodynamic theory [20]. These processes can be classified as the adiabatic or isothermal processes.

In the compression process, the compressor converts excess power to pressured air stored in high pressure reservoir [21]. To derive the energy and power expressions, the ideal gas law is used;

$$PV = mRT \tag{2.1}$$

where P is the pressure in Pa, V is the volume of air in m³, m is the mass of air in Kg, R is the specific gas constant in JK/Kg and T is temperature in K.

For the isothermal condition, Eq. (2.1) can be rewritten as

$$PV = \text{Constant} \tag{2.2}$$

Based on thermodynamic theory where the internal work of the system and the temperature change is neglected, the work done by the compressor within isothermal process can be given by

$$W = \int_1^2 PdV = P_1V_1 \ln\frac{P_1}{P_2} \tag{2.3}$$

where P_1 and P_2 are the pressures of the air at atmospheric and storage levels, respectively.

For the adiabatic process, Eq. (2.1) can be rewritten as

$$PV^\gamma = Constant \tag{2.4}$$

where $\gamma = {C_p}/{C_v}$ denotes the isentropic exponent. C_p is the specific heat at constant pressure while C_v denotes the specific heat at constant volume. Using the temperature ratio of the ideal gas $(T_1/T_2) = (p_1/p_2)^{\gamma-1/\gamma}$, the net work done by the compressor within the adiabatic condition is expressed as

$$W = \frac{\gamma}{\gamma-1}P_1V_1\left[\left(\frac{P_2}{P_1}\right)^{\frac{\gamma-1}{\gamma}} - 1\right] \tag{2.5}$$

For the expansion process, the potential work of the air can be calculated by using the same equations of both processes. The initial state of this process is the compressed air state while the final state is the atmospheric state. However, completely adiabatic or isothermal process cannot be found in practice since there is nothing as a perfect insulation or perfect cooling. But both purely adiabatic and isothermal processes are used as upper and lower boundaries of the available energies, respectively.

The investigation and development of the CAES system can be classified into two groups: large-scale; small-scale CAES systems. The details of each group are provided in the following sections.

2.1.1 Large CAES systems

The idea of using CAES system for storing the electrical energy was introduced in the early 1940s [8], [9]. Historically, CAES systems have gone through three major changes resulting in three generations of designs [22].

2.1.1.a 1st generation of large CAES plants

The first generation, which was employed in the commercial section, is the Huntorf CAES project in Hannover, Germany which started to generate electricity since 1978, see Fig. 2.2 [23]. This CAES

plant was used to provide black-start operation for the nuclear unit, which is locate close to the North Sea. It also reduces the peak power demand cost. The plant has two salt caverns with the overall capacity of approximately 310,000 m^3, which has the advantages of redundancy during maintenance/ cavern shut-down and ease of cavern refilling [23]. The compressor of the CAES plant requires a pressure of 13 bar as a minimum pressure for starting up. The charging time to fill these caverns is 8 hours of daily cycle that can generate 290 MW. For the discharging state, it needs a 2.5 minute start-up and operates at the pressure range between 48-66 bar for supporting a nuclear plant and electricity grid for 2 hours [24]. The maintenance of the CAES plant needs only be done for the over-ground components such as valves and the well head since a cavern survey in 2001 revealed that there is no deviation after over 20 years of their service. This plant is claimed to have an excellent performance that guarantees high operational availability of 90% with 99% starting reliability [3], [9]. However, its cycle efficiency is fairly low at approximately 46% since the heat during compression state is released to the environment as waste and the additional heat is required to reheat the air in the expansion process [1], [5], [6].
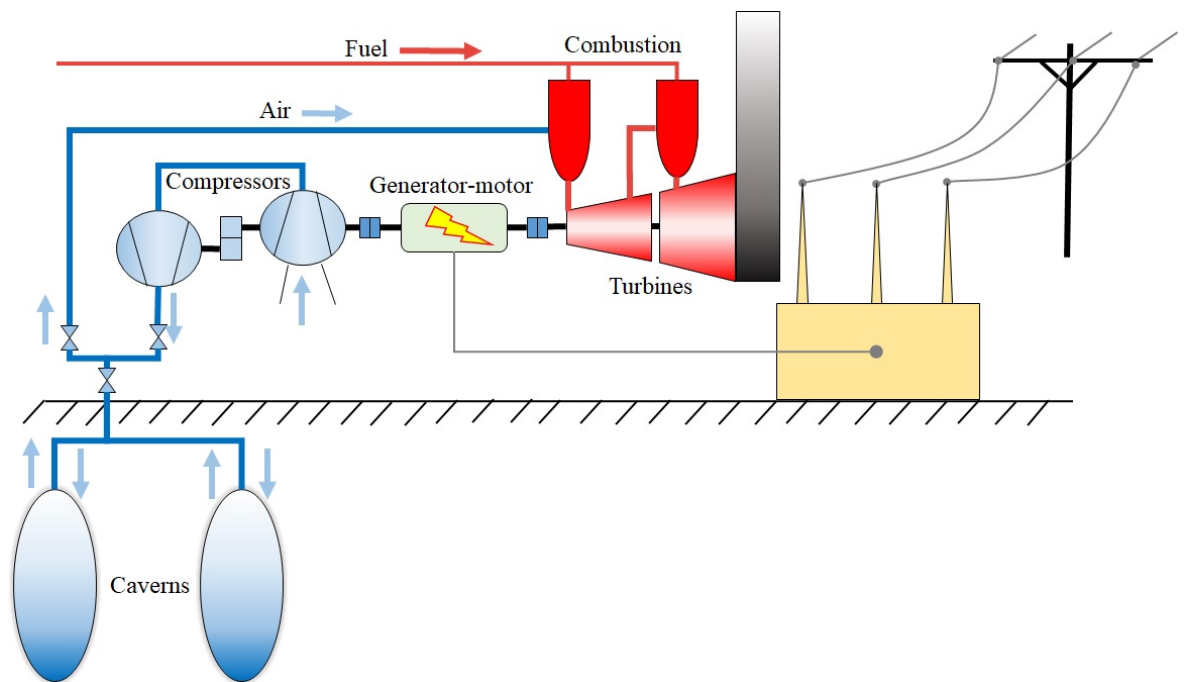
Figure 2.2 Components of the Huntoft CAES plant [23]

2.1.1.b 2nd generation of large CAES plant - *Production* Side Efficiency

The second generation of CAES design is represented by McIntosh, Alabama – USA, which has been in operation since 1991 [1], [3]. This plant has a generating capacity of 110 MW, which can deliver its power continuously for up to 26 hrs. A single salt cavern with a capacity of 500,00 m^3 is employed, which can store the compressed air up to around 74 bar [2], [3], [25]. The production side efficiency is the main consideration in this design. A recuperator preheats the air from the

cavern using the waste heat from the turbines in the charging process. This reduces fuel consumption by around 25% compared to Huntorf [21], [26]. The design can use a heat exchanger in the compression pump, molten salt for heat storage and a heat exchanger in the expansion turbine and between expansion stages. Using the compression heat during the expansion process can increase the efficiency by 10 - 15%. There are many variations on the design of the second generation CAES plants. For example, the concept of the CAES system with air injection (CAES-AI) that was proposed by Nakhamkin et al [27] shown in Fig. 2.3. The design concepts based on the McIntosh plant in which the preheated air is injected in the combustion chamber of the gas turbine to increase the power output. Another example is the CAES-AI with the HP air expander (CAES-AI-HPE) concept [27]. An HP expander is added for matching between the pressure of pre-heated compressed air and inlet pressure of the combustion chamber. This concept can be improved by adding LP expander called CAES-AI with bottoming cycle air expander (CAES-AI-BCE) concept for adjusting the airflow to match the burner operation. This concept allows the turbine to operate at higher temperature and the fuel consumption is decreased by 10% [27], [28].
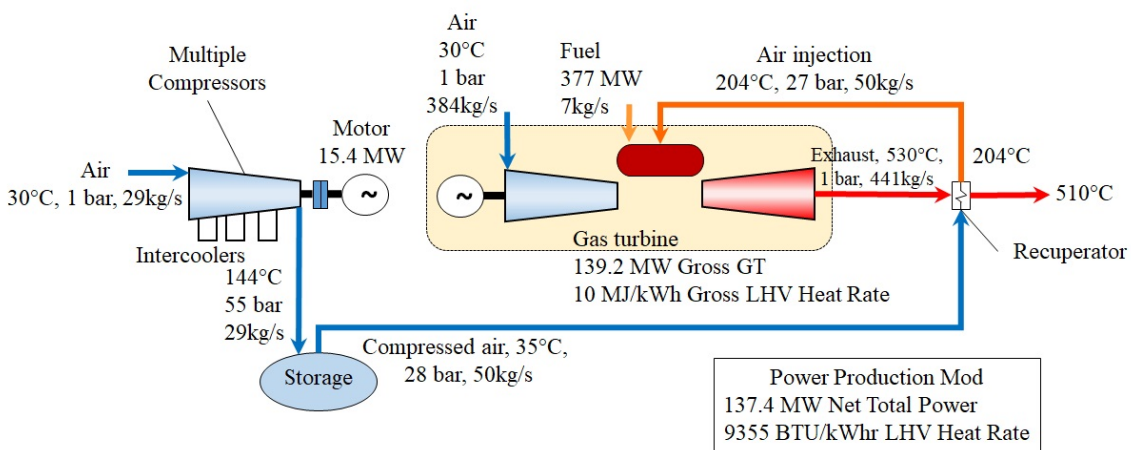
(a) CAES-AI
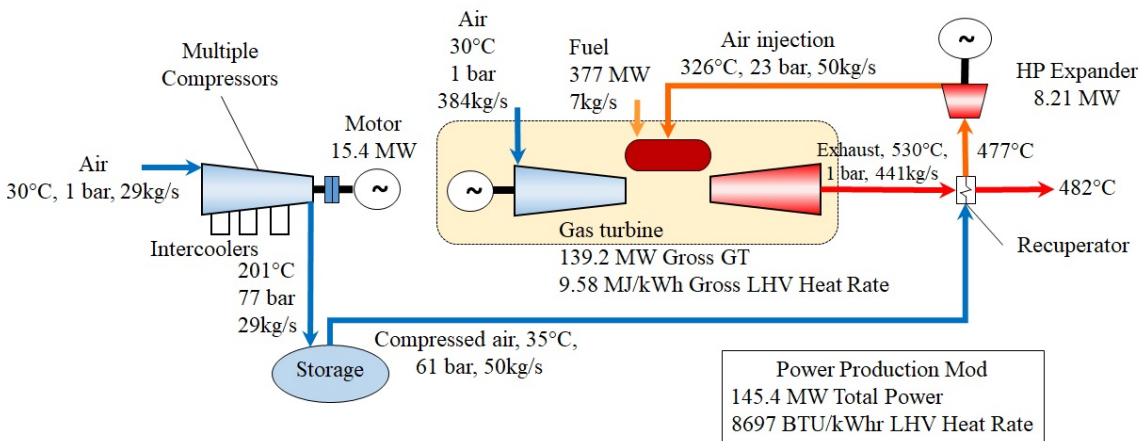
(b) CAES-AI-HPE
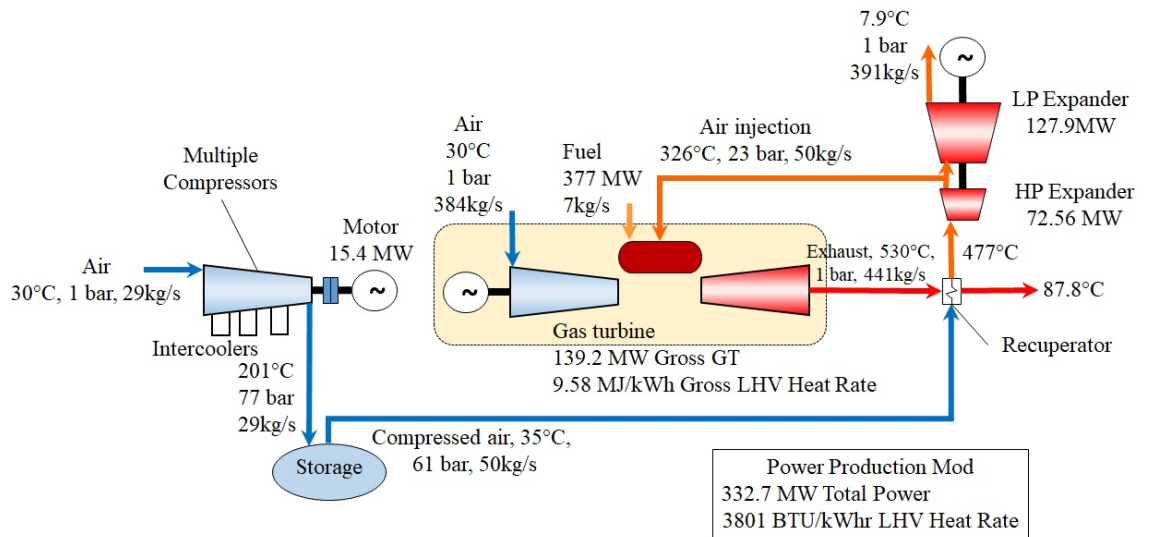
(c) CAES-AI-BCE

Figure 2.3 Schematic of CAES with air injection concept adapt from [27]

2.1.1.c 3rd generation of large CAES plant - Compressed Air *Injection* Side

The third generation of CAES plants makes efficiency improvements by improving the design of the injection (compression) side of the plant. With a special design, a reduction of 25% is also possible and furthermore reductions to 0% natural gas are also possible with adiabatic CAES or isothermal CAES. There are many possible variations but the two extreme designs are Advanced Adiabatic CAES (AA-CAES) and Isothermal CAES (ICAES) [29], [30].

Advanced Adiabatic-CAES (AA-CAES) system has been designed to reduce or eliminate the fuel need by reusing the heating energy from compression process during the expansion operation [29], [31]. In this system, the combustion chamber is replaced by a thermal energy storage system (TES). This leads to the elimination of combustors and consequently the fuel requirement. The main components of AA-CAES system include compressors, TES, underground cavern and turbines [31]. The first demonstration is "ADELE" constructed by RWE Power, General Electric, Zublin and DLR in Stassfurt, Anhalt that apply the concept of advance adiabatic into CAES system as shown in Figure 2.4 [32].
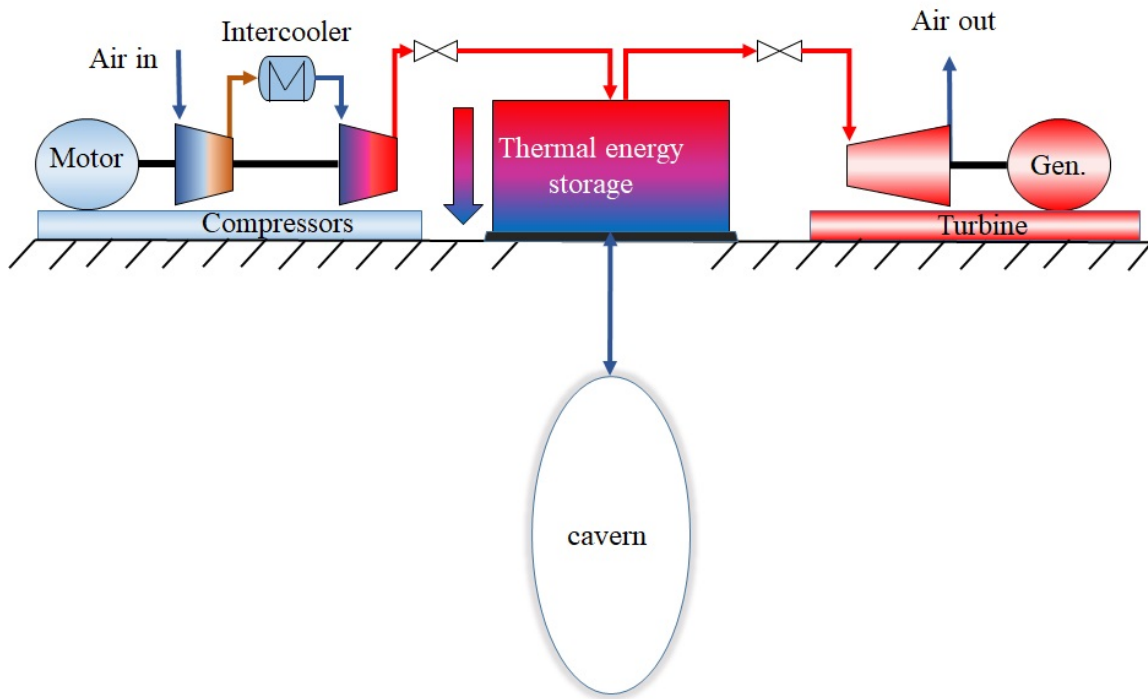
Figure 2.4 System concept of ADELE adiabatic CAES [32]

Isothermal CAES is introduced to overcome some of the challenges with the traditional CAES or adiabatic CAES. The combustor and 'high temperature' heat energy storage are eliminated and both processes of the CAES operate slowly, which results in the improved efficiency of approximate 70% – 80% and a relatively low cost [33]. During the compression process, the air pressure is gradually increased without temperature change by liquid piston with the mean of effective heat transfer, which minimizes the work needed for compression. In the expansion process, the compressed air drives the liquid motor to operate slowly and absorb its surrounding heat, which provides the maximum work [30], [31], [34]. However, it is difficult for a small-scale system since the heat needs to be removed continuously during compression process and added continuously during the expansion process.

2.1.2 Small Scale CAES (SS-CAES) system

2.1.2.a Pure pneumatic SS-CAES

The pure-pneumatic SS-CAES system is a solution with similar principles of operation of that of a large-scale CAES plant without the requirement of underground cavern [4], [12], [14], [35]–[41]. The air is stored in pressure vessels instead of caverns. The power capacity of the SS-CAES is much smaller than that of a large-scale CAES, usually in kW. An air motor is employed in this system rather than using turbines. Pre-heating in the expansion process is sometimes utilized and heat exchangers are also used to achieve isothermal decompression [14]. However, the power density of SS-CAES is low compared to the other small-scale EES systems because they are governed by the same

principles as large-scale CAES systems. The performance of SS-CAES can be improved by integrating it with heat exchangers. The system can increase the conversion efficiency by around 72% when integrated with a TES system [42]. Additionally, an electrical control system can further improve the performance of the system in both the charging and discharging processes. A maximum efficiency point tracking (MEPT) strategy can be used to improve the thermodymics efficiency of the energy conversion, which was investigated in [12], [39], [41], [43]. However, this MEPT requires using a number of sensors. Fortunately, maximum power point tracking (MPPT) is an interesting alternative to MEPT that provides outputs close to it. A perturb and observe (P&O) MPPT controller of a SS-CAES was introduced by Kokaew [4], [14]. The controller has a good performance in terms of real-time maximum power tracking and achieving high efficiency; the efficiency of the MEP is higher than that of the MPP by around 1-3% [17]. For a pure pneumatic storage system, the disadvantages include difficulties in integrating good heat exchangers, losses due to friction and leakage and the low energy storage capabilities [22]. Moreover, since it is a mechanical system, the SS-CAES has a very narrow maximum efficiency peak. A small deviation from the MPPT causes significant loss of efficiency.

2.1.2b Hydro-pneumatic SS-CAES

The hydro-pneumatic SS-CAES system is implemented based on the isothermal concept in which heat is exchanged at the contact between the liquid and air surfaces [9]. The system consists of a motor/generator, a hydraulic pump/motor and two storages. In this system, air is compressed by the liquid and can be divided into two types, namely closed and open cycles.

(a) C-HyPES   (b) O-HyPES
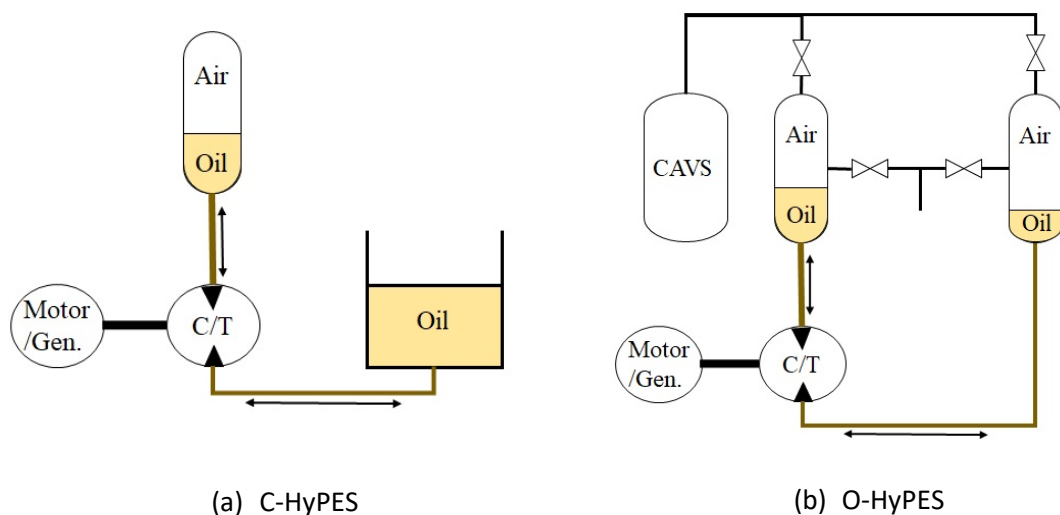
Figure 2.5 Simplified process schemes of hydro-pneumatic energy storage [8]

The closed cycle hydro pneumatic energy storage (C-HyPES) is shown in Fig. 2.5 (a). Oil is pumped into the cylinder resulting in air pressure increase. Then, the air pressure is decreased by releasing the oil in different directions through the turbine or hydraulic motor for driving the generator. This

system is available at laboratory scale since it has low energy density, which is its major drawback [12].

The open cycle hydro-pneumatic energy storage (O-HyPES) shown in Fig. 2.5(b) is used to overcome the disadvantages of the C-HyPES. The system requires at least two cylinders for liquid piston to compress air. Oil flows between these two cylinders via the pump/turbine. The O-HyPES can increase the compression efficiency up to 83% [44]. Nevertheless, the liquid pistons have the surface contact between compressed air and oil, which is used as the heat transfer area. It is limited the powers during the charging and discharging processes since it depends on the container shape. This limitation can be reduced by using a water-spraying method [45]. The temperature rise in the chamber during the charging processes is prevented by droplet spray, which is used to cool down the compressed air [11], [46], [47]. This method also is used at the inlet of the turbine resulting to increase of turbine efficiency [48].

2.1.3 Underwater CAES system

Underwater/ocean CAES (UWCAES) system is another technology in which air storage is located under the water or in the ocean. This UWCAES could be integrated with offshore renewable energy resources such as wind and wave [34]. The hydrostatic pressure is used to resist the pressure of the stored air leading to constant pressure within the bag. The pressures of charging and discharging processes depend on the depth. The conceptual design of ocean compressed air energy storage (OCAES) is proposed by [34]. It also consists of five main components which are the compressor, turbine, motor/generator, thermal recovery unit (TRU) and compressed air tank [49]. There are two possible configurations of the UWCAES system shown in Fig. 2.6. The elastic airbag tied up to the seabed is connected to the conversion unit by the air delivery pipeline. In the charging period, the air is compressed and delivered to the airbag. The heat exchanger in TRU is used to extract the generated heat. In the discharging period, the air is released, heated up by the TRU and expanded through the turbine, which is connected to the generator for generating the electrical power. Hydrostor, in Canada, has patented another design of this CAES type which uses the concept of semi-adiabatic UW-CAES that can store electricity for durations of 4-48 hours at scales of 1-50 MW [50].
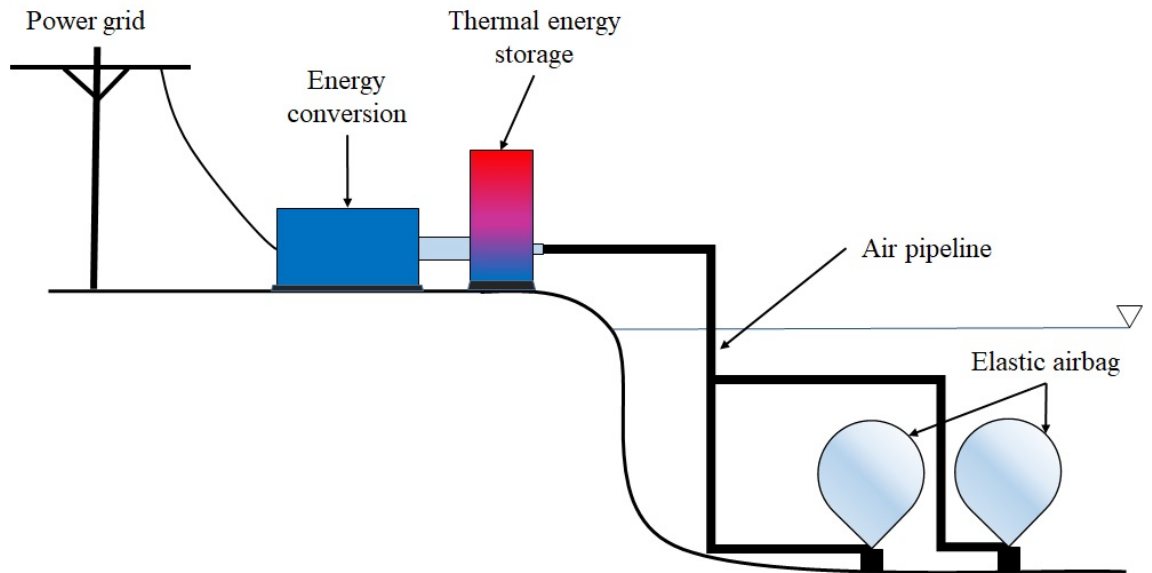
(a) Onshore UWCAES
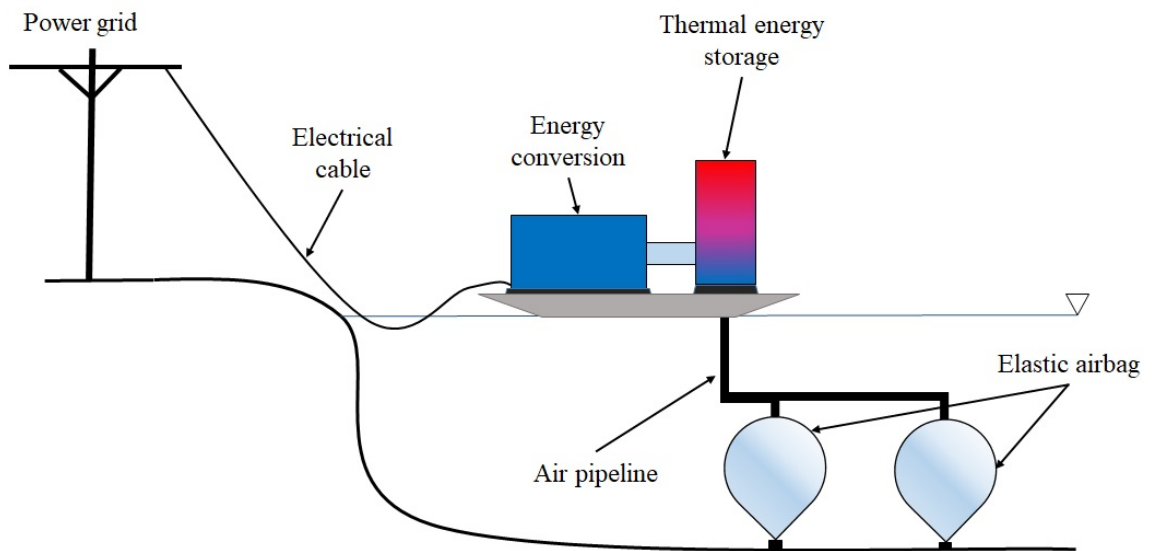
(b) Floating platform UWCAES

Figure 2.6 Possible configurations of UWCAES system [49]

2.2 Hybrid energy storage (HES) system

The topic of improving energy storage system (ESS) capability has attracted interests from many scientists and researchers over the past decade [51]. However, since different ES systems have their own capabilities and limitations such as power density, energy density, life cycle, charge and discharge times, a single ESS cannot meet the requirement of all applications. To resolve this issue, the hybridization of ESS is an alternative concept for combining the benefits of each system and overcoming their disadvantages.

A hybrid energy storage (HES) system seems to be an appropriate method to overcome not only the limitations of a single ESS but also the challenges of renewable energy [52]. A number of published works on HES systems have illustrated the benefits of HES in renewable energy technologies [53]–[56]. The design of the HES depends on the purpose of hybridization, which comprises at least two storage devices, one of high-energy density and the other of high-power density [57]. The high-energy system meets the energy demand for long time periods while the high-power system delivers and absorbs the peak and transient powers [52], [58]. Among the HES systems, using a battery and Fuel cell as a high-energy hybrid storage system was widely investigated [59]–[67]. Considering the CAES system, it has the potential advantages of having a small environmental footprint; it uses air as storage mean without toxic waste, ease of maintenance and recyclability [17]. Its energy density, however, seems to be significantly lower than that of the other systems as illustrated in Fig. 2.7.

A HES system comprising CAES combined with supercapacitor was proposed by Lemofouet and Rufer [43]. The CAES acts as the primary energy supplier that is controlled by a maximum efficiency point tracking (MEPT) system. The supercapacitor is used as a storage and backup system. Martinez et al. [68] has also investigated a similar HES system. In this study, the control system is based on the maximum power point tracking (MPPT) and the supercapacitor is employed to smooth the output power of the system.

A hybrid CAES with a flywheel is another hybrid system that has also been studies. It was proposed by Zhao et al [69]. The system was integrated with the wind energy technology for compensating the fluctuations of the power output. The adiabatic CAES system is operated under constant pressure of turbine inlet and variable cavern pressure while the constant power strategy is implemented by the flywheel.
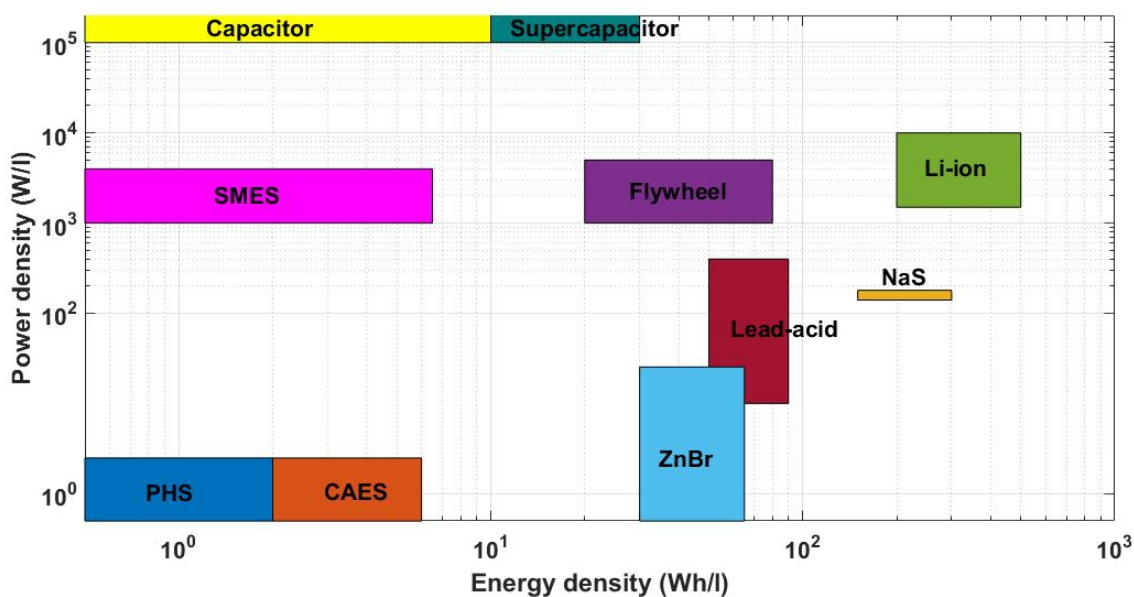
Figure 2.7 Power and energy densities of different ES systems[14], [26], [70]

Most of the works discussed here mainly focus on how to improve the efficiency of CAES system in both small and large scales. Thermodynamic theory including ideal gas equation are the main choice for demonstrating the system's process and calculating the efficiency. Some papers present the electronic control system using control strategies to gain the maximum efficiency from the CAES operation. The MEPT strategy controlling the SS-CAES in a hybrid energy storage system has been investigated successfully by Lemofouet et al. [12], [43] while Kokaew et al. [4], [13], [14] develop a novel MPPT controller for SS-CAES. But the SS-CAES system has a very narrow maximum efficiency peak when it is controlled by MEPT/MPPT controller. A significant drop of efficiency results from a small deviation from the MEPT/MPPT. When SS-CAES is connected to various load levels via the converter, it does not have the potential to resolve this issue leading to lack of power quality. This issue needs to be improved by hybridising with the high-power system such as batteries. In addition, the component's sizes of the system needs to be determined to ensure that the system stores sufficient energy for supply the selected power demand, e.g., a house and shop.

Chapter 3   Small-Scale CAES system and MPPT speed controller

This chapter starts with a description of SS-CAES and then discusses the MPPT speed controller. Next, the controller is designed and simulated to achieve the desired performance. The mathematical model of the air motor is included as well as a PM DC generator connecting with a boost converter. State-space averaged small-signal models are used for designing the parameters of the cascaded PI speed controllers.

3.1 SS-CAES system

During the discharge process, it is important to understand the conversion of pneumatic to electrical energy. This conversion includes the analysis of an air motor model, which is a crucial step in describing the air motor characteristic selected in this research.

Generally, air motor have their individual characteristics and their key physical characteristics such as power, torque, speed and air consumption are employed for obtaining a mathematical model. In this research, the characteristics of the air motor LZB 14 AR034 (110W) [71] are used and scaled appropriately to change the operating pressure and output power. The characteristic data were collected from the experiments of the manufacturer's products [71]. Figure 3.1 presents general technical information for the motor.
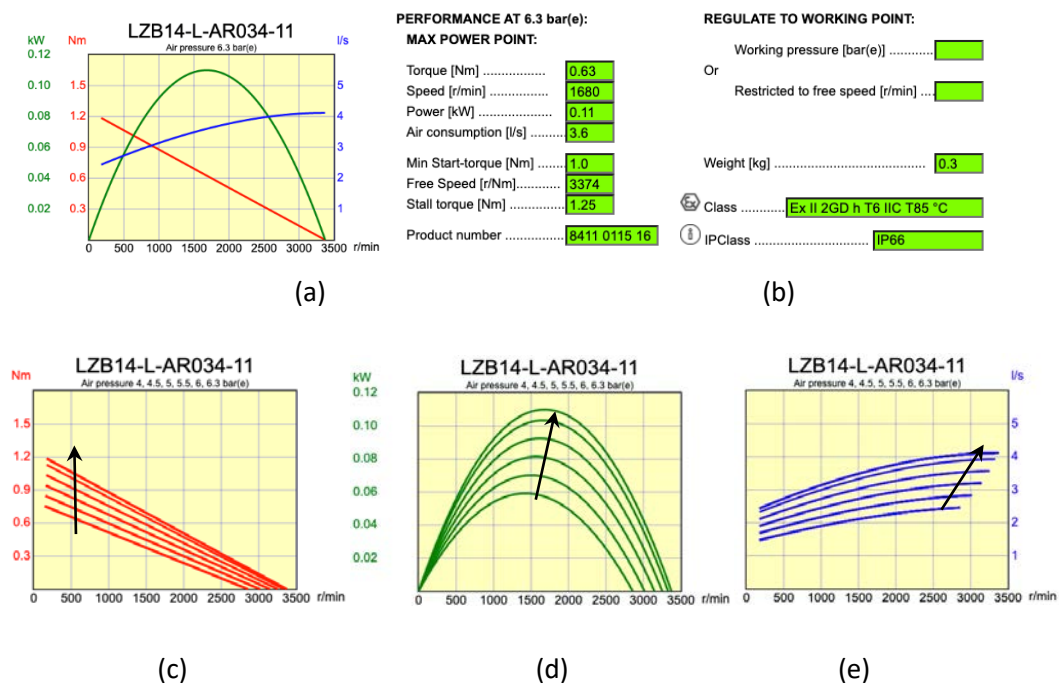
Figure 3.1 The characteristics of the air motor LZB14-AR034 [71]

Fig. 3.1(a) shows three air motor characteristics at the rated pressure: torque, power and air consumption against speed changes while a nameplate of the air motor, which shows the nominal parameters at specific pressure, is presented in Fig. 3.1(b). The air motor torque, power and air consumption with respect to speed changes are respectively illustrated in Fig. 3.1(c)-(e), for different pressure levels of 4, 4.5, 5, 5.5, 6 and 6.3 bar. As can be seen clearly from Fig. 3.1(c), the manufacturer provides a linear stall torque related to speed changes that can be explained by linear characteristic equations, which is dependent on pressure; it is increased according to the raised pressure.

To acquire the mathematical models, all characteristic parameters of the air motor are analysed by using a curve fitting toolbox in Matlab/Simulink. The air motor model is analysed under both constant and variable pressure conditions.

For the constant pressure model, the parameters are analysed in order to obtain the equation of the torque, power and air consumption with respect to the speed change. As stated previously, in Fig. 3.1(a), the air motor provides approximately linear stall torque characteristic that can be modelled by using a linear equation:

$$T_{am} = T_0(p_i) \left(1 - \frac{\omega_r}{\omega_{r0}(p_i)} \right) \tag{3.1}$$

Where T_{am} denotes the mechanical torque (Nm)

$\quad$ T_0 is the stall torque (Nm)

$\quad$ p_i is the inlet pressure (Pa)

$\quad$ ω_r is the rotational speed (rpm)

$\quad$ ω_{r0} is the free speed (rpm)

The mechanical power (P_{am}) can be expressed as the relationship between mechanical torque and angular speed as follows:

$$P_{am} = \omega_r \cdot T_{am} = T_0(p_i) \left(\omega_r - \frac{\omega_r^2}{\omega_{r0}} \right) \tag{3.2}$$

Due to the fact that the air consumption ($\dot{V}_a$) with respect to the speed change is nonlinear, as shown in Fig. 3.1(e), the equation of this characteristic can be analysed based on Gaussian distribution function at the pressure of 6.3 bar. This Gaussian function is used in this study since it is the basic physical model that comprises of a natural exponential function, capable of defining maximum or minimum values with the constant coefficient and a quadratic function [14]. The air motor consumption is given by:

$$\dot{V}_a = \dot{V}_{max}\, e^{\left(-\left(\frac{\omega_r - c_1}{c_2}\right)^2\right)} \tag{3.3}$$

where c_1 and c_2 are real constants that are calculated from different points of the air consumption characteristic curve at 6.3 bar.

For the variable pressure model, it is important to understand the effect of the variable pressure (p_i) on air motor efficiency. The boundary of the parameters such as stall torque (T_0), free speed (ω_{r0}) and air consumption $(\dot{V}_{max})$ can be used to estimate the functions. These effects can be described as follow:

Stall torque: $\quad\quad\quad T_0(p_i) = c_{t1}p_i + c_{t2}$

Free speed: $\quad\quad\quad \omega_{r0}(p_i) = c_{n1}p_i^{c_{n2}} + c_{n3}$

Air consumption: $\quad \dot{V}_{max}(p_i) = c_{a1}p_i + c_{a2}$

Note that $c_{t1}, c_{t2}, c_{n1}, c_{n2}, c_{n3}, c_{a1}$ and c_{a2} are real constants determined by fitting the straight lines at the boundary as illustrated in Fig 3.2. Therefore, the equations of the variable pressure model are obtained by modifying that of the constant pressure model as follows:

$$T_{am}(p_i) = T_0(p_i)\left(1 - \frac{\omega_r}{\omega_{r0}(p_i)}\right) \tag{3.4}$$

$$P_{am}(p_i) = T_0(p_i)\left(\omega_r - \frac{\omega_r^2}{\omega_{r0}(p_i)}\right) \tag{3.5}$$

$$\dot{V}_a(p_i) = \dot{V}_{max}(p_i)e^{\left(-\left(\frac{\omega_r - c_1}{c_2}\right)^2\right)} \tag{3.6}$$
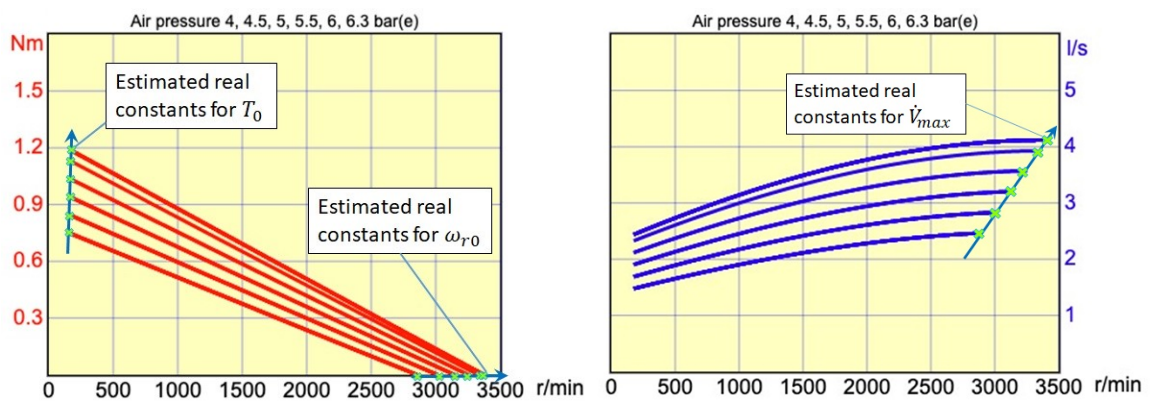
Figure 3.2 Estimated the real constants for $T_0(p_i)$, $\omega_{r0}(p_i)$ and $\dot{V}_{max}(p_i)$

3.2 MPPT speed controller

The MPPT speed controller can be divided into two parts: a speed controller and MPPT algorithm. The MPPT algorithm generates the speed reference at the maximum power point, which is used by the speed controller to control the speed of the generator. This section describes the speed controller, which is analysed using the state-space averaging method. Then, the section moves on to the MPPT algorithm which is used to provide the speed reference.

3.2.1 Speed controller

The speed controller is used to control the air motor speed by controlling the output current of the generator using a power electronic device. It is generally employed in sustainable energy conversion applications such as a wind system [72]–[77]. To achieve a small-signal model of the system for designing the parameters of the speed controller, three methods were considered: absorbed and injected current (AIC), state-space averaging and numerical simulation in Simulink, the actual power electronic circuit including PWM.

The AIC method is used to derive the linearized dynamic model has discussed in [17] and [79]. An example of using this technique is that by Kokaew et al [4], [13], [14] who investigated the MPPT speed regulation in SS-CAES systems. A PMDC generator was coupled with an air motor and a buck converter was used to control the speed. In this study, the AIC method was used to obtain the small signal model. This technique has proved to be a simple method for small-signal model which can be represented by a block diagram or an electrical equivalent circuit. In contrast, and based on the averaged input current, the small-signal of this method might increase the numerical fault and difficulty of the closed-loop design if it is applied to the diode current of the boost converter.

Another technique to obtain the general small-signal model is the numerical analysis of PWM switch. Similar to the AIC method, it applies principle of linearization only to the nonlinear part. The PWM-switch model, presented by Vorperian [79], has the advantages of simplicity and clear understanding of the converter behaviour. A further technique is the state-space averaging method. Unlike the above two mentioned methods, the state equations describing the system are linearized, which can then be applied to a non-linear system [80]. This technique simplify significantly the non-linear system analysis. A small-signal model using the state-space method requires extensive knowledge of matrix algebra for achieving the relevant gains but it is suitable for computational simulations, i.e., using Matlab/Simulink, for designing the controller [14], [76], [81]. In this thesis, the average state-space method is used to analyse a small-signal model of the SS-CAES system for controlling a boost converter. Fig.3.3 shows the configuration of the SS-CAES using MPPT speed controller. The air motor is used to drive the DC generator for pneumatic-electric

energy conversion while the boost converter controls the output current being delivered to the load. The system is used with MPPT strategy which is illustrated in the next subsection.
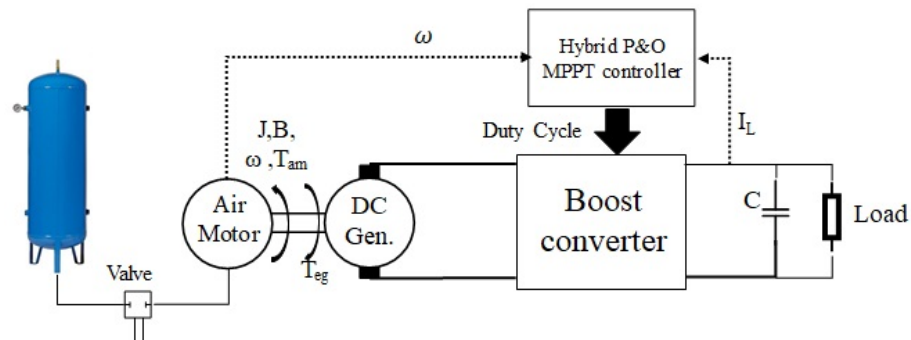
Figure 3.3 Configuration of SS-CAES using MPPT controller

3.2.2 MPPT algorithm - Review

The MPPT strategy was implemented to set the reference speed of the speed controller of the air motor. MPPT methods can be categorized into 19 different algorithms which are reviewed in [82]. For example, perturb and observe (P&O), incremental conductance (INC), constant voltage (CV) and fuzzy logic control. Most of these methods can give the exact MPP while some of them provide only an approximation [83]. A number of researchers have studied MPPT algorithms in order to understand their operational strategies and their performances in order to identify the most suitable approach for their maximum power tracking. Among these studies, the P&O method seems to be the most widely used method due to its advantages such as ease of implementation, simplicity and low computational power need.[82], [84]–[87].

In 2006, Lemofouet *et al.* [43] used a maximum efficiency point tracking (MEPT) algorithm with a heat exchanger to improve the performance of a hydro-pneumatic system. At a constant pressure of 350 bar, the system operated with a hydraulic motor providing an efficiency of over 94%. The MEPT algorithm based on the perturb and observe (P&O) method controlled the output of the pneumatic to mechanical conversion. In order to track the maximum efficiency point (MEP), the system employed a number of sensors such as pressure, flow rate and speed sensors. However, the MEP is difficult to track accurately in real time since it depends on the accuracy of the system model and estimation of losses [12]. On the other hand, MPPT is easier for real-time tracking than MEPT because the output power can be measured directly.

In an interesting research on MPPT by Martinez et al [37], P&O method is used to track the maximum power of pneumatic to electric conversion. A pressure transducer is utilized to approximate the initial speed of the air motor. The P&O method in this paper has a fixed speed step for incrementing and decrementing the air motor speed and then considers whether the power has

decreased or increased. The outcome of this paper that the MPPT algorithm provides the speed reference to control the actual rotation speed of the air motor to operate at the maximum power point, which improve the thermodynamic conversion. However, it requires another energy storage system to improve it for producing a smoother output power, which make it suitable for supporting the renewable energy applications.

Amongst research on MPPT using P&O method, Kokaew *et al.* [4], [14] introduced a novel P&O method by calculating the derivative of the power with respect to speed $(dP/d\omega)$ as well as the derivative of power with respect to the duty cycle of the dc-dc converter (dP/dD). Moreover, the step speed change is divided into two-step sizes. A small step size is used for the fine tuning region where $dP/d\omega$ is used to decide the direction of the next speed step in the MPP proximity, and a coarse step change that is used with dP/dD when the operating point is far from the MPP. The validation of this method was done by experiments [4], [14]. The results showed that using the rate of change of power with respect to the duty cycle provides a better performance than using the rate of change of power with respect to speed. However, using both of these under certain circumstances will still result in the algorithm selecting the wrong direction of speed change, increasing instead of decreasing speed or vice versa.

Most applications of the MPPT algorithm using the P&O method have been with PV systems which often suffer from the operating point oscillating around the MPP [73], [88]. The accuracy and the convergence speed to MPP depend on the step-size selection. The small step size provides an accuracy higher than the large step size. In contrast, the large step size can increase the speed of convergence in response to rapid change of the operating condition [82], [86]–[90]. Moreover, these methods cannot make correct decisions on the required direction of the reference current or voltage [91], [92]. As a result, there will be undesirable energy losses during wrong direction speed changes.

In [14], MPPT- fuzzy logic control together with a variable step size is used to reduce these problems. Two key approaches that are applied in the study are a fuzzy logic control and a vector-fuzzy logic control. After simulation and validation by experiment, the system can provide the desired speed smoothly around the MPP but it still makes wrong decisions under small pressure fluctuating conditions. Furthermore, the power tracking of the MPPT- fuzzy logic control is less accurate than that of the MPPT-P&O algorithm.

The review clearly shows that the P&O method is used in both MEPT and MPPT. This method is popular and can be easily implemented but lack of accuracy and tracking failure under rapidly changing conditions are its common disadvantages [93]. These drawbacks have been investigated by Kokaew [14], who has consequently introduced a hybrid P&O algorithm as mentioned earlier.

The SS-CAES using the proposed MPPT strategy has a good performance to operate at the MPP, which provides the efficiency close to that using the MEPT strategy. However, it does not have the potential to respond to the fluctuating load demand since its operating area is around the maximum power peak. When the load demand changes, the system's efficiency will drop considerably because of the deviation from the MPPT. This issue can be improved by adding another energy storage device such as a battery as a hybrid energy storage system, which is an interesting point of this thesis. Therefore, the hybrid P&O MPPT algorithm proposed by Kokaew [14] is discussed in this thesis as a design method for the SS-CAES system.

P&O MPPT speed controller

The MPPT controller is designed by considering the power-speed and duty cycle-speed graphs. The power-speed curve under the specific pressure is plotted by using Eq. (3.2). The duty cycle-speed curve can be plotted by considering the relationship between the air motor power, converter's output power and both mechanical and electrical losses, which is expressed as:

$$P_{am} = \frac{V_o{}^2}{R_L} + P_{fc} + i_{ag}^2 r_{ag} \tag{3.7}$$

Since the PM DC generator coupled with air motor generates the input voltage(e_{ag}), the behaviour of PM DC generator should be considered in order to understand all models of the system. From Fig. 3.4, the dynamic behaviour of PM DC generator, described by Newton's 2nd law, is expressed as:

$$T_{am} = T_{eg} + B_t \omega_r + J_t \frac{d\omega_r}{dt} \tag{3.8}$$
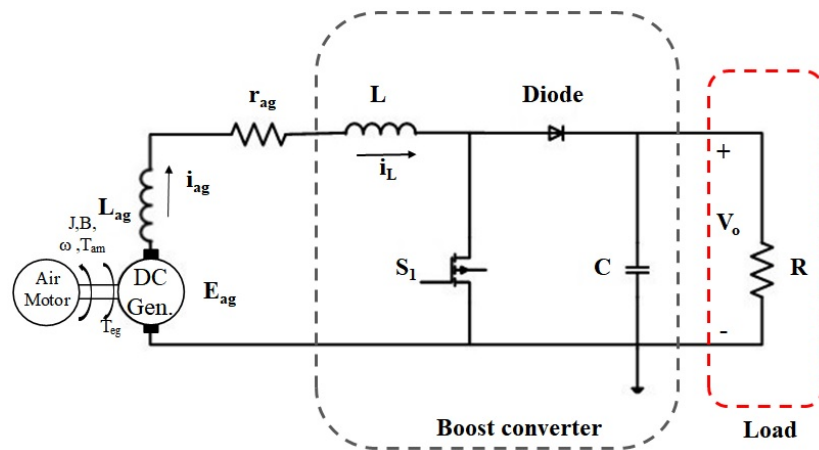
Figure 3.4 Circuit diagram of the discharge process with boost converter

where T_{eg} is load torque (N.m)

B_t is the total viscous friction coefficient (N.m.s/rad)

ω_r is angular velocity (rad/s)

J_t is the combined moment of inertia of the air motor and generator (kg.m²)

The back electromagnetic force (emf) of the generator is expressed by

$$e_{ag} = K_m \omega_r \tag{3.9}$$

where K_m is the back emf constant (V.s/rad). This back emf is obtained from the load torque of the air motor:

$$T_{eg} = K_e i_{ag} \tag{3.10}$$

where K_e is the generator's torque constant (N.m/A). For the lossless converter, the efficiency of the boost converter can be expressed as [94]:

$$\eta_c = M_v(1 - D) \tag{3.11}$$

where $M_v = \dfrac{V_o}{e_{ag}}$ and D is the duty cycle. To maintain the continuous mode during the duty cycle, the inductance is calculated by the following expression [95]:

$$L = \frac{e_{ag}D}{f_s \Delta i_L} \tag{3.12}$$

The capacitance is required for reducing a load voltage, which is expressed by

$$C_o = \frac{DI_o}{f_s \Delta v_o} \tag{3.13}$$

Therefore, substituting Eq. (3.9) and (3.11) into Eq. (3.7), the power of the air motor can be revised as follows:

$$P_{am} = \frac{\left(\eta_c e_{ag}/_{1-D}\right)^2}{R_L} + P_{fc} + i_{ag}^2 r_{ag} = \frac{\left(\omega_r K_m \eta_c/_{1-D}\right)^2}{R_L} + P_{fc} + i_{ag}^2 r_{ag} \tag{3.14}$$
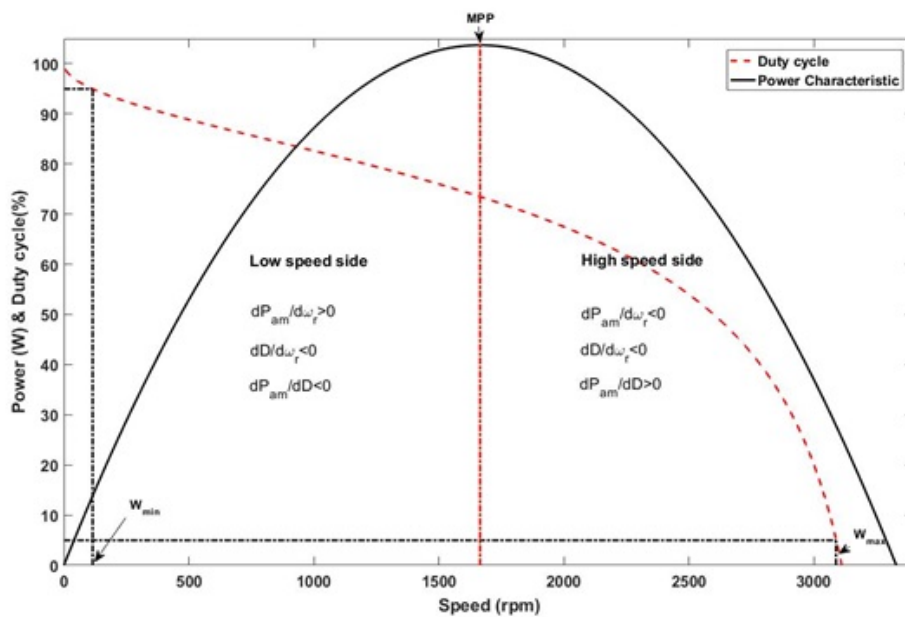
Figure 3.5 Air motor power and duty cycle of the boost converter versus speed

The duty cycle-speed and the power-speed curves are then plotted in Fig. 3.5. The assumptions in the figure are that the output power is around 110 W, the boost converter efficiency is 90% and the total power losses are zero. It can be seen clearly that the duty cycle of the boost converter has the practical range limitation from 95% to 5% [94]. The controller cannot set the reference speed to maintain the speed of converter at the low speed side if the speed is less than a minimum value of W_{min}, i.e., when the duty cycle is above 95%. Similarly, the reference speed at the high-speed side cannot be set when the speed is faster than the maximum value of W_{max}, i.e., when the duty cycle is less than 5%. This means that the controller becomes unstable when the duty cycle operates above 95% and below 5%.

The speed operating point is identified by using the slopes of the air motor power-speed and duty cycle-speed curves until the MPP is tracked. The operating point is calculated by the change of power with respect to the change of duty cycle $\left(\frac{dP_{am}}{dD}\right)$ using the *chain rule*.

$$\frac{dP_{am}}{dD} = \frac{dP_{am}}{d\omega_r} \cdot \frac{d\omega_r}{dD} \qquad (3.15)$$

The operating point is on the low speed side if the slope of $dP_{am}/d\omega_r$ is positive but $dD/d\omega_r$ is negative. The slope of dP_{am}/dD, then, is negative. Therefore, the speed increases within constant step-size when the operating point is at low speed side, based on the basic principle of the P&O algorithm. In contrast, the constant step-size speed decreases if the operating point is located at the high-speed side, the slope of dP_{am}/dD is positive resulting from the negative slopes of both $dP_{am}/d\omega_r$ and $dD/d\omega_r$.
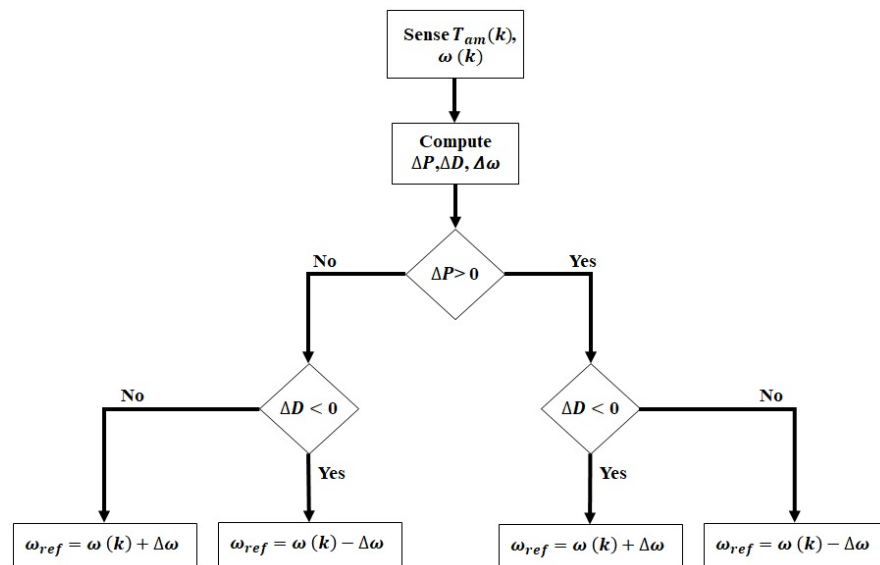
Figure 3.6 MPPT flowchart

The flow chart of the MPPT controller based on [4] is shown in Fig. 3.6. Torque and speed values are measured and used to compute the change of power, duty cycle and speed. If the power

difference is positive and the duty cycle difference is negative, the reference speed then will be increased by an amount of $\Delta\omega$. If both these differences are positive, the reference speed then will be decreased by the same amount. On the other hand, if the differences in power and duty cycle values are negative, then the reference speed will be decreased, and if the differences in power is negative and the duty cycle positive, then the reference speed will be increased.

3.3 SS-CAES and controller modelling

3.3.1 SS-CAES model

For the discharge process, the SS-CAES consists of three significant components, namely, the air tank, the air motor and the PMDC generator connected to the boost converter. The model of the SS-CAES system was built by using Matlab/Simulink as shown in Fig. 3.7. The mathematical equations describing the air motor characteristics are created based on Eq. (3.4) – (3.6). The boost converter consists of MOSFET switch, capacitor, resistive load, inductor and diode that are connected to the air motor model as well as the PMDC generator in both constant and variable pressure conditions. For this model, the large air tank is assumed to supply enough air mass throughout the process under isothermal condition with no losses. The mathematical models of the air motor characteristics and the details of the system parameters are listed and presented in Appendix A and C.1, respectively.
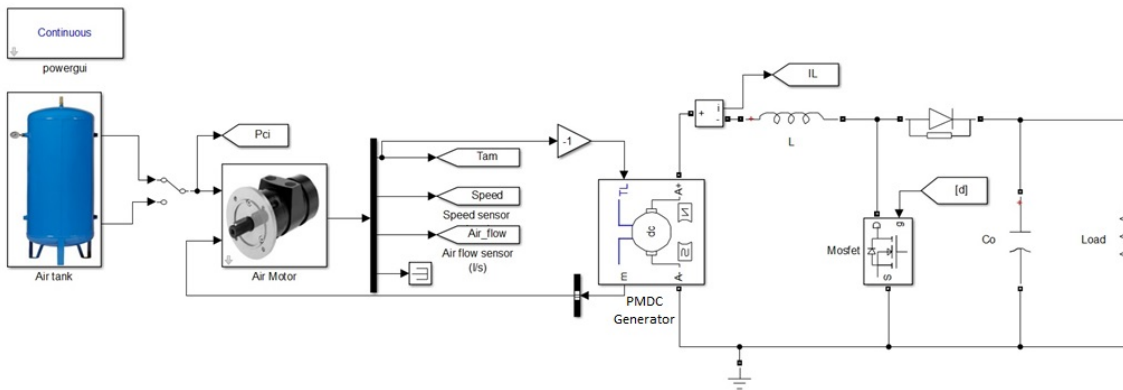
Figure 3.7 SS-CAES system with boost converter model

3.3.2 MPPT speed controller model

Speed controller analysis

To design the speed controller, the averaging state-space method is used in order to obtain an expression for the transfer function of the DC generator with the converter. This transfer function

is used to design the control system by designing speed regulation and analysing its stability. The equivalent circuit of the DC generator with the boost converter model is presented in Fig. 3.8.
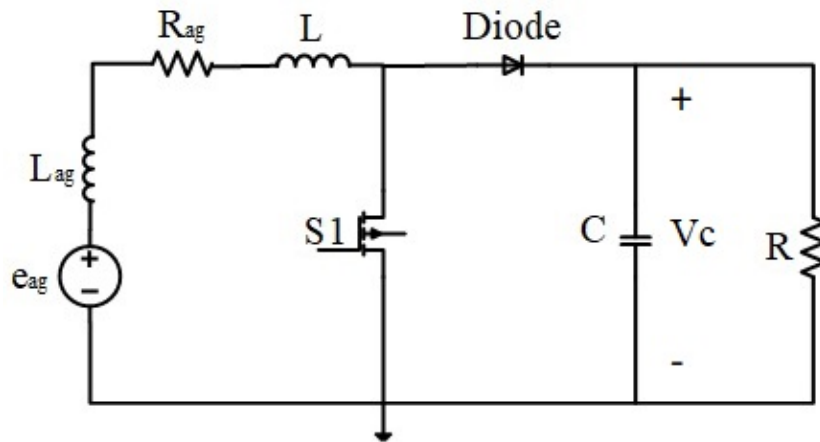
Figure 3.8 DC generator with boost converter model

Generally, the generator with a boost converter uses the MOSFET as the switching device, which operates within two operating modes of continuous and discontinuous. This work considers only the continuous operating mode of the system. Considering the switching operation when the MOSFET is switched on, the state equations can be obtained by using Kirchhoff's voltage law. The equivalent circuit is shown in Fig 3.9.
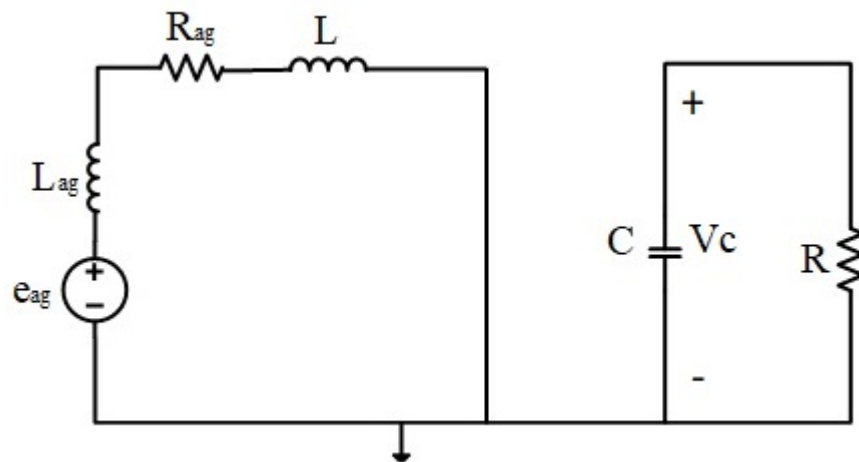
Figure 3.9 DC generator with boost converter model when switch is on

The state vectors for this boost converter are defined by $[i_L(t) \quad v_C(t)]$. The state equations are given by:

$$e_{ag} = L_{ag}\frac{di_L}{dt} + R_{ag}i_L + L\frac{di_L}{dt} \tag{3.10}$$

$$V_c + RC\frac{dv_c}{dt} = 0 \tag{3.11}$$

With

$$V_{out} = -RC\frac{dv_c}{dt} \tag{3.12}$$

Rearranging for state-space equation in matrix form of the ON state switching configuration:

$$\frac{d}{dt}\begin{bmatrix} i_L \\ v_c \end{bmatrix} = \begin{bmatrix} -\frac{R_{ag}}{L_{ag}+L} & 0 \\ 0 & -\frac{1}{RC} \end{bmatrix}\begin{bmatrix} i_L(t) \\ v_c(t) \end{bmatrix} + \begin{bmatrix} \frac{1}{L_{ag}+L} \\ 0 \end{bmatrix}e_{ag} \tag{3.13}$$

$$V_{out} = -R\left(-\frac{V_c}{R}\right) = [0 \quad 1]\begin{bmatrix} i_L(t) \\ v_c(t) \end{bmatrix} \tag{3.14}$$

Then

$$A_1 = \begin{bmatrix} -\frac{R_{ag}}{L_{ag}+L} & 0 \\ 0 & -\frac{1}{RC} \end{bmatrix}; \; B_1 = \begin{bmatrix} \frac{1}{L_{ag}+L} \\ 0 \end{bmatrix}; \; C_1 = [0 \quad 1]$$

Considering the switching operation when the MOSFET is switched off, the equivalent circuit is shown below in Fig 3.10.
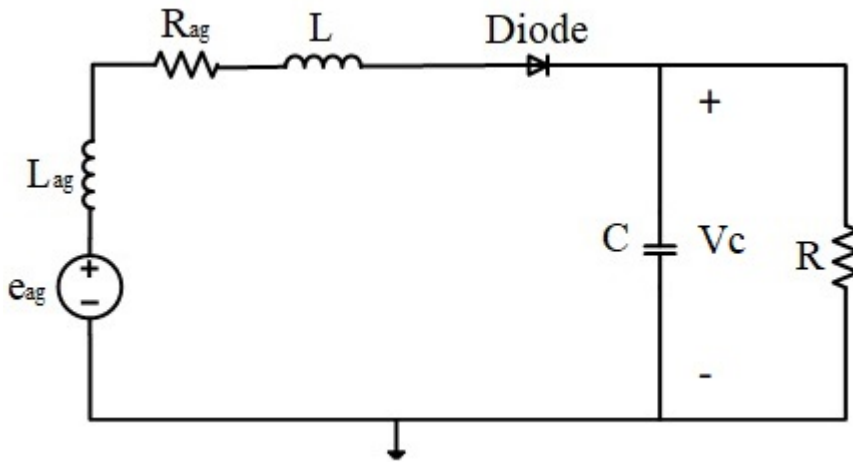
Figure 3.10 DC generator with boost converter model when switch is off

Applying the Kirchhoff's voltage law to the loop of the switching-off configuration gives:

$$e_{ag} = L_{ag}\frac{di_L}{dt} + R_{ag}i_L + L\frac{di_L}{dt} + V_c \tag{3.15}$$

$$V_c - R\left(i_L - C\frac{dv_c}{dt}\right) = 0 \tag{3.16}$$

With

$$V_{out} = R\left(i_L - C\frac{dv_c}{dt}\right) \tag{3.17}$$

The state-space equations in matrix form describing the OFF state switching mode are:

$$\frac{d}{dt}\begin{bmatrix} i_L \\ v_c \end{bmatrix} = \begin{bmatrix} -\frac{R_{ag}}{L_{ag}+L} & -\frac{1}{L_{ag}+L} \\ \frac{1}{C} & -\frac{1}{RC} \end{bmatrix}\begin{bmatrix} i_L(t) \\ v_c(t) \end{bmatrix} + \begin{bmatrix} \frac{1}{L_{ag}+L} \\ 0 \end{bmatrix} e_{ag} \tag{3.18}$$

$$V_{out} = -R\left(i_L - \left(i_L - \frac{v_c}{R}\right)\right) = \begin{bmatrix} 0 & 1 \end{bmatrix}\begin{bmatrix} i_L(t) \\ v_c(t) \end{bmatrix} \tag{3.19}$$

That is

$$A_2 = \begin{bmatrix} -\frac{R_{ag}}{L_{ag}+L} & -\frac{1}{L_{ag}+L} \\ \frac{1}{C} & -\frac{1}{RC} \end{bmatrix}; \ B_2 = \begin{bmatrix} \frac{1}{L_{ag}+L} \\ 0 \end{bmatrix}; \ C_2 = \begin{bmatrix} 0 & 1 \end{bmatrix}$$

The average state-space equations can be calculated by using the expression for the duty cycle (D): $A_{av} = A_1D + A_2(1-D), B_{av} = B_1D + B_2(1-D), C_{av} = C_1D + C_2(1-D)$. Therefore, the average state-space matrices can be given as:

$$A_{av} = \begin{bmatrix} -\frac{R_{ag}D}{L_{ag}+L} - \frac{R_{ag}(1-D)}{L_{ag}+L} & -\frac{1-D}{L_{ag}+L} \\ \frac{1-D}{C} & -\frac{D}{RC} - \frac{(1-D)}{RC} \end{bmatrix} = \begin{bmatrix} -\frac{R_{ag}}{L_{ag}+L} & -\frac{1-D}{L_{ag}+L} \\ \frac{1-D}{C} & -\frac{1}{RC} \end{bmatrix}$$

$$B_{av} = \begin{bmatrix} \frac{1}{L_{ag}+L} \\ 0 \end{bmatrix}D + \begin{bmatrix} \frac{1}{L_{ag}+L} \\ 0 \end{bmatrix}(1-D) = \begin{bmatrix} \frac{1}{L_{ag}+L} \\ 0 \end{bmatrix} \tag{3.20}$$

$$C_{av} = \begin{bmatrix} 0 & 1 \end{bmatrix}$$

The steady-state DC solution (X) for the system can be obtained by

$$X = -A_{av}^{-1}B_{av}V_{in}$$

$$X = -\begin{bmatrix} -\frac{R_{ag}}{L_{ag}+L} & -\frac{1-D}{L_{ag}+L} \\ \frac{1-D}{C} & -\frac{1}{RC} \end{bmatrix}^{-1}\begin{bmatrix} \frac{1}{L_{ag}+L} \\ 0 \end{bmatrix}E_{ag}$$

$$= \frac{1}{R_{ag}+R(1-D)^2}\begin{bmatrix} 1 \\ R(1-D) \end{bmatrix}E_{ag} \tag{3.21}$$

From this DC solution, the output voltage is obtained by using the formula $V_{out} = C_{av}X$

$$V_{out} = \begin{bmatrix} 0 & 1 \end{bmatrix}\frac{1}{R_{ag}+R(1-D)^2}\begin{bmatrix} 1 \\ R(1-D) \end{bmatrix}E_{ag}$$

$$V_{out} = \frac{R(1-D)E_{ag}}{R_{ag}+R(1-D)^2} \tag{3.22}$$

As a result, the DC voltage conversion gain (M) is calculated by:

$$M_v = \frac{V_{out}}{V_{in}} = -C_{av}A_{av}^{-1}B_{av}$$

$$= \frac{R(1-D)}{R_{ag} + R(1-D)^2} \tag{3.23}$$

According to the current mode control for the small-signal analysis, there are four open-loop transfer functions, which are needed to derive via Laplace transformation: duty cycle-to-output voltage (G_{vd}), input voltage-to-inductor current (G_{ig}), duty cycle-to-inductor current (G_{id}) and output voltage-to-inductor current (G_{iv}).

Duty cycle-to-output voltage small-signal open-loop transfer function(G_{vd})

The transfer function for $G_{vd}(s)$ can be defined as:

$$G_{vd}(s) \triangleq \frac{\hat{V}_{out}(s)}{\hat{D}(s)} = C_{av}(sU - A_{av})^{-1}[(A_1 - A_2)X + (B_1 - B_2)V_{in}] + (C_1 - C_2)X$$

Where s donates a complex variable and U is an identity matrix. Since, B_1 and B_2 for this converter are equal, $G_{vd}(s)$ can be rewritten as:

$$G_{vd}(s) \triangleq \frac{\hat{V}_{out}(s)}{\hat{D}(s)} = C_{av}(sU - A_{av})^{-1}(A_1 - A_2)X$$

$$= \frac{s - \frac{R(1-D)^2 - R_{ag}}{L_t}}{s^2 + \left(\frac{L_t + R_{ag}RC}{RCL_t}\right)s + \frac{R_{ag}R(1-D)^2}{RCL_t}} \cdot \frac{E_{ag}}{R_{ag} + R(1-D)^2} \tag{3.24}$$

Where $L_t = L_{ag} + L$

Input voltage-to-inductor current small-signal open-loop transfer function(G_{ig})

As the steady-state DC solution components consist of average inductor current $\left(I_{L_{av}}\right)$ and capacitor voltage $\left(V_{C_{av}}\right)$, the input voltage-to-inductor current transfer function $\left(G_{ig}\right)$ can be given by taking the first row of the matrix.

$$G_{ig}(s) \triangleq \frac{\hat{I}_L(s)}{\hat{V}_{in}(s)} = (sU - A_{av})^{-1}B_{av}$$

$$= \frac{\left(s + \frac{R_{ag}}{L_t}\right)\frac{1}{L_t}}{s^2 + \left(\frac{L_t + R_{ag}RC}{RCL_t}\right)s + \frac{R_{ag}R(1-D)^2}{RCL_t}} \tag{3.25}$$

Duty cycle-to-inductor current small-signal open-loop transfer function(G_{id})

The transfer function $G_{id}(s)$ can be defined as:

$$G_{id}(s) \triangleq \frac{\hat{I}_L(s)}{\hat{D}(s)} = (sU - A_{av})^{-1}[(A_1 - A_2)X + (B_1 - B_2)V_{in}]$$

As $B_1 = B_2$ for this converter, the duty cycle-to-inductor current open-loop transfer function $G_{id}(s)$ can be obtained by taking only the first row of the matrix $(sU - A_{av})^{-1}(A_1 - A_2)X$:

$$G_{id}(s) = \frac{s + \frac{2}{RC}}{s^2 + \left(\frac{L_t + R_{ag}RC}{RCL_t}\right)s + \frac{R_{ag}R(1-D)^2}{RCL_t}} \cdot \frac{E_{ag}}{R_{ag} + R(1-D)^2} \tag{3.26}$$

Output voltage-to-inductor current small-signal open-loop transfer function(G_{vi})

This transfer function can be developed properly for the closed loop system design after achieving the various transfer functions. $G_{vi}(s)$ can be expressed as:

$$G_{vi}(s) \triangleq \frac{\hat{I}_L(s)}{\hat{V}_{out}(s)} = \frac{G_{id}(s)}{G_{vd}(s)} = \frac{\hat{I}_L(s)}{\hat{D}(s)} \cdot \frac{\hat{D}(s)}{\hat{V}_{out}(s)}$$

$$= \frac{s + \frac{2}{RC}}{s - \frac{R(1-D)^2 - R_{ag}}{L_t}} \tag{3.27}$$
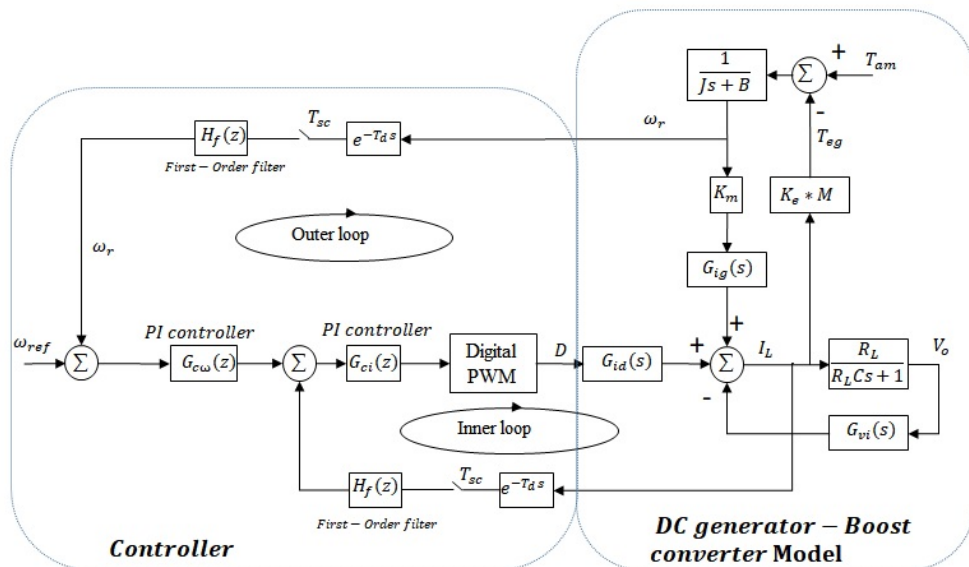
Figure 3.11 Block diagram of speed control model [17]

A speed controller is designed based on a small-signal state-space model presented in Fig. 3.11. The system block can be divided into two main parts: the controller on the left and the small signal model of the DC generator with a buck converter on the right. This speed regulator controls the air motor speed to reach the MEP and MPP. Two cascaded PI loops are needed to be considered for designing the speed controller that are an outer speed loop and an inner inductor current loop. Throughout this thesis, the controllers are assumed to have fast computational speed and data acquisition in both analogue-digital and digital-analogue converters. Generally, in designing the controller we need to investigate the control stability which is carried out for the open-loop transfer function. According to [96], the stability of the open-loop system guarantees stability of the close-

loop system (i.e., for the frequency response with respect to the zero gain line and phase across 180°). The gain and phase margins selected on Bode diagram are used as the classical indicators for providing the system's stability. For the stability of the controller design, a gain margin must be specified greater than 3 dB and a phase margin must be selected between 30° and 60°. The controller design must ensures that the system's operating point is far from the critical point, which results in the system's stability [96].

For the inner current loop, the PI controller is used to ensure that the inductor current has zero error. The controller provides the duty cycle to maintain a constant inductor current i_L. The design can be done by using the open-loop transfer function of the inductor current based on the Mason's rules [97]. This transfer function is expressed as:

$$G_{ip}(s) = \frac{G_{id}(s)}{1+\Delta_1} \tag{3.28}$$

where $\Delta_1 = G_{vi}(s)G_{st}(s) + MK_mK_eG_{ig}(s)G_d(s).$

$$G_{st}(s) = \frac{R_L}{R_LC_os+1} \text{ and } G_d(s) = \frac{1}{J_ts+B_t}$$

This open-loop transfer function is cascaded with a digital low pass filter in order to modify the control strategy in a flexible manner. The low pass filter is expressed by

$$H_f(z) = \frac{1-e^{\omega_{cf}T_{sc}}}{z-e^{\omega_{cf}T_{sc}}} \tag{3.29}$$

where ω_{cf} is the cut-off frequency and T_{sc} is the sampling period.

For the outer speed loop, PI controller is used to maintain the error of the generator's speed as close to zero as possible by providing the inductor current reference I^* to the inner-current loop. To stabilize the speed control of a DC generator, the open loop transfer function of the outer speed loop is presented by

$$G_{\omega p}(s) = \frac{\omega_r(s)}{I^*(s)} = -\frac{MK_eG_{ci}(s)G_{id}(s)G_d(s)}{1+\Delta_2} \tag{3.30}$$

where $\Delta_2 = G_{vi}(s)G_{st}(s) + MK_mK_eG_{ig}(s)G_d(s) + G_{ci}(s)G_{id}(s)H_f(s)$

The speed controller needs to be tuned for stabilizing both PI controllers. The transfer functions are plotted using the Bode diagram in order to specify the gain and phase margins of the control system. The results of the controller tuning will be illustrated in subsection 3.4.2.

Comparison between MEP and MPP

The comparison between MEP and MPP have been reported by Kokaew [13]. The performance of the air motor needs to be maximised by using the MPPT controller. However, it is important to consider the difference between the maximum efficiency and maximum power points.

For the MEP, the efficiency of the air motor conversion (η_{am}) based on the first and second laws of thermodynamics (see Appendix) can be expressed as:

$$\eta_{am} = \frac{T_0(p_i)\frac{\pi}{30}\left(\omega_r - \frac{\omega_r^2}{\omega_{r0}(p_i)}\right)}{\frac{\gamma}{\gamma-1}p_a\dot{V}_a\left[\left(\frac{p_i}{p_a}\right)^{\frac{\gamma-1}{\gamma}}-1\right]} \tag{3.37}$$

where p_a, p_i are the ambient and inlet pressures and γ is the ratio of the specific heat that is equal to c_p/c_v. The value of γ in this thesis is 1.4 at temperature 293 K. To determine the maximum efficiency, the derivative of the efficiency in (3.37) with respect to the speed change can be expressed as

$$\frac{d\eta_{am}}{d\omega_r} = K_1\frac{\pi}{30}\left(\omega_r - \frac{\omega_r^2}{\omega_{r0}(p_i)}\right) \tag{3.38}$$

where $K_1 = \dfrac{T_0(p_i)}{\frac{\gamma}{\gamma-1}p_a\dot{V}_a\left[\left(\frac{p_i}{p_a}\right)^{\frac{\gamma-1}{\gamma}}-1\right]}$.

For the MPPT, the derivative of mechanical power with respect to speed, which provides the error, is expressed by:

$$\frac{dP_{am}}{d\omega_r} = T_{am}(p_i)\left(1 - 2\frac{\omega_r}{\omega_{r0}(p_i)}\right) \tag{3.39}$$

To reach the maximum power point, the error should be zero. Therefore, the speed at the maximum power point is given by:

$$\omega_r = \frac{\omega_{r0}(p_i)}{2} \tag{3.40}$$

To find differences between the two strategies, comparisons should be made. The design of the MEPT/MPPT controller is shown below in Fig. 3.12. If MEPT is selected, the reference speed is set by using Eq. (3.38). On the other hand, the speed reference is set to be half of the free speed if MPPT is selected.

Figure 3.12 MEPT/MPPT controller

MPPT controller

Successful comparison of the MEPT and MPPT strategies has led to the implementation of the P&O MPPT controller, described in Section 3.2, using SimPowerSystems of Matlab/Simulink.

Figure 3.13 The cascaded PI speed controller scheme

Fig. 3.13 depicts the control scheme of CAES with a boost converter. Here, the converter is controlled by two cascaded PI controllers, i.e., an outer speed control loop that sets the reference speed for an inner current control loop. The speed of the air motor (ω) is sensed and compared with the MPPT speed reference (ω_{ref}) in order to calculate the error. This speed error is then used by a PI controller to set the current reference (I_{ref}). The CAES current (I_L) will track this reference value and the duty cycle for the converter is produced accordingly.

3.4 Simulation results

3.4.1 Air motor characteristics

In the discharge process, the air motor characteristics were identified. The mathematical models were implemented by using MATLAB/Simulink. The characteristics of the air motor LZB 14 AR034 (110W), shown in Appendix A, [71] are used in this work under the assumption of constant inlet and varying pressure; they are scaled appropriately to change operating pressure and output power. The comparisons between the mathematical models and the information from the manufacturer are illustrated in Fig. 3.14–3.16.

Figure 3.14 Air consumption characteristic of air motor
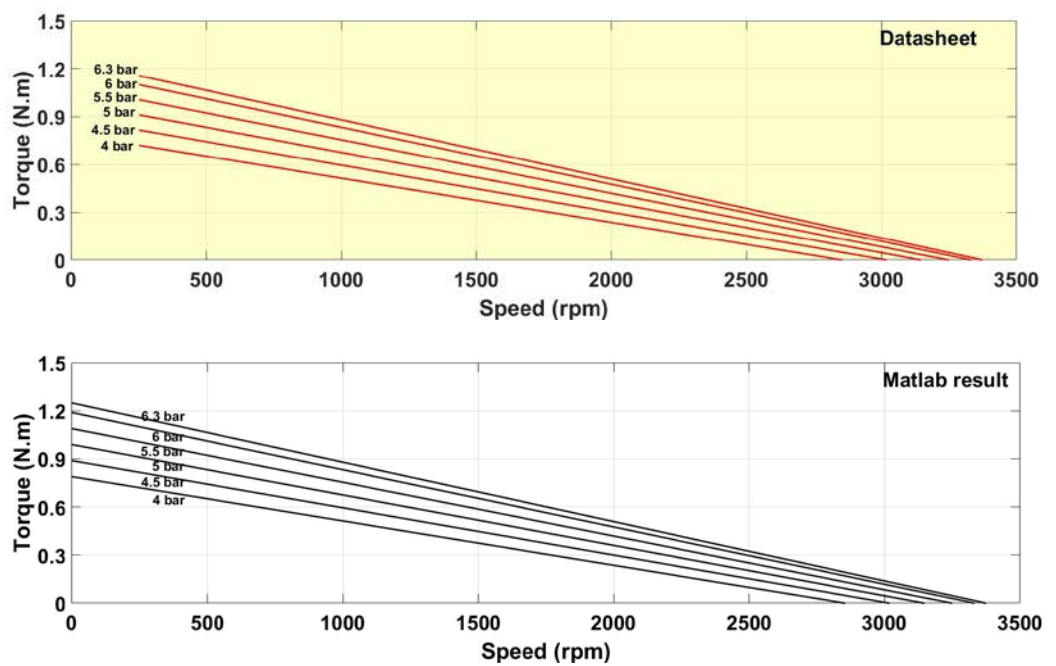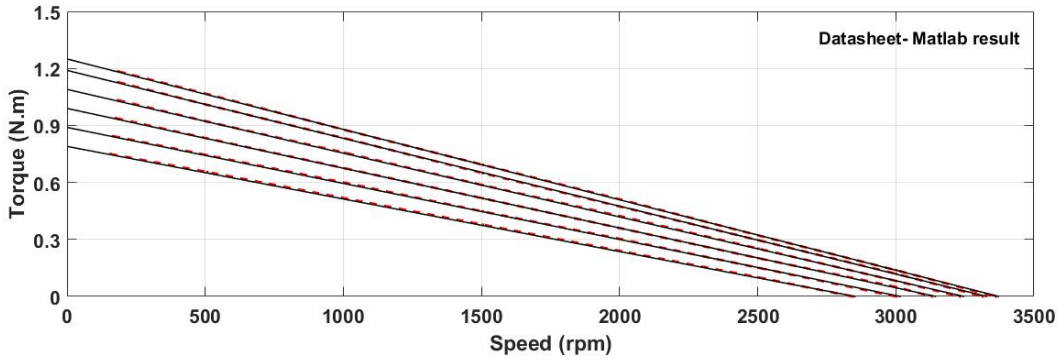
Figure 3.15 Air motor torque characteristic
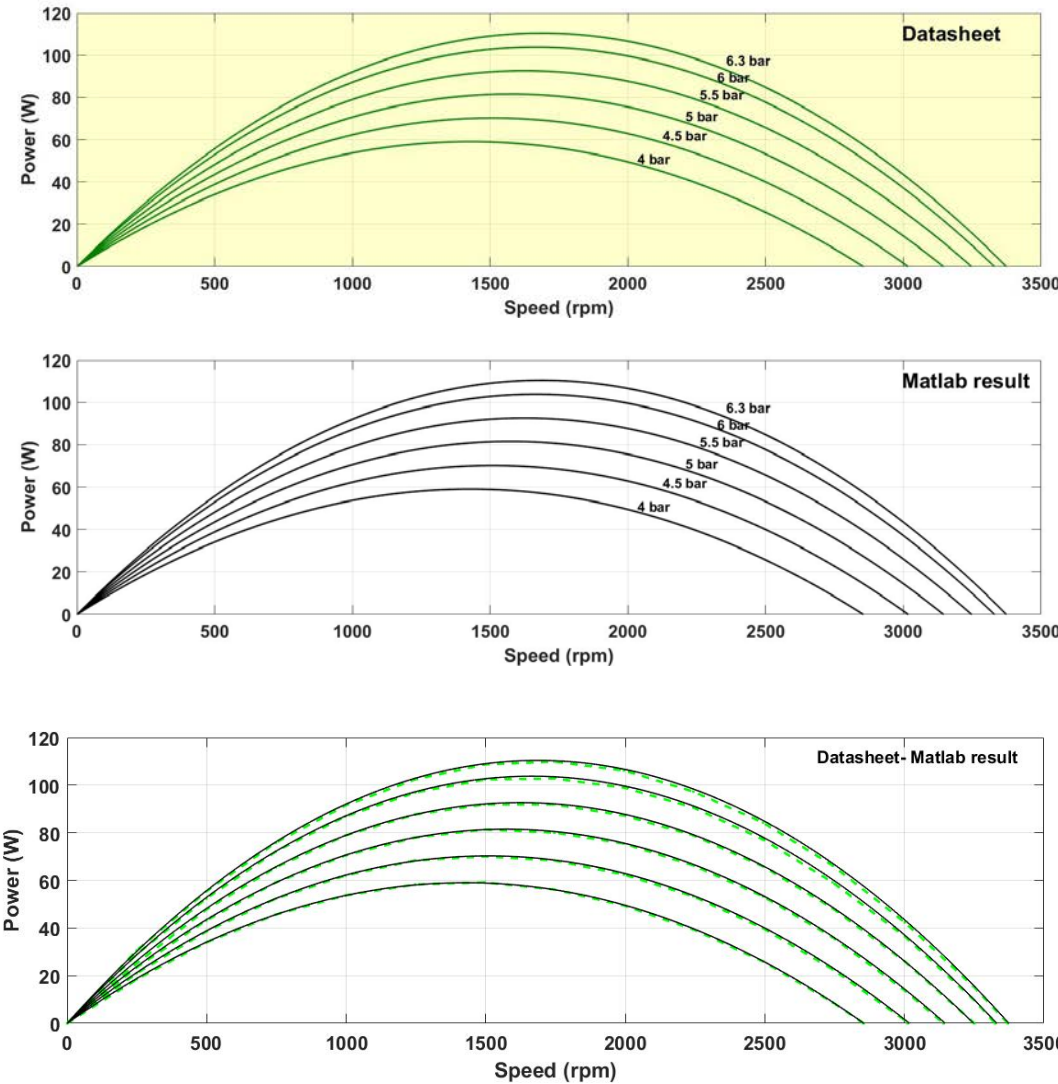
Figure 3.16 Power characteristic of the air motor

As illustrated in Fig. 3.14 – 3.16, the mathematical models provide similar results to the data from the manufacturer. It can be concluded that the derived equations are good fits to the real data, which can be used to simulate in this study. Due to the fact that this study follows on from the previous work done by Kokaew *et al.* [14], the linear equation of the air motor torque and a

Gaussian function are also used to create the output power as well as the air consumption, respectively. This is somewhat different than the model used by Lemofouet *et al.* [43].

3.4.2 MPPT controller

Speed controller tuning

In terms of designing a speed controller for the SS-CAES, two PI controllers are designed and utilized for the inner current loop and the outer speed loop. The controllers are assumed to have data acquisition in the analogue-digital and digital-analogue converters and to have fast computational speed. A Bode diagram is used to specify the relevant gains of these controllers by reading both gain and phase margins values off the plot for achieving a stable speed controller.

For the inner current loop, the open loop transfer function cascaded with a low pass filter is discretized, using a zero-order hold (ZOH), and plotted on the Bode diagram. In this study, the gain margin 19 dB and phase margins 40° are selected by reading the values on the plot for ensuring the system's stability [96]. The Bode diagram of the inner current loop is shown in Fig. 3.17. As can be seen, the black line represents the open-loop of the inner current loop $G_{ip}(z)$, which is the uncompensated system. It is stabilized by cascading the PI controller $G_{ci}(z)$ shown by the red line of the stable open-loop $G_{ip}(z)G_{ci}(z)H_f(z)$; the compensated system achieves the gain and phase margins, satisfying the stability requirements.
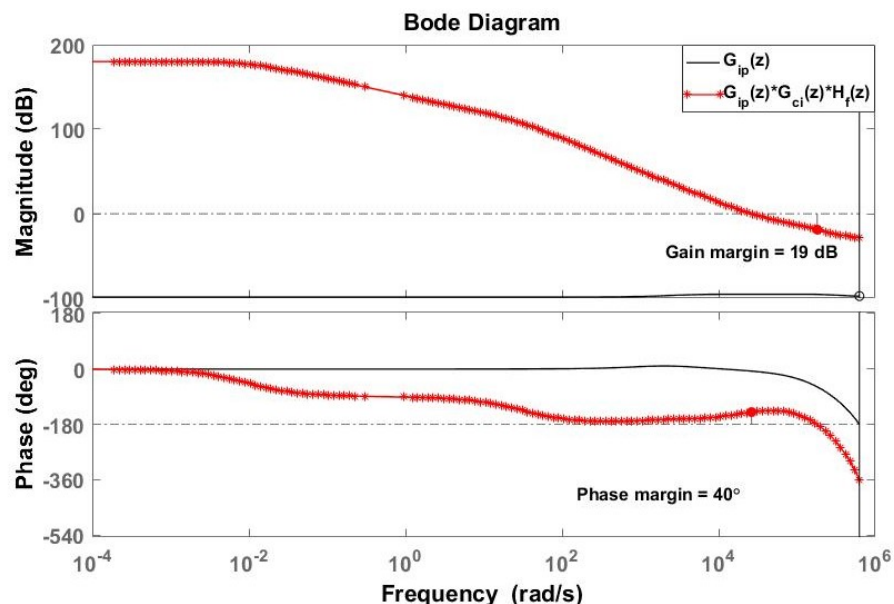
Figure 3.17 The Bode plot of the open loop transfer function of current

To stabilize the outer speed loop, the gain and phase margins are specified to be 33 dB and 60°, respectively. As can be seen on the Bode diagram in Fig. 3.18, the black line represents the open

loop of the outer loop $G_{\omega p}(z)$, which is the uncompensated system. It is stabilized by cascading the PI controller $G_{c\omega}(z)$ shown by the red line of the stable open loop $G_{\omega p}(z)G_{c\omega}(z)$; the compensated system achieves the gain and phase margins and hence satisfy the stability criteria, i.e., the system is stable.
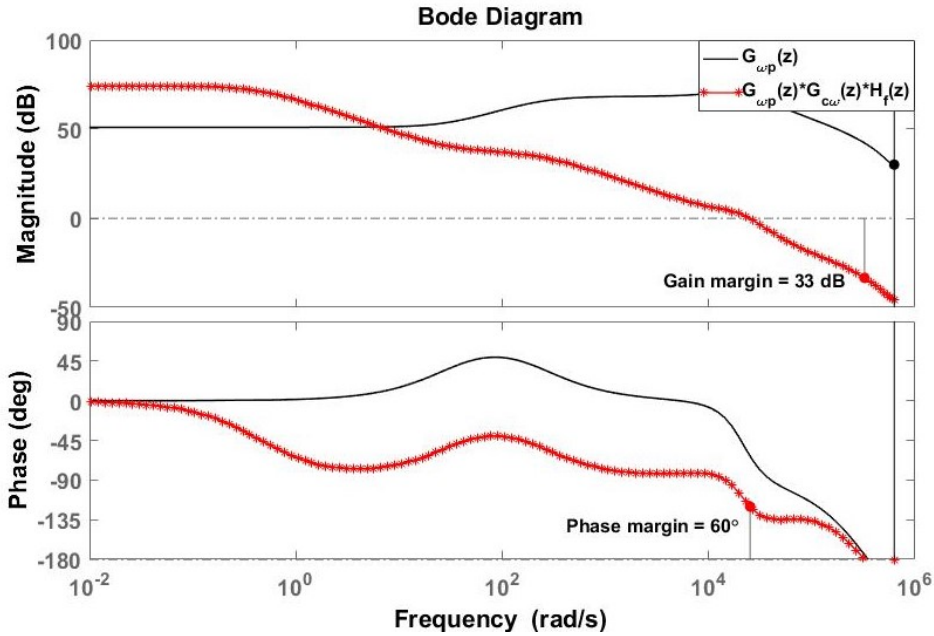
Figure 3.18 The Bode plot of the open loop transfer function of speed

This simulation has been done with the assumption of having an ideal gas in a large storage vessel as well as the discharging process being at isothermal conditions. Kinetic and friction losses are neglected. The inductor current is maintained by using the inner-loop PI controller with the low-pass filter for avoiding any noise in the inductor current signal. The model was simulated under two conditions, which are constant speed command and various speed command.

For the constant speed condition, the pressure changes from 6 to 4 and back to 6 bar again. The speed reference (blue line) is set constant at 150 rad/s. Fig. 3.19 illustrates the results of the speed and power. The speed PI controller also provides good results under varying pressure condition in order to maintain the actual speed (red line) at 150 red/s presented in the speed against time graph.
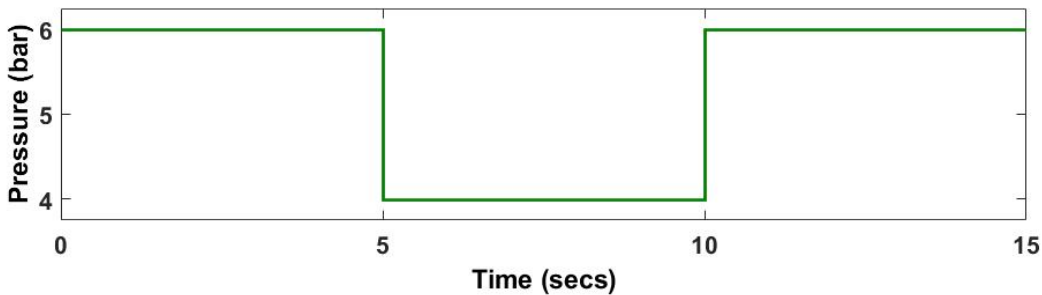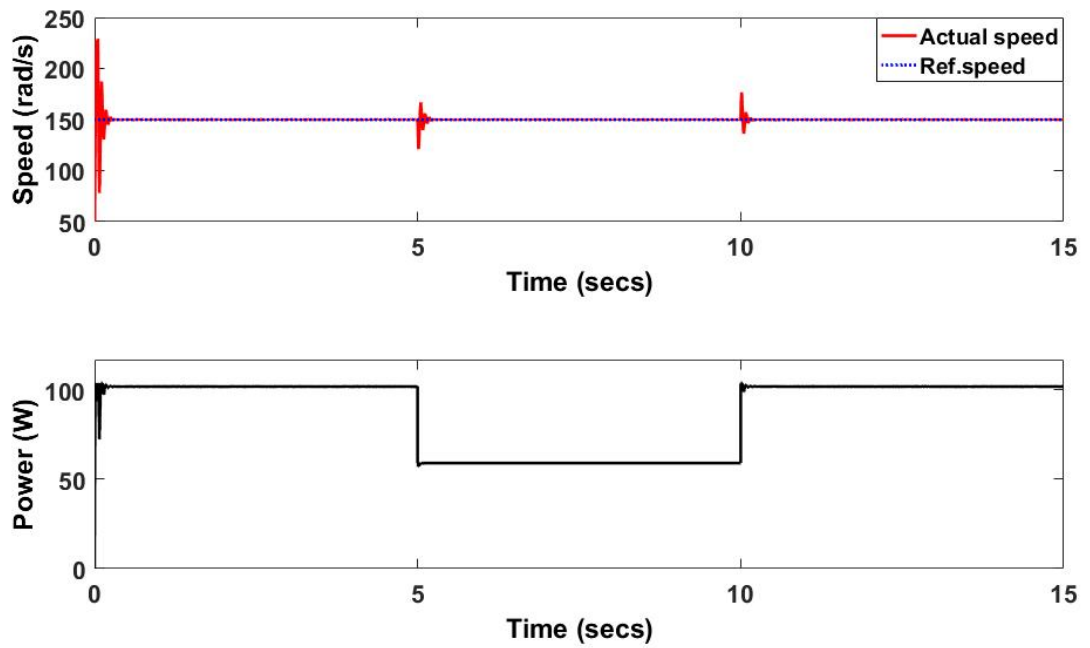
Figure 3.19 Results of SS-CAES under the condition of constant speed and varying pressure

Under varying speed reference condition, the pressure is set constant at 6 bar. The speed reference varies from 150 rad/s to 140 rad/s and then step up to 160 rad/s. The results of speed and power are achieved by using speed controller shown in Fig. 3.20. In the speed versus time graph, the red line represents the actual speed while the blue line donates the reference speed. Clearly, the speed PI controller has successfully controlled under varying speed reference condition at constant pressure of 6 bar.
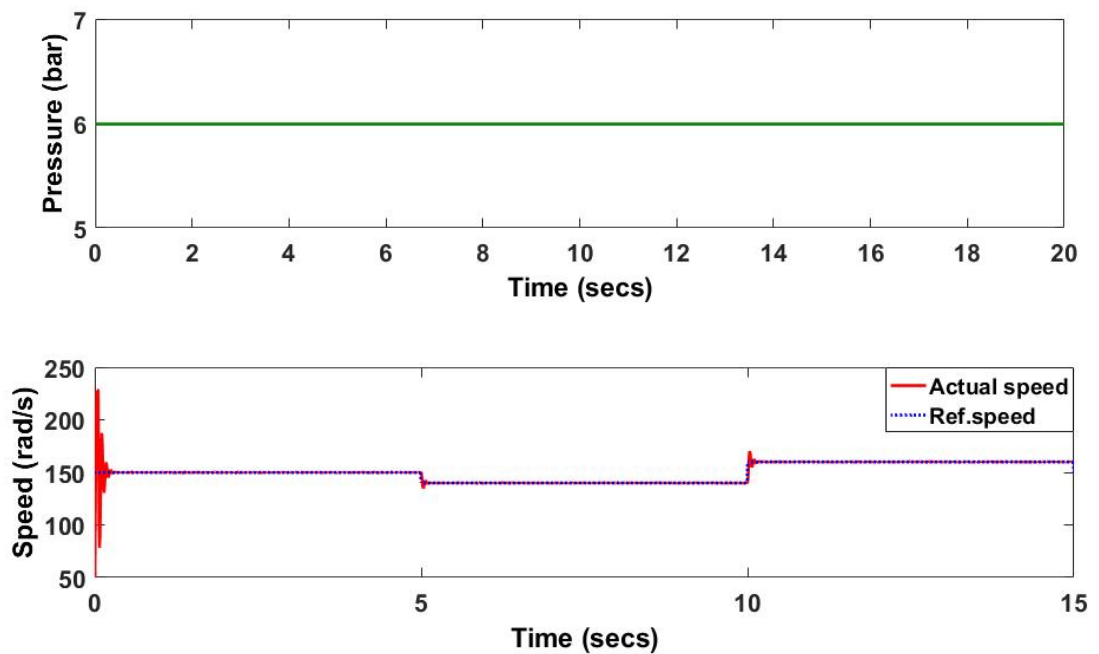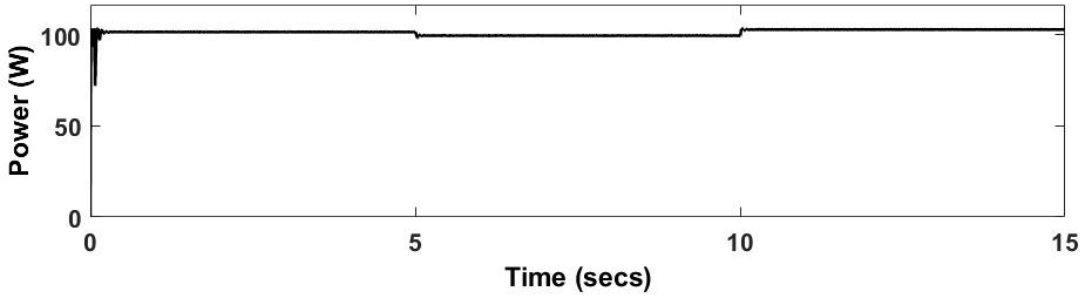
Figure 3.20 Results of SS-CAES under the condition of varying speed and constant pressure

Comparison between MEPT and MPPT controllers

The MPPT and MEPT controllers are compared for different speed operating points. Different speed point of these controllers can be plotted by using Eq. (3.37) and (3.40). Fig. 3.21 illustrates the maximum power and the maximum efficiency lines on the air motor characteristic curves. Clearly, the speed operating points of the MEP and MPP lines are different. These lines also rely strongly on pressure. In terms of the system efficiency, at constant pressure, the efficiency of the MEP is higher than that of the MPP by around 1-3%.
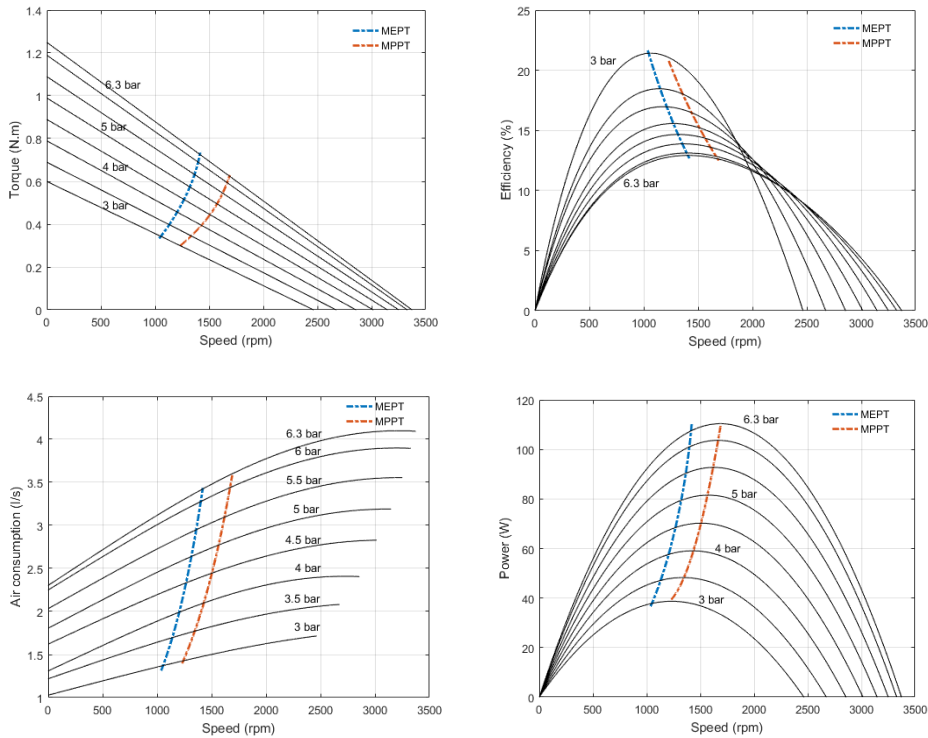
Figure 3.21 MPP and MEP lines on the air motor characteristic curves

Both MPPT and MEPT strategies are implemented with speed controller under constant and varying pressure conditions for testing the system performance. The system consists of an air motor, dc generator and boost converter connected to a constant resistive load. The results of the dynamic response of the air motor controlled by MEPT controllers under varying pressure conditions are

presented in Fig. 3.22. The pressure varies from 6 to 4 and then back to 6 bar again. It can be seen that the MEPT controller has effectively produced the reference speed (dashed blue). The red line represents the actual speed while the green line donates the maximum efficiency at each pressure.
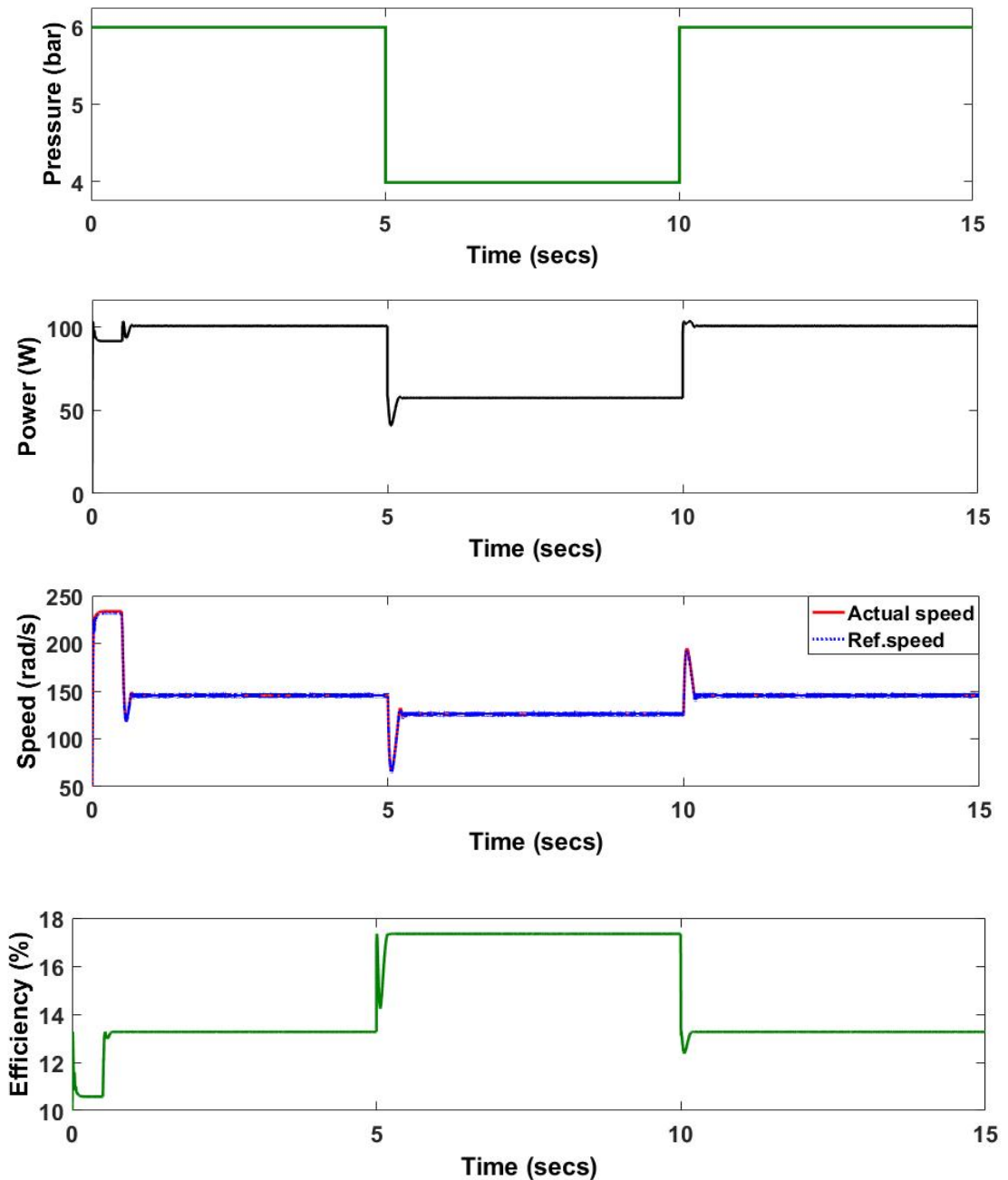
Figure 3.22 The results of the MEPT speed controller

For the MPPT controller under varying pressure conditions, Fig. 3.23 shows results for power, speed and efficiency. On the speed graph, the reference speed (dashed blue) is generated by estimating from half the free speed of the air motor. It controls the actual speed (red line) effectively. These can confirm that both MEPT and MPPT controllers have successfully generated the reference under this condition.
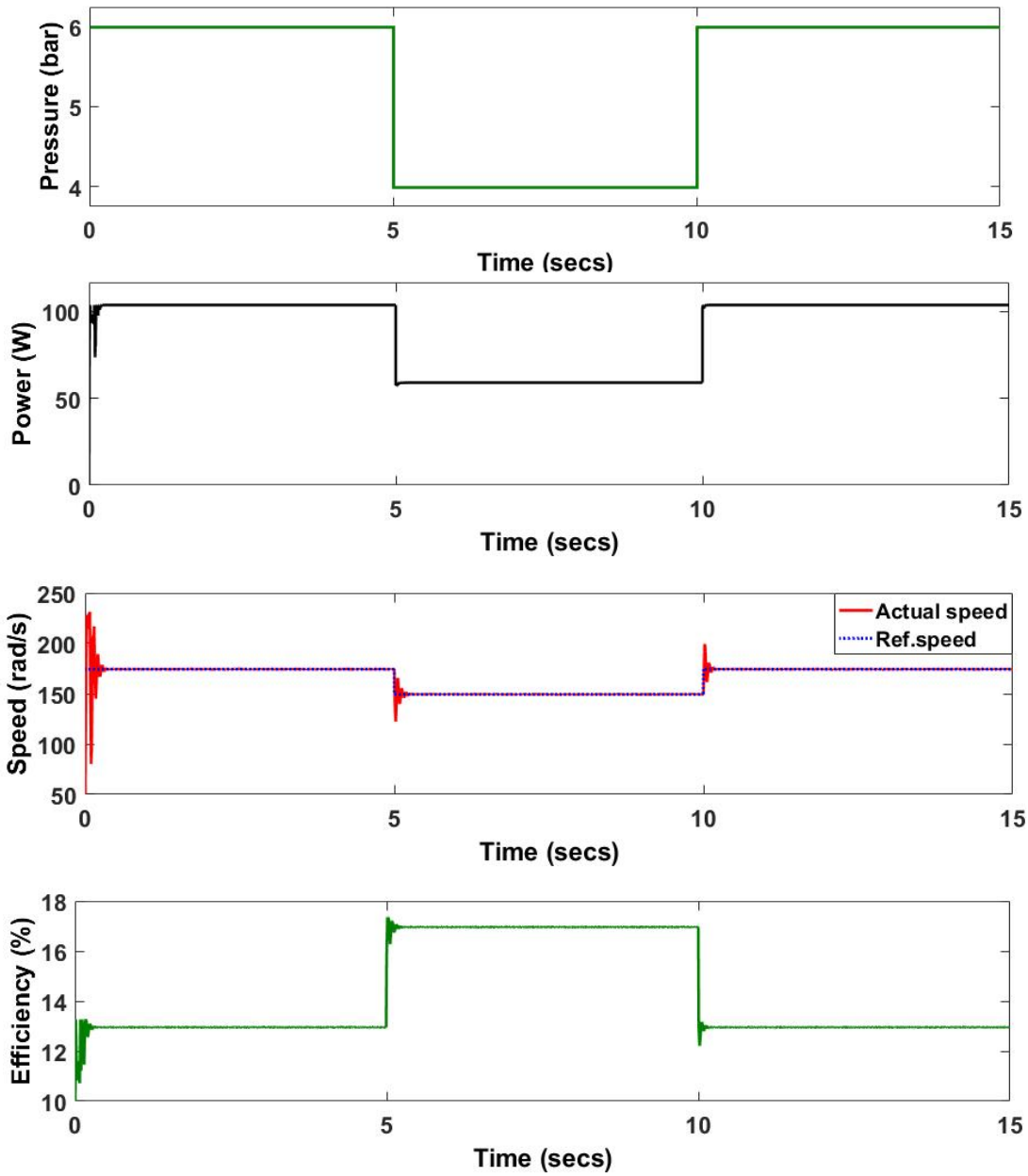
Figure 3.23 The results of the MPPT speed controller

For the constant pressure condition, the pressure of 6 bar is set as the input of the air motor. The speed, power and efficiency of the air motor controlled by MEPT and MPPT operating modes are presented in Fig. 3.24. Clearly, the actual speed, which is controlled by MEPT controller, is different from that controlled by MPPT controller.
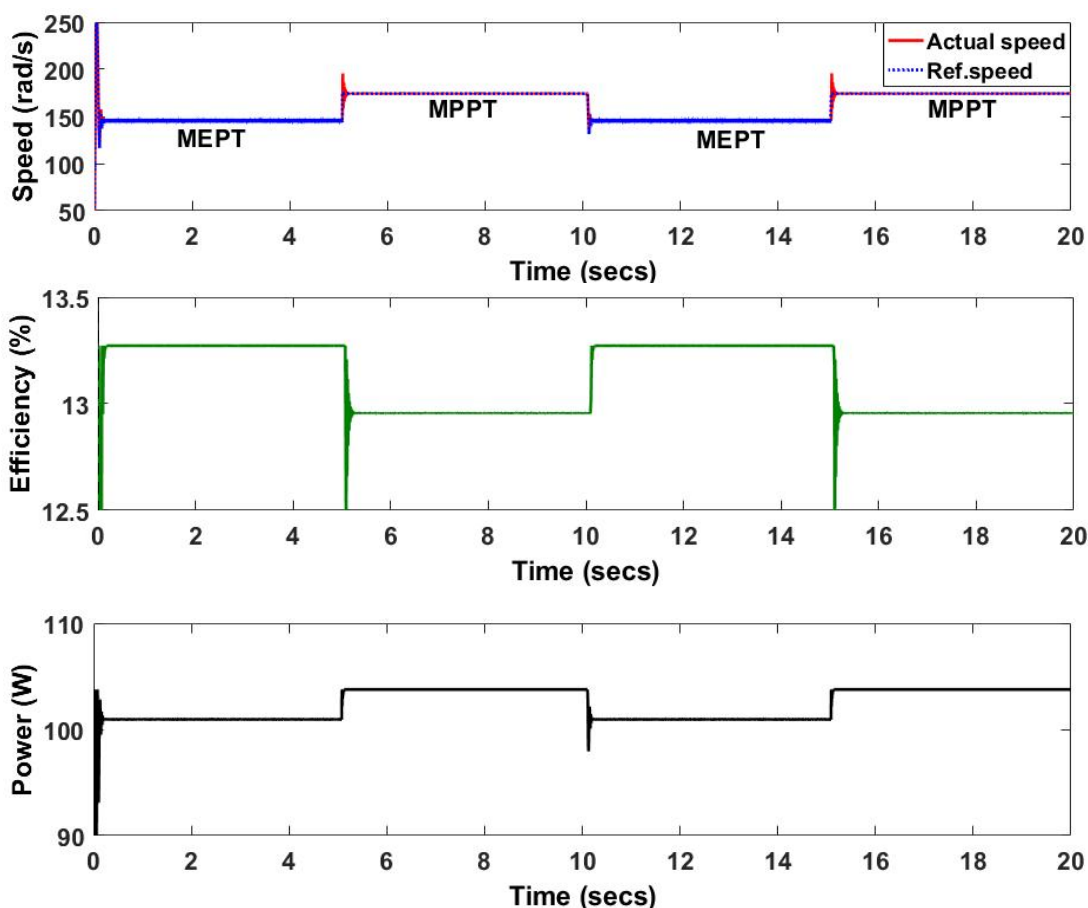
Figure 3.24 The results of the MEPT and MPPT speed controllers

MPPT controller

After successful tuning the speed controller and MEPT/MPPT comparison, the MPPT speed controller is used to control the SS-CAES operating at maximum power point. The model of the discharge process and the MPPT speed controller are implemented using Matlab/Simulink. The simulation is done under isothermal conditions and all losses are neglected. The load resistance is assumed to be constant. The MPPT algorithm is designed using the derivative of mechanical power (P_{am}) with respect to duty cycle (D) in order to identify the operating point of the air motor and adjust the speed to work at maximum power point. Fig.3.25 shows the simulation results of the SS-CAES system under varying pressure. In the speed versus time graph, the command speed is the blue line provided by the MPPT algorithm while the red line denotes the actual speed. Obviously, the actual speed operates at MPP of each pressure. It can be confirmed that the MPPT algorithm can produce the speed demand correctly when the pressure fluctuates from 6 to 4 to 3 to 5 and then back to 6 bar again.
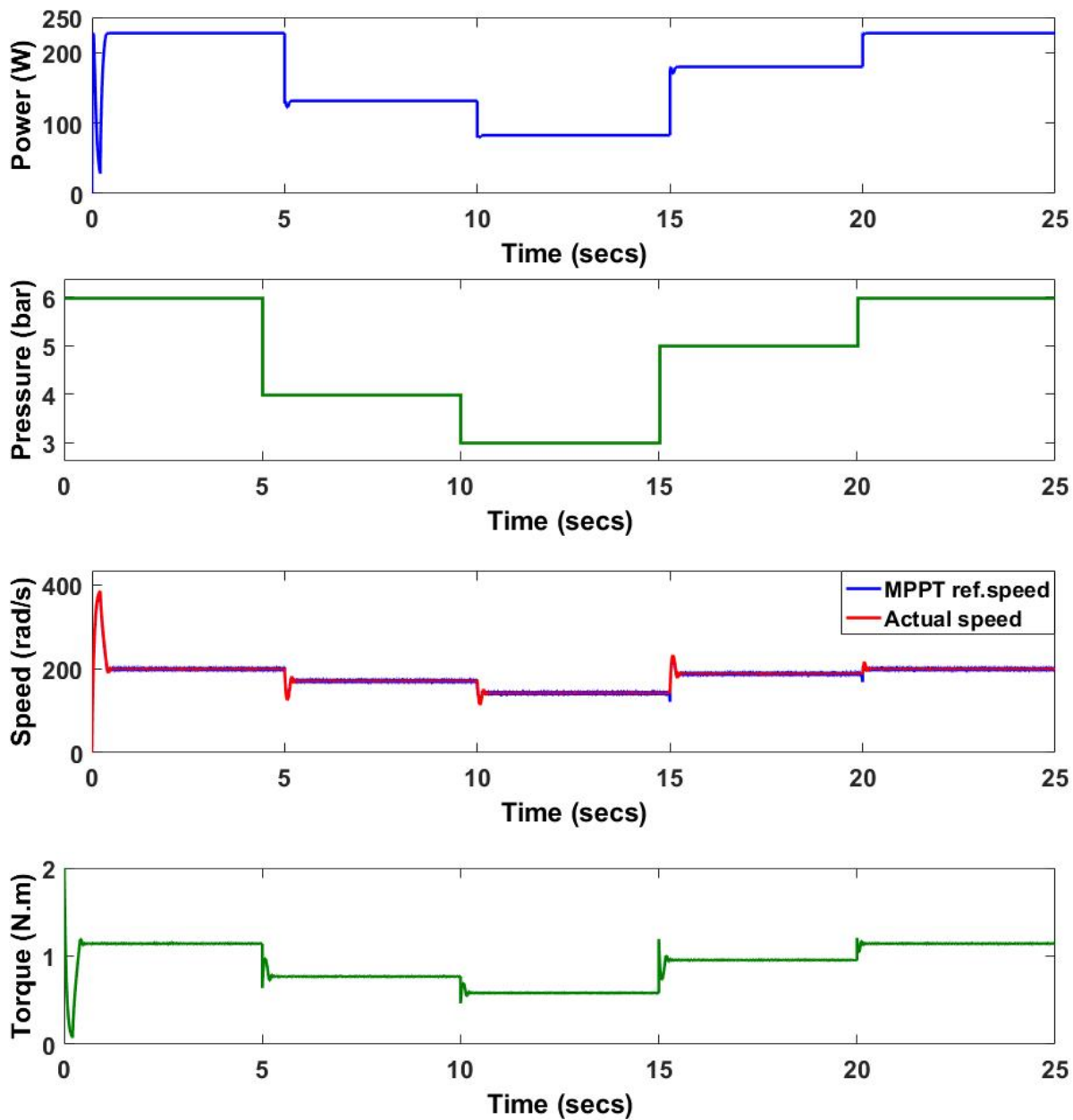
Figure 3.25 Results of the MPPT controller under changing pressure condition

3.5 Summary

This chapter focused on the SS-CAES system controlled by the MPPT speed controller within the discharge process. An air motor coupled with a PM DC generator was used and the output was controlled by a boost converter for supplying power to a constant resistive load. The speed regulator was applied for the air motor to control its speed.

The cascaded PI controller for the speed regulator was studied for controlling the speed of the generator, using a boost converter with the conditions of varying pressure and speed. For tuning the controller, the state-space averaging and small signal analysis were used to derive the transfer

functions, which was used to stabilise the system and select the proper parameter for the outer speed loop and inner-current loop. The criteria for system stability was a phase margin of 30°- 60° and a gain margin greater than 5 dB.

The maximum efficiency and maximum power point strategies were compared. The speed operating points of both controller types were different. They effectively controlled the actual speed at their speed operating points, which produced vary small difference in efficiencies. The efficiency of the MPPT was 1-3 % lower than that of the MEPT at the constant pressure of 6 bar. However, the MEPT strategy needs accurate characteristics of the air motor since the non-linear nature of the air motor as well as the sensors for pressure and speed measurement affect the results. Moreover, the MEPT strategy is difficult in terms of real-time measurements and implementation. To avoid these advantages, the MPPT algorithm is interesting as an alternative strategy due to its requirement for lower number of sensors and no prior knowledge of the air motor characteristics. The MPPT is easy for real time tracking since it measures the output power directly.

To track the maximum power, the speed reference of the air motor was calculated based on the perturb and observe method. The derivative of mechanical power with respect to duty cycle was used to calculate the speed operating point for reaching maximum power point. To implement the duty cycle of the boost converter, it needs to be designed within limitation of the practical range, i.e., between 95% to 5%. The MPPT controller showed good performance to control the air motor speed at the MPP. However, the system has a very narrow maximum efficiency peak. A small deviation from the MPPT results in considerably loss of efficiency. These issues can be improved by adding another energy storage such as a battery which can buffer fast load fluctuations while the CAES air motor operates at its MPP. The next chapter investigates a hybrid CAES system with a battery.

Chapter 4   Hybrid SS-CAES-Battery System

This chapter presents the proposed hybrid energy storage (HES) system comprising a SS-CAES during the discharge process as illustrated in Fig. 4.1. As the SS-CAES system with the MPPT controller are presented in Chapter 3, this chapter commences with a review of the battery system. The voltage controllers are then designed for the battery connected to a bidirectional converter and the SS-CAES in conjunction with a boost converter. Next, household load demands in all seasons are compared and selected for estimating both air motor and battery sizes for a typical household in the Southern region of the UK. Finally, simulation results of the proposed system are presented to show the performance of the HES system by comparison with the SS-CAES only system controlled by a voltage controller.
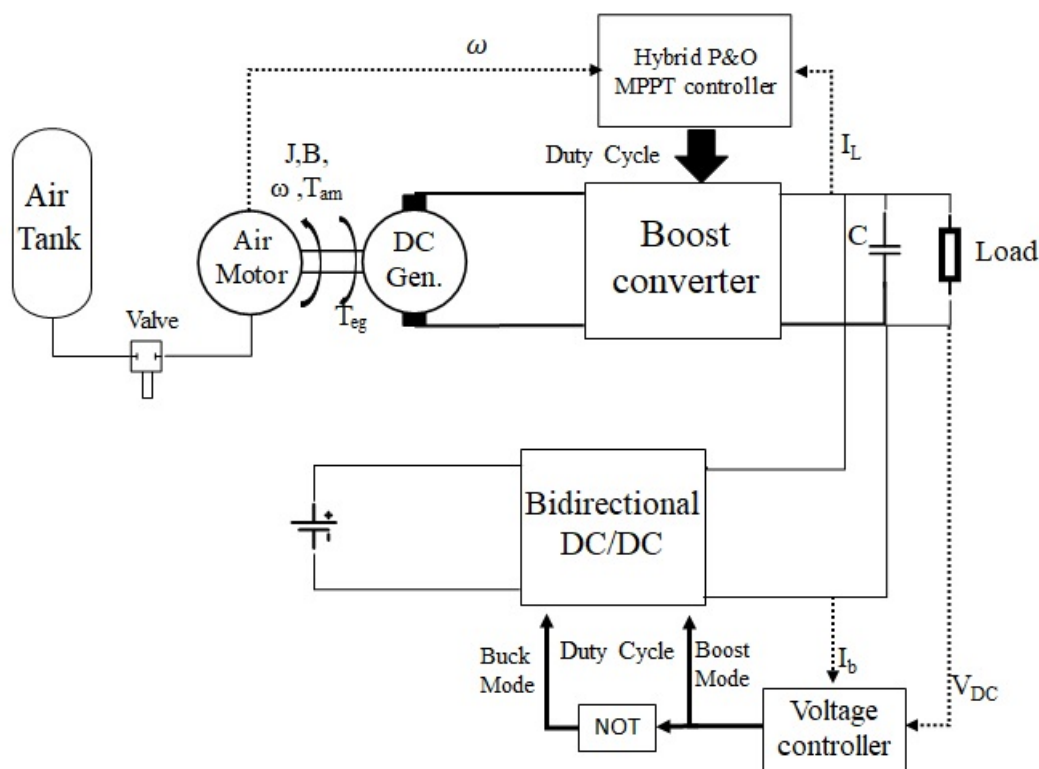
Figure 4.1 Configuration of the systems with the controllers

4.1 Review of battery system

The battery is a type of the energy storage device which has been used for more than a century in several applications. The principle of the battery is to convert electrical energy into chemical energy when it charges and vice versa when it discharges [98]. It has been investigated intensively especially the electrode materials and electrolytes for improving cost, energy and power densities,

battery safety and life cycle [99]–[103]. Currently, there are three main types of Lead-acid, Lithium-ion (Li-ion) and Nickel batteries.

Lead-acid batteries, which are the oldest and most developed, are rechargeable. This battery type is still used for small-medium scale storage applications [51]. The lead-acid batteries are employed in 75% of photovoltaic systems and around 70% of this battery type are used in vehicles [104], [105]. It has a lot of advantages such as low cost, high reliability, simplicity of manufacture and high efficiency (70-90%) [3], [24], [51], [106]. However, this battery type uses a heavy metal component which is not environmental friendly. It also has low energy density (30-50 Whr/kg) and short cycle life (500-100 cycles), which is poor for power management. Moreover, it requires a temperature management system since it has a poor temperature performance [3].

Nickel batteries are classified as secondary batteries with better performance than Lead-acid batteries such as having a higher energy density (50-75 Whr/kg) and a longer life (2000-2500 cycles) [24], [51]. Among this battery type, Nickel-Cadmium (Ni-Cd) and Nickel-Metal Hydride (NI-MH) batteries are most developed and widely used in the market [24]. The Ni-Cd battery has been used as a powerful battery bank with a power rating of 27 MW while the Ni-MH battery is used in over 95% hybrid electric vehicles such as the Toyota Prius and Camry [107]–[110]. However, Ni-Cd battery is expensive because of the high cost of its industrial process. Moreover, Cadmium is a toxic heavy metal, which has a negative environmental impact [3], [51].

The Lithium battery plays an important role in electrical energy storage, especially in plug-in hybrid electric vehicles [33], [111]. The advantages of this battery type are high efficiency (> 95%), high energy density (75-200 Wh/kg), long life cycle (~10,000 cycles at 60% DOD), plentiful and inexpensive cathode material which make it a promising technology for portable applications [3], [24], [51], [112]–[115]. In contrast, the high cost of the battery for large-scale applications is a significant obstacle comparing with other types of batteries since it needs special packaging and internal circuitry for its protection and safety [116].

These batteries are most widely used as a rechargeable device for many applications and household. It is combined with other ESS or/and renewable energy (RE) technologies for improving the system capabilities and reliability. The investigation of hybridisation of battery with other energy storage systems (ESS) and RE technologies has been done over the past decades. The possible HES configurations based on a battery are presented as supercapacitor/battery, fuel-cell/battery, superconducting magnetic energy storage/battery and CAES/battery [52], [58]. The battery is used to charge and discharge power in a hybrid system. Battery also seems to be a common storage system implemented in the RE technologies such as wind and solar systems [117],

[118], [127], [119]–[126]. Therefore, a controller is required to manage the battery operation, as illustrated in the next section.

4.2 Voltage controller

A battery with a bidirectional converter is used to overcome storage problems associated with a SS-CAES system. The battery is used to discharge power when the load is greater than the generating power and to charge the excess power otherwise. For considering the performance of the hybrid system, a voltage controller is designed for the battery with a bidirectional converter and the SS-CAES system with a boost converter.

4.2.1 Voltage controller for the battery with a bidirectional converter

A small-signal model of the cascade voltage controller

The dynamic characteristics of a bidirectional converter need to be analyzed in order to understand the system and produce a design based on the small-signal model. The voltage variable source is observed regardless of the direction of the power flow. The circuit diagram of the bidirectional converter model is presented in Fig. 4.2, which enables both positive and negative current flow from/to the battery.
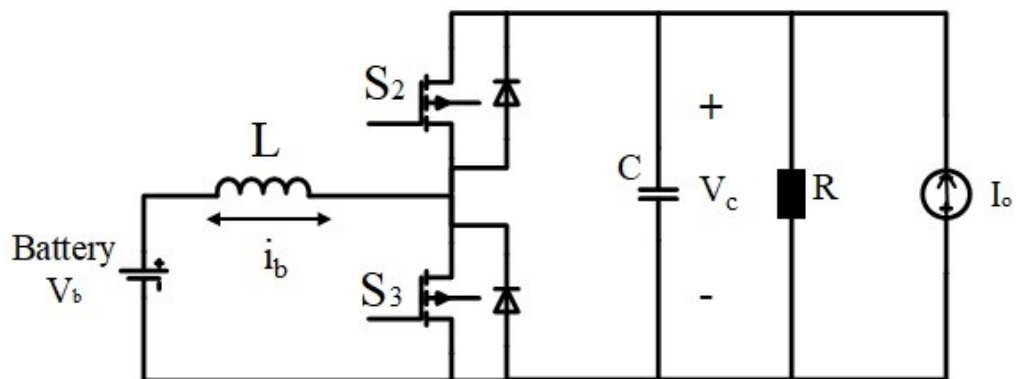
Figure 4.2 Bidirectional DC converter with output variable source

The converter acts as a boost converter during the discharging process while working as a buck converter during charging process. For this study, the internal resistance is assumed to be constant as and the temperature effect is neglected. To design the voltage controller, the state-space model is used for obtaining an expression for the transfer function of the converter. In order to obtain this transfer function by analyzing the dynamics of the converter under steady state condition, the switching operation needs to be considered. When the MOSFET S_3 is switched on and S_2 is switched off, the circuit diagram can be presented as:
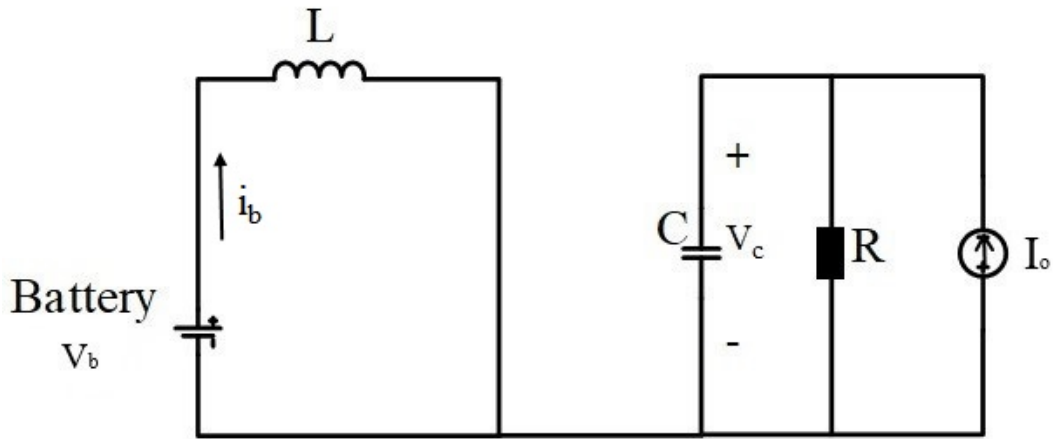
Figure 4.3 Bidirectional converter when MOSFET S$_3$ is on, S$_2$ is off

The state vector and the input vector for this bidirectional converter are defined by $[i_b \quad v_C]$ and $[V_b \quad I_o]$, respectively. Using Kirchhoff's voltage (KVL) and current laws (KCL), the equations are given by:

$$V_b - L \frac{di_b}{dt} = 0 \tag{4.1}$$

$$I_o - C \frac{dv_C}{dt} - \frac{v_C}{R} = 0 \tag{4.2}$$

Rearranging for state-space equation in matrix form of the first switching configuration:

$$\frac{d}{dt}\begin{bmatrix} i_b \\ v_C \end{bmatrix} = \begin{bmatrix} 0 & 0 \\ 0 & -1/RC \end{bmatrix}\begin{bmatrix} i_b \\ v_C \end{bmatrix} + \begin{bmatrix} 1/L & 0 \\ 0 & 1/C \end{bmatrix}\begin{bmatrix} V_b \\ I_o \end{bmatrix} \tag{4.3}$$

Then, the state coefficient matrix can be given by

$$A_1 = \begin{bmatrix} 0 & 0 \\ 0 & -1/RC \end{bmatrix} ; B_1 = \begin{bmatrix} 1/L & 0 \\ 0 & 1/C \end{bmatrix} \tag{4.4}$$

On the other hand, the circuit diagram when the MOSFET S_3 is switched off and S_2 is switched on can be shown as:
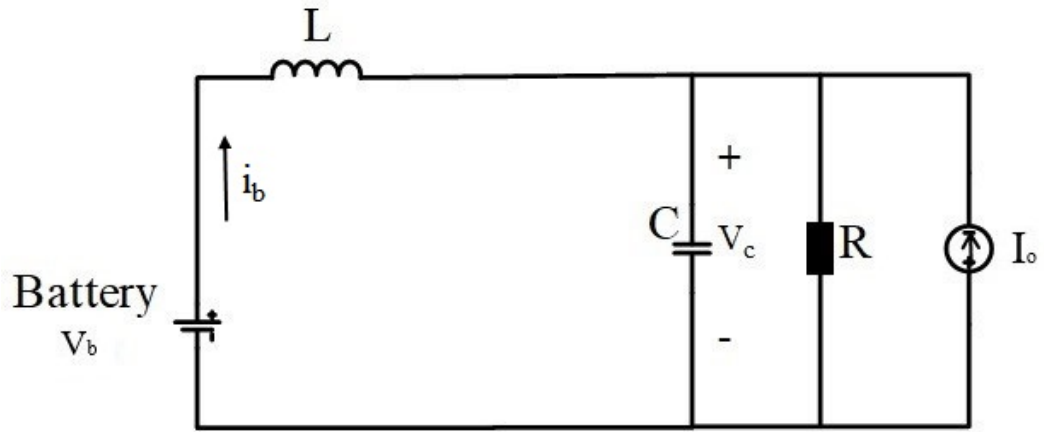
Figure 4.4 Bidirectional converter when MOSFET S$_3$ is off, S$_2$ is on

The KVL and KCL are also applied in the topology give:

$$V_b - L\frac{di_b}{dt} - V_C = 0 \tag{4.5}$$

$$i_b + I_o - C\frac{dV_C}{dt} - \frac{V_C}{R} = 0 \tag{4.6}$$

Rearranging for state-space equation in matrix form of the second switching configuration:

$$\frac{d}{dt}\begin{bmatrix} i_b \\ v_C \end{bmatrix} = \begin{bmatrix} 0 & -1/L \\ 1/C & -1/RC \end{bmatrix}\begin{bmatrix} i_b \\ v_C \end{bmatrix} + \begin{bmatrix} 1/L & 0 \\ 0 & 1/C \end{bmatrix}\begin{bmatrix} V_b \\ I_o \end{bmatrix} \tag{4.7}$$

Therefore, the state coefficient matrix of this switch are given by

$$A_2 = \begin{bmatrix} 0 & -1/L \\ 1/C & -1/RC \end{bmatrix} ; B_2 = \begin{bmatrix} 1/L & 0 \\ 0 & 1/C \end{bmatrix} \tag{4.8}$$

The system output is assumed to coincide with the state vector. As a results, $C_1 = C_2 = I$ which is the identical matrix. The average state-space equations can be calculated by using expression of duty cycle (d): $A = A_1D + A_2(1 - D), B = B_1D + B_2(1 - D)$. Therefore, the average state-space matrices can be given as follow.

$$A = \begin{bmatrix} 0 & -(1-D)/L \\ (1-D)/C & -1/RC \end{bmatrix} \tag{4.9}$$

$$B = \begin{bmatrix} 1/L & 0 \\ 0 & 1/C \end{bmatrix} \tag{4.10}$$

The steady-state DC solution for the system can be obtained by

$$X = -A^{-1}BV_{in}$$

$$X = - \begin{bmatrix} 0 & -(1-D)/L \\ (1-D)/C & -1/RC \end{bmatrix}^{-1} \begin{bmatrix} 1/L & 0 \\ 0 & 1/C \end{bmatrix} \begin{bmatrix} V_b \\ I_o \end{bmatrix}$$

$$= \begin{bmatrix} V_b/R(1-D)^2 - I_o/(1-D) \\ V_b/(1-D) \end{bmatrix} \tag{4.11}$$

Therefore, each component can be expressed as:

$$I_b = \frac{V_b}{R(1-D)^2} - \frac{I_o}{1-D} \tag{4.12}$$

$$V_C = \frac{V_b}{1-D} \tag{4.13}$$

For a small-signal analysis, the open-loop transfer functions of each output variable control are derived as follows.

Duty cycle-to-output voltage small-signal open-loop transfer function(G_{vdb})

For this converter $B_1 = B_2$ and $C_1 = C_2$, i.e., the formula of $G_{vdb}(s)$ can be obtained from the second row of the matrix:

$$G_{vdb}(s) \triangleq \frac{\hat{V}_{out}(s)}{\hat{D}(s)} = C(sI-A)^{-1}[(A_1-A_2)X + (B_1-B_2)V_{in}] + (C_1-C_2)X$$

$$= \frac{1}{s^2 + \frac{1}{RC}s + \frac{(1-D)^2}{LC}} \begin{bmatrix} \left(\frac{V_b}{L(1-D)}\right)\left(s + \frac{1}{RC}\right) + \left(\frac{1-D}{LC}\right)\left(\frac{V_b}{R(1-D)^2} - \frac{I_o}{1-D}\right) \\ \left(\frac{I_o}{1-d} - \frac{V_b}{RC(1-D)^2}\right)s + \left(\frac{V_b}{LC}\right) \end{bmatrix}$$

$$= \frac{\left(\frac{I_o}{1-d} - \frac{V_b}{RC(1-D)^2}\right)s + \left(\frac{V_b}{LC}\right)}{s^2 + \frac{1}{RC}s + \frac{(1-D)^2}{LC}} \tag{4.14}$$

Duty cycle-to-inductor current small-signal open-loop transfer function(G_{idb})

As $B_1 = B_2$ for this converter, the duty cycle-to-inductor current open-loop transfer function $G_{idb}(s)$ can be obtained by taking only the first row of the matrix. The formula of $G_{id}(s)$ can be defined by:

$$G_{idb}(s) \triangleq \frac{\hat{I}_b(s)}{\hat{D}(s)} = (sI-A)^{-1}[(A_1-A_2)X + (B_1-B_2)V_{in}]$$

$$= \frac{1}{s^2 + \frac{1}{RC}s + \frac{(1-D)^2}{LC}} \begin{bmatrix} \left(\frac{V_b}{L(1-D)}\right)\left(s + \frac{1}{RC}\right) + \left(\frac{1-D}{LC}\right)\left(\frac{V_b}{R(1-D)^2} - \frac{I_o}{1-D}\right) \\ \left(\frac{I_o}{1-d} - \frac{V_b}{RC(1-D)^2}\right)s + \left(\frac{V_b}{LC}\right) \end{bmatrix}$$

$$= \frac{\left(\frac{V_b}{L(1-D)}\right)\left(s + \frac{1}{RC}\right) + \left(\frac{1-D}{LC}\right)\left(\frac{V_b}{R(1-D)^2} - \frac{I_o}{1-D}\right)}{s^2 + \frac{1}{RC}s + \frac{(1-D)^2}{LC}} \tag{4.15}$$

Inductor current -to-output voltage small-signal open-loop transfer function(G_{vib})

This transfer function can be developed properly for closed loop system design after achieving the various transfer functions. Thus, the $G_{vi}(s)$ can be expressed as:

$$G_{vib}(s) \triangleq \frac{\hat{V}_{out}(s)}{\hat{I}_b(s)} = \frac{G_{vdb}(s)}{G_{idb}(s)} = \frac{\hat{V}_{out}(s)}{\hat{D}(s)} \cdot \frac{\hat{D}(s)}{\hat{I}_b(s)}$$

$$= \frac{\left(\frac{I_O}{1-d} - \frac{V_b}{RC(1-D)^2}\right)s + \left(\frac{V_b}{LC}\right)}{\left(\frac{V_b}{L(1-D)}\right)\left(s + \frac{1}{RC}\right) + \left(\frac{1-D}{LC}\right)\left(\frac{V_b}{R(1-D)^2} - \frac{I_O}{1-D}\right)} \tag{4.16}$$

Fig. 4.5 illustrates the close-loop feedback of the cascaded voltage control design for the battery in the discharge (boost) mode.
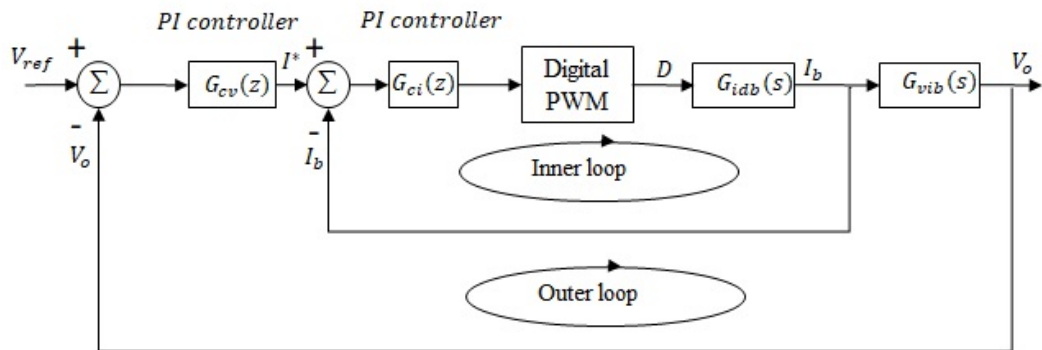
Figure 4.5 Block diagram of the transfer function of battery with a bidirectional converter

The voltage control of the system is designed with two control loops, which are the inner current loop and the outer voltage loop. The outer voltage loop is used to maintain the error of the output voltage as close to zero as possible by providing the inductor current reference to the inner-current loop, which provides the duty cycle to maintain a constant inductor current i_b. The control stability needs to be studied, which is carried out for the open-loop transfer function.

For the inner current loop, the PI controller is used to ensure that the inductor current has zero error. The controller provides the duty cycle to maintain a constant inductor current i_b. The design can be done by using the open-loop transfer function of the inductor current based on the Mason's rules [97]. This transfer function is expressed as:

$$G_{ib}(s) = \frac{I_b(s)}{D(s)} = G_{idb}(s) \tag{4.17}$$

This open-loop transfer function is cascaded with a digital low pass filter in order to modify the control strategy in a flexible manner. The low pass filter is expressed by

$$H_f(z) = \frac{1 - e^{\omega_{cf}T_{sc}}}{z - e^{\omega_{cf}T_{sc}}} \tag{4.18}$$

Where ω_{cf} is the cut-off frequency and T_{sc} is the sampling period.

For the outer voltage loop, PI controller is used to maintain the error of the voltage as close to zero as possible by providing the inductor current reference I^* to the inner-current loop. To stabilize the output voltage, the open loop transfer function of the outer voltage loop, which is included the inner loop controller, can be presented by

$$G_{vb}(s) = \frac{V_o(s)}{I^*(s)} = \frac{G_{ci}(s)G_{idb}(s)G_{vib}(s)}{1+G_{ci}(s)G_{idb}(s)H_f(s)} \tag{4.19}$$

To stabilize both PI controllers, the transfer functions is plotted on the bode diagram in order to specify the gain and phase margins of the control system.

Voltage controller model for the battery

A voltage controller is designed for the battery such that the bidirectional converter absorbs and delivers transient power during power fluctuation while the output voltage is kept constant. Fig. 4.6 illustrates the control scheme of the battery with a bidirectional converter. The voltage (V_{bus}) is measured and compared with the voltage reference (V_{ref}). This error is minimized by a PI controller, which sets the current reference (I_{bref}) of the inner loop. The reference value is limited by the charging (I_{ch}) and discharging current (I_{disch}) rating that is obtained from the datasheet for safety reason. The error between the reference and battery current (I_b) is applied to PI regulator. The output signal is the duty cycle D_1 for transistor S_2 (buck mode) or D_2 for transistor S_3 (boost mode), respectively. The duty cycle D_1 is generated while D_2 is stopped in the buck mode and vice versa.
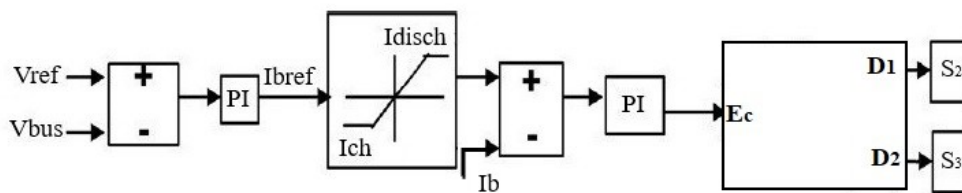
Figure 4.6 Modelling of the battery voltage controller

4.2.2 Voltage controller for SS-CAES

Voltage control design

As mentioned in Section 4.1, the performance of the system needs to be compared within two scenarios. A first scenario is a CAES only system controlled in constant voltage mode that the voltage controller needs to be designed. Fig. 4.7 shows the block diagram of the cascade voltage

control design for the boost converter connected to the SS-CAES, which contains two control loops. C_1 and C_2 are the controllers for the outer voltage and the inner current loops, respectively. $G_{id}(s)$ and G_{st} are the two linear transfer functions, which are achieved from Eq. (3.26) and (3.28) in Chapter 3.
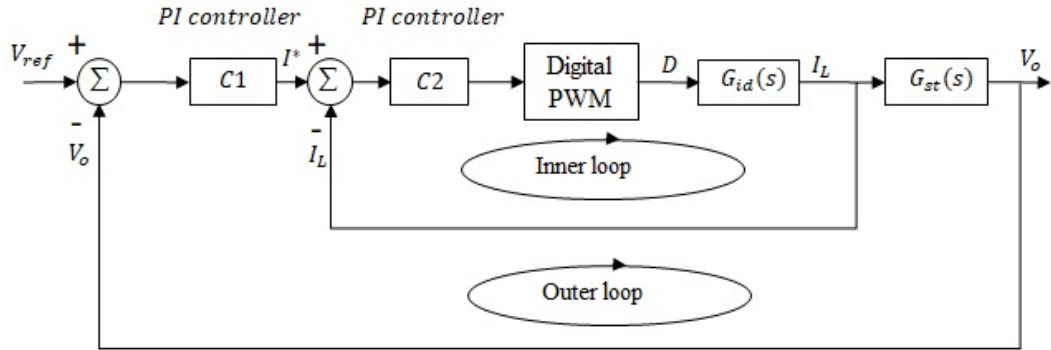
Figure 4.7 Block diagram of the voltage controller

As a grid-disconnected mode, the control of the system is designed with two control loops, which are the inner current loop and the outer voltage loop. The outer voltage loop is used to maintain the error of the output voltage as close to zero as possible by providing the inductor current reference to the inner-current loop, which provides the duty cycle to maintain a constant inductor current i_L. To stabilize both PI controllers, the transfer functions is plotted on the bode diagram in order to specify the gain and phase margins of the control system.

For the inner current loop, the design can be done by using the open-loop transfer function of the inductor current based on the Mason's rules [97]. The transfer function of the duty cycle to the inductor current $G_{ip}(s)$ is expressed as:

$$G_{ip}(s) = \frac{I_L(s)}{D(s)} = G_{id}(s) \tag{4.20}$$

For stabilizing the output voltage loop, the open loop transfer function of the outer voltage loop $G_{vp}(s)$, which is included the inner loop controller, can be presented by

$$G_{vp}(s) = \frac{V_o(s)}{I^*(s)} = \frac{G_{ci}(s)G_{id}(s)G_{st}(s)}{1+G_{ci}(s)G_{id}(s)H_f(s)} \tag{4.21}$$

To stabilize both PI controllers, the transfer functions is plotted on the bode diagram in order to specify the gain and phase margins of the control system.

Voltage controller model for SS-CAES
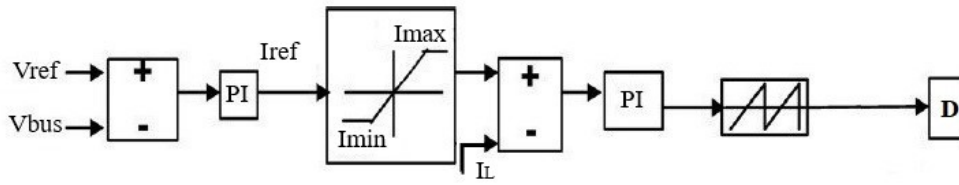
Figure 4.8 Modelling of CAES voltage controller

A voltage controller is designed for the CAES connected to a boost converter. Fig. 4.8 illustrates the block diagram of the CAES voltage controller. The voltage (V_{bus}) is detected and compared with the voltage reference (V_{ref}). The error between these two values is applied to a PI controller, which generates the current reference (I_{ref}) of the inner loop. The CAES current (I_L) will be regulated to its reference value (I_{ref}) by the PI controller. The duty cycle, which is the output signal, is then generated accordingly. Due to the output voltage being kept constant by this controller, the air motor speed will be varied in order to generate the current for the load demand.

The efficiency of the air motor is calculated by using Eq. (3.37) when the systems connect to the constant load. In this case, the speed operating point can be used to determinen the efficiency of the air motor in both controlling modes. The efficiency of the air motor controlled by the MPPT controller is compared by one operated in the voltage mode. The improvement of the efficiency in percentage can be calculated by:

$$\frac{\eta_{am,MPPT} - \eta_{am,Voltage}}{\eta_{am,MPPT}}$$

(4.22)

4.3 Sizing of the discharging components

The component-sizing procedure is assumed for a stand-alone hybrid system with the proposed structure in Fig.4.1, for a household electricity supply in the Southern region of the UK. The purpose is to estimate proper size of the system components to ensure the reliability of the electricity supply. Hence, the cost effectiveness is not considered. The maximum hourly demand powers in four seasons for a typical home in the County of Hampshire and the Isle of Wight are used as a case study collected by Rushby *et al* [128] as shown in Fig. 4.9. They are selected by considering from the highest power demand during a day in each seasons. The red line represents the hourly maximum power demand in winter season while purple, black and blue lines donate the hourly maximum demands in summer, spring and autumn seasons, respectively.
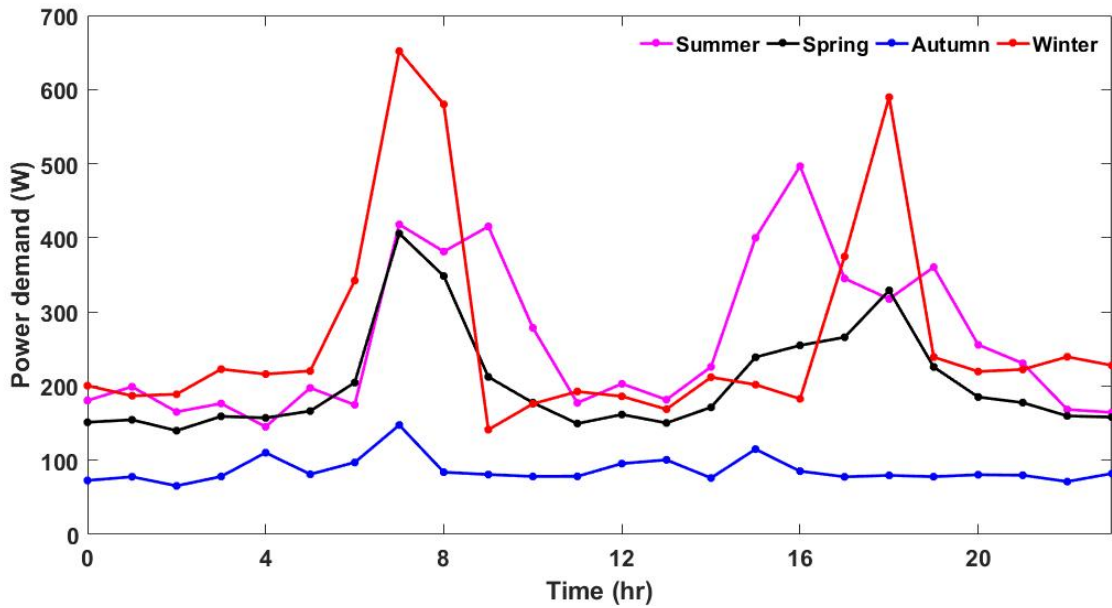
Figure 4.9 Maximum hourly household power demand in the Southern region of the UK [128]

The demand power has the high demands in the morning (around 6 -10 hrs) and in the evening (16-20 hrs). The highest peak demands are in winter while the power demand in autumn is small. To select the data of the power demand for sizing the air motor and battery, the total amounts of the power demands of the days in all seasons are calculated as presented in Table 2. It is clearly that the total power demand of a day in winter is greatest, which is around 6.4 kW, while the total power need of a day in autumn is smallest, approximately 2.075 kW. To determine the air motor and battery sizes, the total power demand of a day in winter is chosen since the system's size estimated by using this data can cover the power demand during a year.

In this case, the SS-CAES system is assumed to discharge constantly at the maximum power point under isothermal process condition. The operating pressure of 20 bar is selected in this paper. The different power ratings of the air motor, obtained from commercial companies, are used for air motor and battery sizing. When the power demand is greater than the CAES power, the difference between the generated power (P_{CAES}) and demand power (P_{dem}), called energy deficit (ED), is used for battery sizing. The battery needs to compensate for the insufficient power to satisfy the power demand. The battery must cover the energy deficit (ED) [18]:

$$ED(t) = \int (P_{CAES}(t) - P_{dem}(t)) \cdot dt \qquad (4.23)$$

where $P_{CAES}(t) < P_{dem}(t)$ at time t. All system models in this paper are implemented using MATLAB/Simulink. Details of the system parameters are listed in Appendix C.

Hours of a day	Power demand (W)			
	Summer	Autumn	Winter	Spring
1	180.7	72.9	200.7	151.4
2	199.3	77.8	187.0	154.7
3	165.4	65.6	189.2	140.1
4	176.7	78.2	223.0	159.3
5	145.3	110.4	216.3	157.3
6	197.7	81.2	220.6	166.5
7	174.9	97.2	342.5	204.9
8	418.2	147.6	651.9	405.9
9	381.6	84.0	580.1	348.6
10	415.4	80.9	141.3	212.5
11	278.7	78.3	176.2	177.7
12	177.5	78.4	192.8	149.6
13	203.3	95.7	186.3	161.8
14	181.8	100.6	168.9	150.4
15	226.1	76.2	212.1	171.5
16	400.2	115.1	202.1	239.1
17	496.8	85.4	183.0	255.1
18	345.3	77.8	374.9	266.0
19	317.6	79.7	589.9	329.1
20	360.5	78.0	239.3	225.9
21	255.9	80.6	219.8	185.4
22	230.9	79.9	222.6	177.8
23	168.6	71.4	239.6	159.9
24	164.6	82.2	228.1	158.3
Total	6263.0	2075.1	6388.2	4908.8

Table 2 Hourly demand power in four seasons

4.4 Power split optimisation
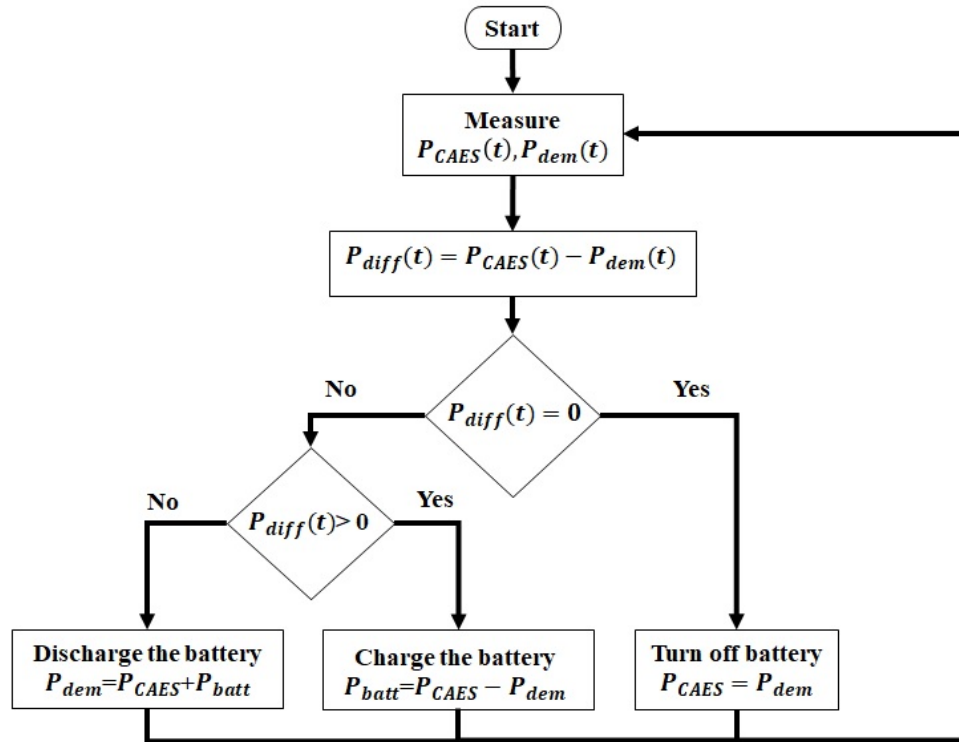
Figure 4.10 Power management flowchart

As mentioned previously, since the generated power from the SS-CAES system is assumed to be constant, there are both excess and deficit power during the period. A power management strategy is illustrated by the flow chart in Fig. 4.10. The SS-CAES system controlled by an MPPT controller is assumed as the main energy source of the hybrid system. The power difference between the SS-CAES system and load demand is calculated as:

$$P_{diff} = P_{CAES} - P_{dem} \tag{4.24}$$

where P_{CAES} is the power generated by the CAES and P_{dem} is the power demand.

The governing strategy is that, at any given time when the generated power P_{CAES} is greater than the demand power $P_{dem} (P_{diff} > 0)$, the battery will be charged by the amount of the excess power. Therefore, the power balance equation given in (4.2) can be rewritten as:

$$P_{batt} = P_{CAES} - P_{dem,} \qquad P_{diff} > 0 \tag{4.25}$$

where P_{batt} is the power stored by the battery.

In contrast, if the demand power P_{dem} is greater than the generated power P_{CAES} $(i.e., P_{diff} < 0)$, the battery begins to discharge power to the load in order to compensate the deficit. Hence, the power balance equation for this situation can be expressed as

$$P_{dem} = P_{CAES} + P_{batt,} \qquad\qquad P_{diff} < 0 \qquad\qquad (4.26)$$

4.3 Simulation results

4.3.1 Voltage controller tuning

Voltage controller for the battery

Bode diagram is used to specify the relevant gains of the controller. The gain and phase margins are chosen by reading the parameters in the Bode plot. To select the parameters of both loops, they must follow the criteria of the system's stability mentioned in Chapter 3 that the value of the phase margin must be between 30°- 60° and a gain margin must be greater than 3 dB [96].
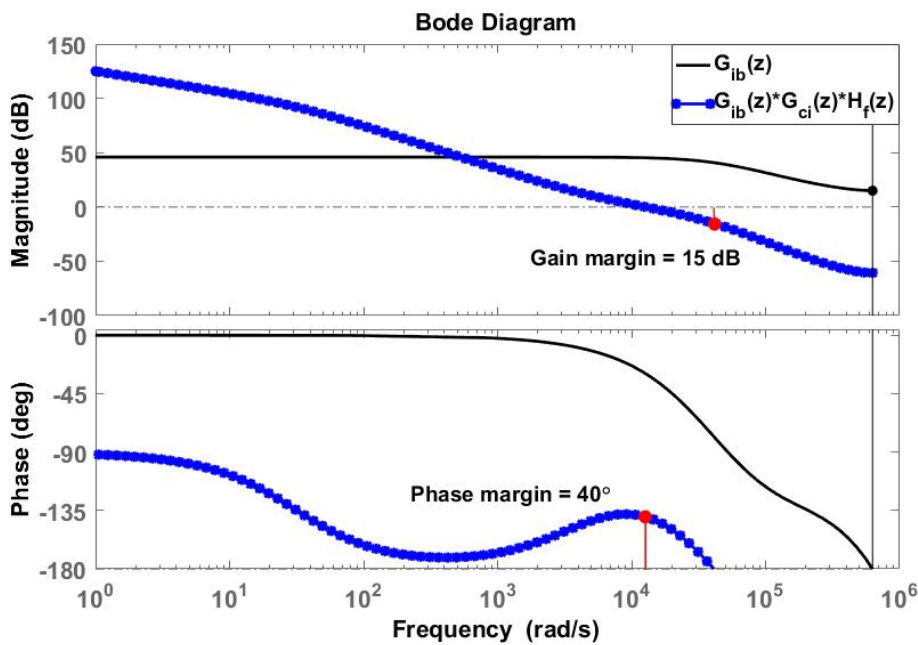
Figure 4.11 The Bode plot of the inner current loop

For the inner current loop, the transfer function (4.17) is cascaded with low pass filter (4.18), which is illustrated in Fig. 4.11 using Bode plots. It can be seen that a gain margin of more than 15 dB and a phase margin of 40° are selected for determining the parameters of $G_{ci}(z)$. The open-loop of the outer loop $G_{ib}(z)$ shown by the black line is compensated by the PI controller $G_{ci}(z)$ as represented by the blue line of the stable open-loop $G_{ci}(z)G_{ib}(z)H_f(z)$. Therefore, the required gain and phase margins are obtained for the compensated system.

For the outer voltage loop, the Bode plot of the open-loop transfer function of the input current reference and the output voltage is shown in Fig. 4.12. A phase margin of 60° and a gain margin of more than 5 dB are chosen on the Bode plot to specify the parameters of the $G_{cv}(z)$. It can be seen

that the outer voltage loop controller can achieve the required gain and phase margins. The uncompensated $G_{vp}(z)$ is reshaped by compensating the PI controller $G_{cv}(z)$, which is illustrated by the blue line representing the compensated $G_{cv}(z)G_{vp}(z)$.
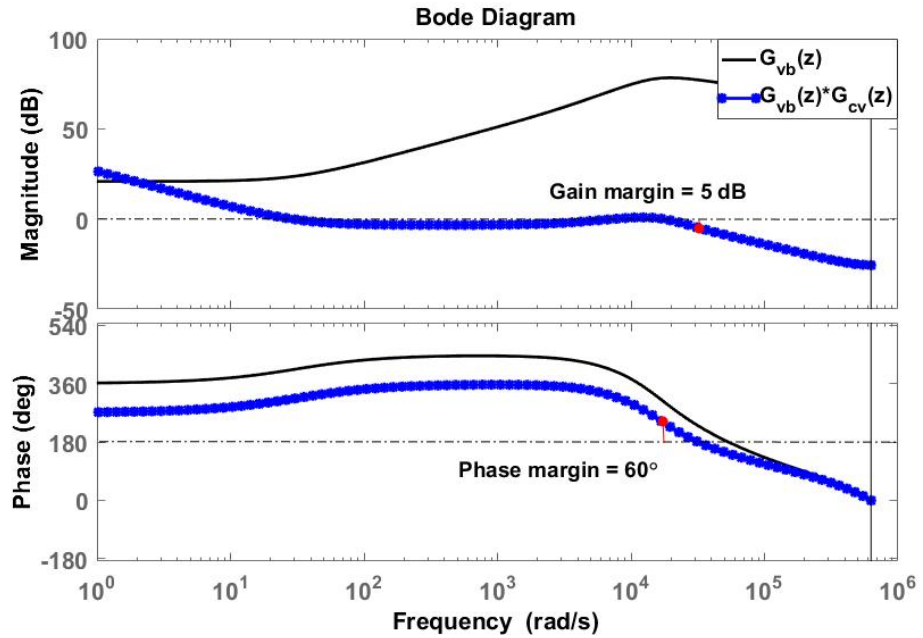
Figure 4.12 The Bode plot of the outer voltage loop

Voltage controller for SS-CAES

The parameters K_P and K_I have to be selected for both inner current and outer voltage loops in order to provide the stability of the system.
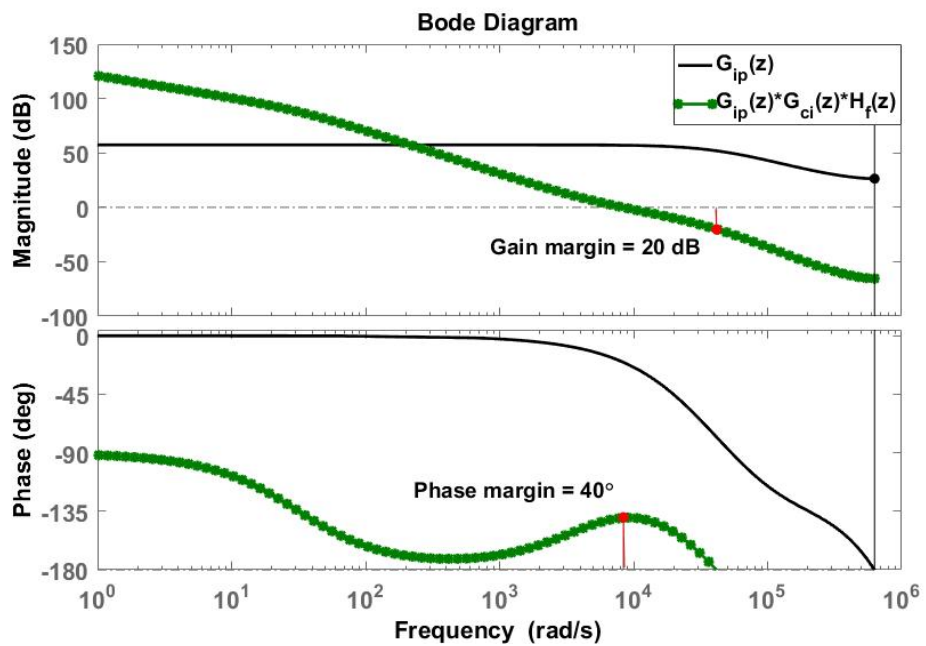
Figure 4.13 Bode diagram of the open-loop transfer function of G_{ip} (z) and G_{ip} (z) G_{ci} (z) H_f (z)

For the inner current loop, Eq. (4.20) is plotted on a Bode diagram with discrete transfer functions of the system as shown in Fig. 4.13. The system $G_{ip}(z)$ shown by the black line is stabilized by compensating the PI controller $G_{ci}(z)$, illustrated by the green line of the stable open-loop $G_{ip}(z)G_{ci}(z)H_f(z)$, to obtain the required values of the gain and phase margins. Based on the open-loop transfer function of $G_{ip}(z)$, the phase margin 40° and the gain margin more than 20 dB are selected on the Bode plot to determine the values of $G_{ci}(z)$.

To stabilize the outer voltage loop, Fig. 4.14 shows the Bode plot design of the outer voltage loop, which includes inner current loop $G_{vp}(z)$ shown by the black line. It is compensated by PI controller $G_{cv}(z)$ as represented by the green line of the stable open-loop $G_{vp}(z)G_{cv}(z)$. In this case, the designed values of the controller can be selected at the phase margin of 60° and gain margin greater than 15 dB.
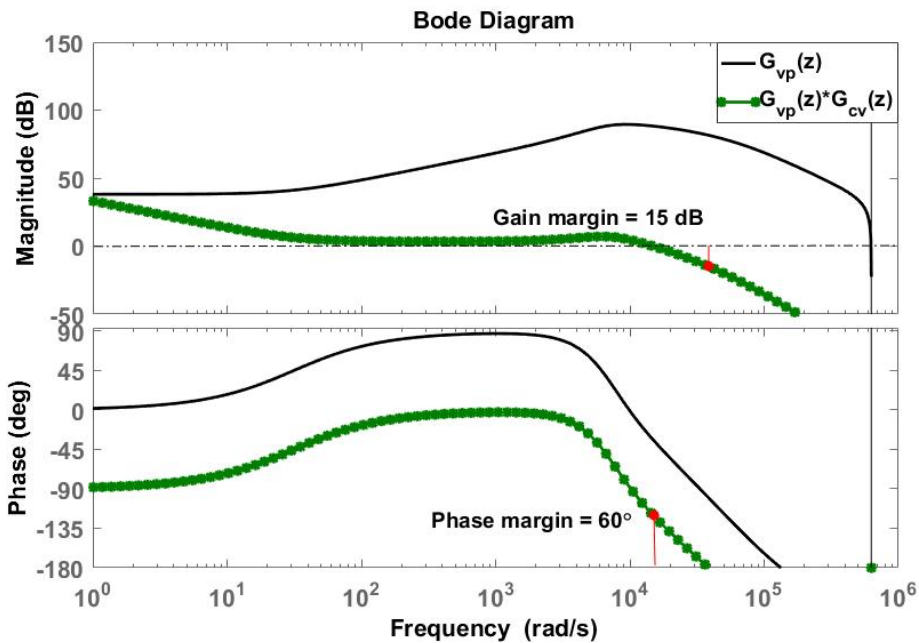
Figure 4.14 Bode plot design of the open-loop transfer function of G$_{vp}$ (z) and G$_{vp}$ (z) G$_{cv}$ (z)

4.3.2 Air motor and battery sizing

To select the air motor and battery sizes, the balance between charging and discharging energies need to be considered for the available battery in the subsequent cycle. The total charged energy should be greater than the discharging energy (E$_{Charged}$ ≥ E$_{Discharged}$). The air tank is assumed to have infinite supply of compressed air and discharge constantly at MPP under isothermal condition.
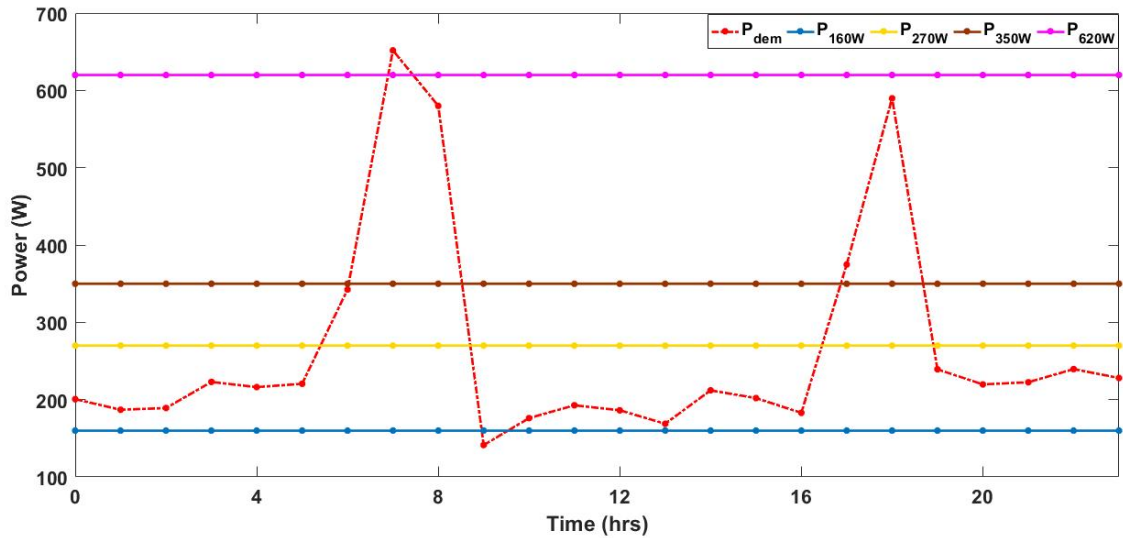
Figure 4.15 The demand power and SS-CAES power under different air motor power rating

Fig. 4.15 illustrates P_{dem} and P_{CAES} under different air motor power ratings. The effect of fluctuation of the power generation when the load change is neglected results in the constant P_{CAES}. Four different air motor power ratings of 160, 270, 350 and 620 watts, obtained from available commercial companies, are used [71]. P_{CAES} exceeds P_{dem} (red-dash line) considerably at the power rating of 620 W (purple) and the system needs a large battery for storing this extra power. In contrast, the 160 W air motor generates insufficient power, which cannot meet P_{dem}. This also results in the need of the massive battery for compensating the deficit power. At the power rating of 270 W (yellow), the generated power from the CAES exceeds P_{dem} except two periods of the peak demands, which are the time of 6 hrs to 9 hrs and 17 hrs to 19 hrs. The charging time is greater than the discharging time of approximately 14 hrs. The occurrence of charged energy is greater than that of the discharged energy that the battery will be ready for the next day. Hence, the air motor with the power rating of 270 W is selected. Since the CAES system cannot maintain the output voltage, the battery system needs to be estimated for supplying the power deficit. Under the power rate of 270 W, the calculated ED is illustrated in Fig. 4.16.
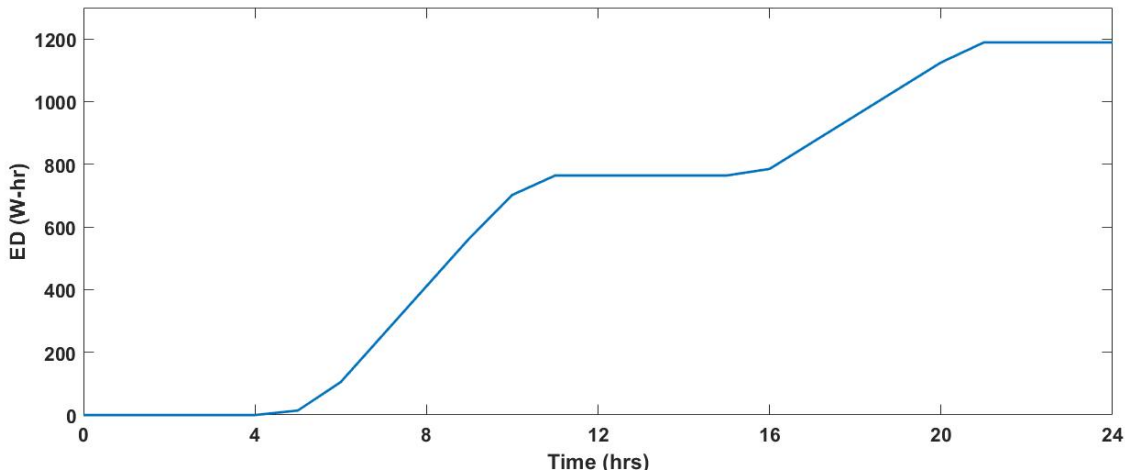
Figure 4.16 The deficit energy supply using an air motor with the power rating of 270 W

Clearly, the energy deficit (ED) is flat from the starting point to the time of 5 hrs since the generated SS-CAES energy is greater than the energy demand during this period. After that, the ED increases considerably from time of 4 hrs to around 11 hrs and increases again around 17 hrs. The charging time, moreover, is greater than the discharging time close to 14 hrs. The overall deficit reaches approximately 1189.3 W-hr within a 24 hrs period, which needs to be supplied by the battery. Including the self-discharge loss of 1% and the discharge efficiency of 80%, a 1500 W-hr battery is selected in this study. Note that the temperature effects are not considered here.

4.3.3 Performance of a hybrid SS-CAES system with a battery

The following results are obtained for an assumed pressure of 20 bar. Fig. 4.17 shows the ideal load power demand profile, which is used to investigate the hybrid performance. The output voltage in this simulation is 230 V. The speed responses of the CAES only system and hybrid system are shown in Fig. 4.18. The controller regulates the speed of the air motor effectively for real-time tracking that provides the speed reference to control the air motor speed reaching MPP. The red dash line is the reference speed generated by the MPPT algorithm while the actual speed of hybrid CAES with battery is the blue line and the speed of the CAES only system is represented by the green line. Obviously, the speed of response of the hybrid system seems to be slightly faster than one using the CAES only system since the battery supply power to the load during the SS-CAES runs to the MPP.
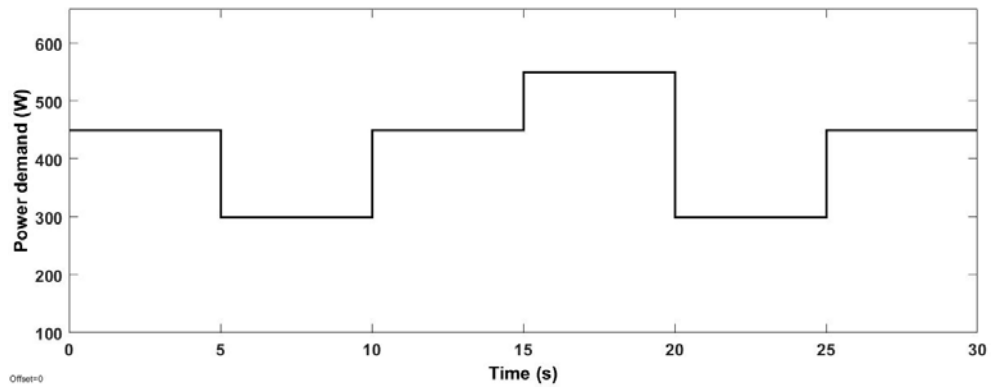
Figure 4.17 The ideal load power demand profile
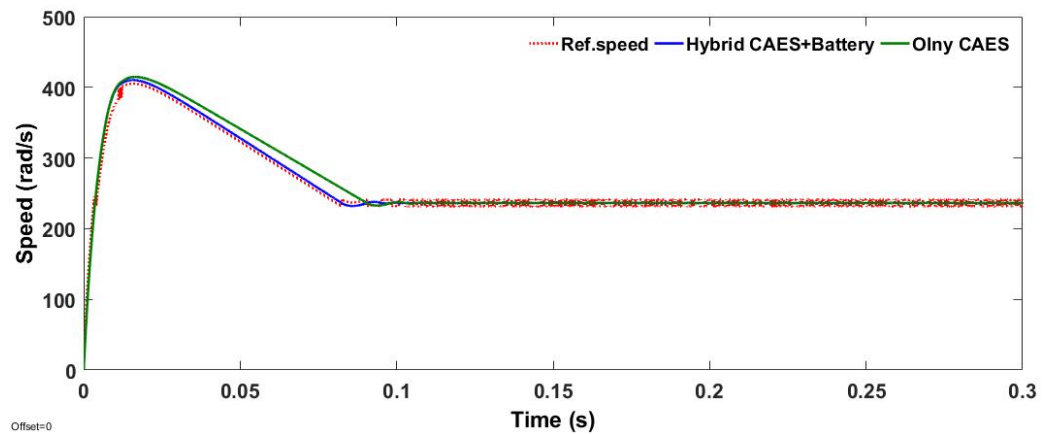
Figure 4.18 Results of MPPT controller

When the CAES system is controlled by the voltage controller, Fig. 4.19 illustrates the simulation results of the CAES system without a battery, which is controlled by the cascaded voltage controller. In Fig. 4.19(a), the output power of the CAES system can respond to the power demand but it has fluctuations when the demand changes. The output voltage in Fig. 4.19(b) has a long settling time before maintaining the reference voltage. Moreover, because of the voltage controller, the speed of the air motor will vary depending on the power demand; it does not operate at the maximum power point.
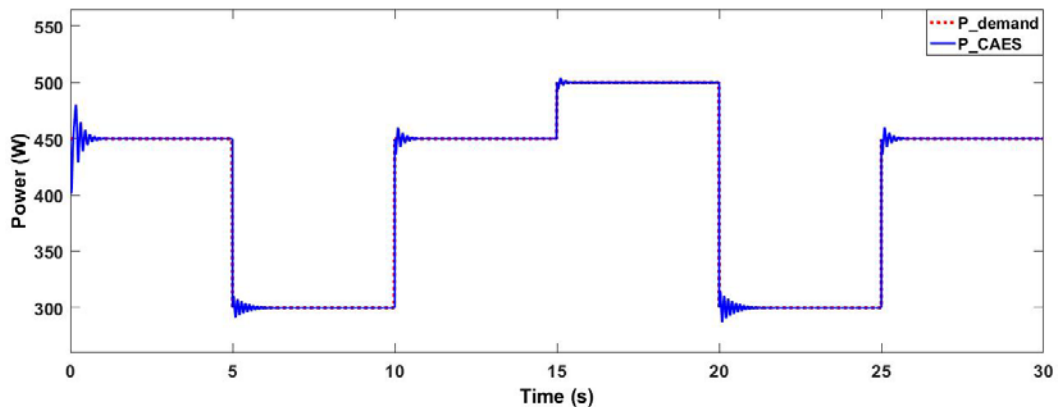
(a) The output power
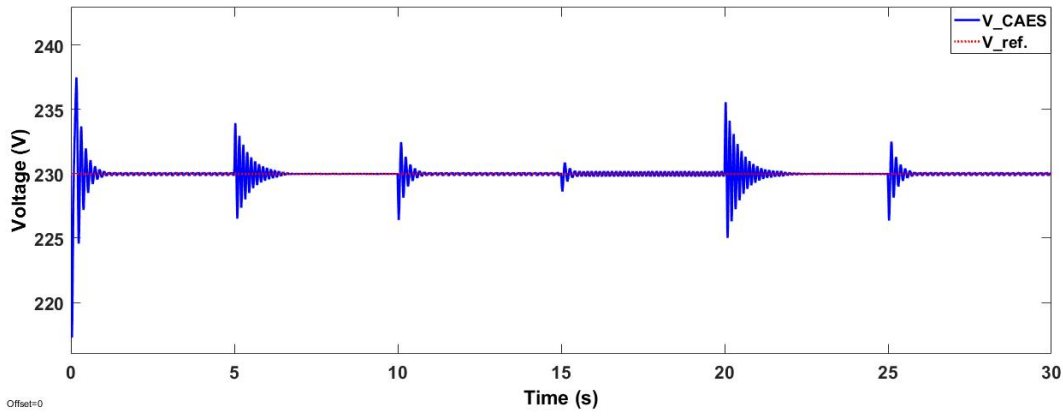
(b) The output voltage
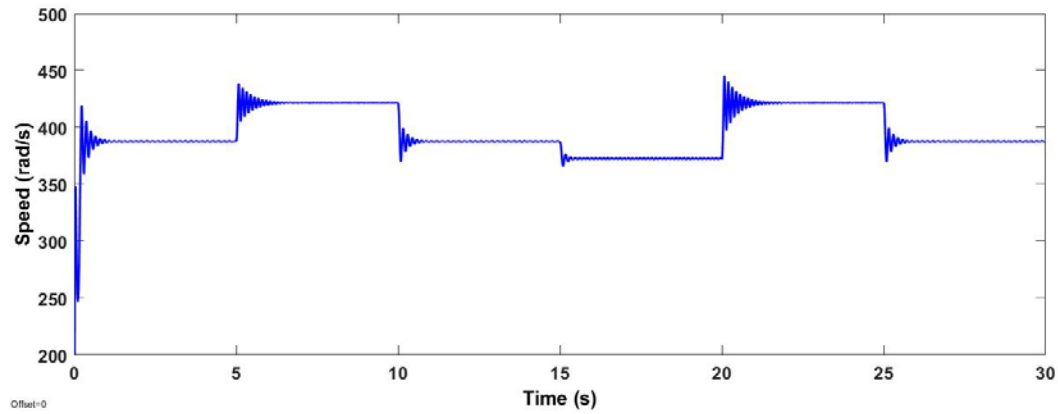
(c) The speed of the air motor

Figure 4.19 The simulation results of the CAES only system controlled by voltage controller

Unlike the hybrid battery and CAES system, Fig. 4.20 shows the simulation results of the hybrid system. In Fig. 4.20(a), the output power of the hybrid system is matched acceptably with the power demand. The battery-bidirectional converter is able to maintain the output voltage at 230 V throughout the simulation period presented in Fig. 4.20(b). Comparing between the outputs voltage in Fig. 4.19(b) and 4.20(b), the voltage of the hybrid system is set to the reference voltage faster than one of the CAES only system when the power demand changes; the hybrid system takes 0.6s to reach the reference voltage while the CAES in voltage mode spends 2.0s for settling. This because the battery compensates the power to maintain the voltage constant, which leads to the system's reliability. Additionally, the battery is charged (shown with negative current) when the CAES power is greater than the load power demand and discharged otherwise (shown with positive current).
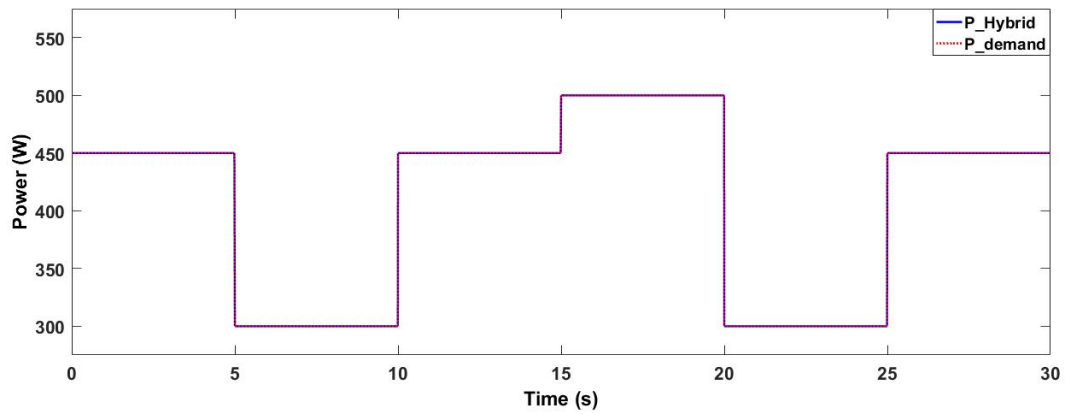
(a) The output power
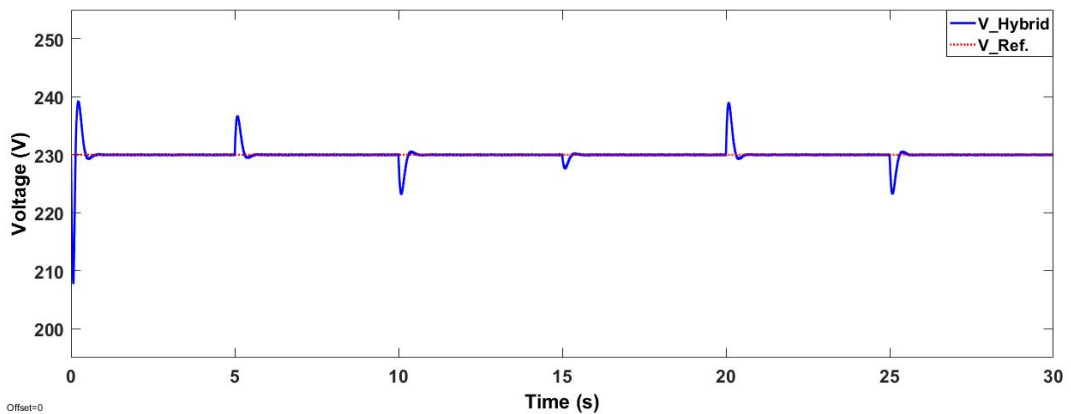
(b) The output voltage
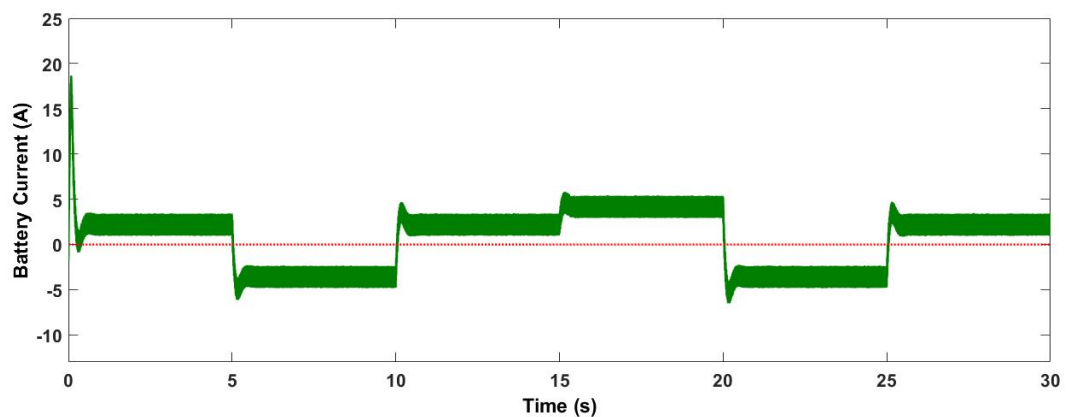
(c) The battery current

Figure 4.20 The simulation of the hybrid battery and CAES system

Considering the efficiency of the air motor controlled by a different controller, Fig. 4.21 shows the efficiency of the air motor controlled by the different controllers. The condition for efficiency testing is that the air motor operates at the constant pressure of 20 bar, which supplies power to a constant resistive load. The result shows clearly that the highest efficiency of the air motor on this graph is 6.59%. The air motor controlled by a voltage controller has low efficiency although the output voltage is constant. It provides the efficiency around 3.40%, which might result in power

losses in the air motor. On the other hand, the hybrid CAES-battery system can recover this situation since the CAES system controlled by MPPT controller operates at the MPP, which is close to the MEP, while the battery controlled by the voltage controller maintains the output voltage constant. Since the CAES system controlled by the MPPT controller, the efficiency is achieved approximately 6.43%, which differs from the MEP around 2.4%. This hybrid system can provide 47.1% of the air motor efficiency better than that of the air motor controlled in the voltage mode.
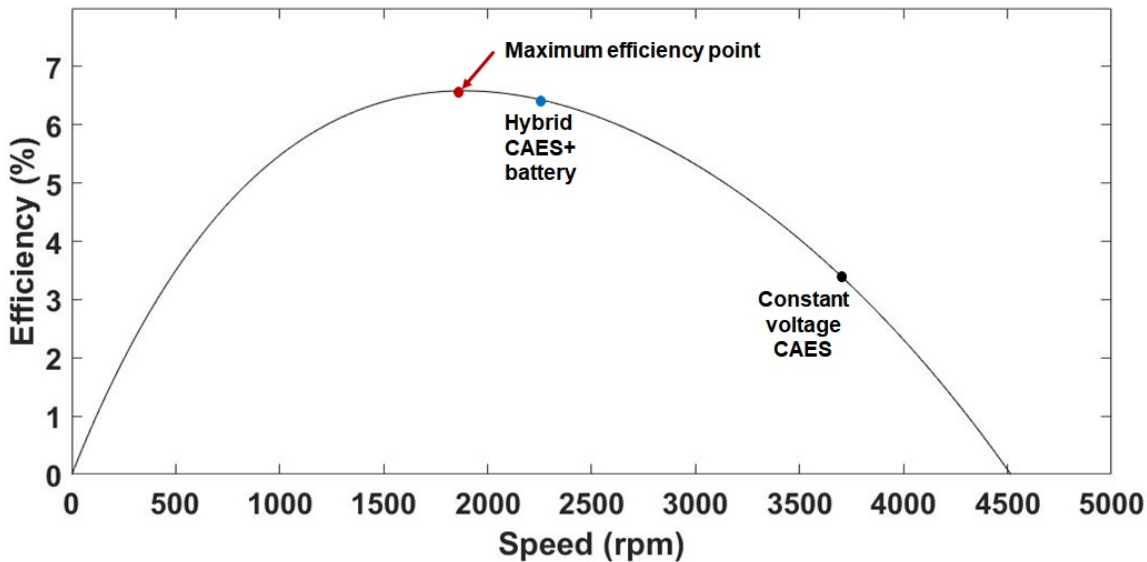
Figure 4.21 Efficiency comparison of the Air motor controlled by different controllers

4.4 Summary

This chapter has investigated the proposed hybrid energy storage system comprising SS-CAES system and a battery. The SS-CAES system is connected to the load through a boost converter that controls the air motor's speed to achieve maximum power point tracking (MPPT). A bidirectional converter is used to connect the battery to the load and maintain the constant output voltage.

The air motor and battery sizes are estimated properly for the load power profile in the Southern region of the UK. Four different power ratings of the air motor are chosen from commercial companies. For proper sizing, the air motor size is determined by considering the balance between charging and discharging times for the available battery in the next cycle. It is noted that the total charged energy should be greater than the discharging energy.

The energy deficit results from the difference between the generated power and demand power when the power demand is greater than the generated power. It is used to determine the battery size since the battery must cover such deficit. The estimated sizes for both energy storage systems guarantee sufficient energy storage for supplying the power within 24 hours.

Considering the performance of the hybrid system, two scenarios are studied. One of these scenarios is the SS-CAES only system controlled by cascaded voltage controller, which provides good performance to respond to the power demand and maintain the voltage constant. However, the air motor does not operate at the maximum power point since its speed depends on the demand change.

Another is a hybrid battery with SS-CAES system that are respectively controlled by the voltage and MPPT controllers. The hybrid system can maintain the voltage when operating at MPP, which improves the performance of the CAES system. With the load change, the performance of the CAES system is improved by including a battery to maintain voltage when the air motor operates at the MPP. The battery is charged during the low power demand and is discharged otherwise. However, as the CAES and the battery form the energy storage system, there is capacity limitations for both, which need to be recharged for the next use. The longer sustainability of power supply such as solar energy are considered to connect to these systems in order to store the excess energy when the solar energy is greater than the load demand.

Chapter 5 Photovoltaic system with SS-CAES in the charging process

This chapter focuses on the charging process of the SS-CAES system using solar energy. The model of the photovoltaic (PV) system is presented. It is controlled by the MPPT controller using perturb and observe method to reach the maximum power point. The PV system supplies power to selected load profile in the Southern area of the UK. Based on the solar irradiance, the SS-CAES is required to store the excess energy and use it to generate the power after sunset. To design proper size for this specific load profile, the component sizes of both PV and SS-CAES systems in charging state are estimated.

5.1 Topology of Photovoltaic systems

Fig. 5.1 shows the topology of the photovoltaic system, which consists of a PV module, boost converter and controller. The PV is connected with the load by means of a boost converter. To improve system's efficiency, the maximum power point tracking (MPPT) controller is used to ensure that the system always works to extract maximum available solar power. For implementing the MPPT, the DC boost converter is used to deliver power from PV panels to the load by adjusting the duty cycle to supply maximum power despite load fluctuations [85], [129]. The components of the PV system will be described and modelled in this section.
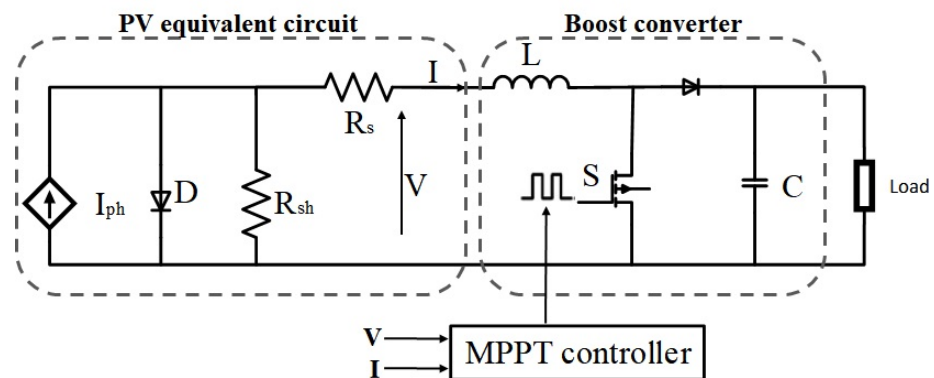
Figure 5.1 A typical Photovoltaic (PV) system

5.1.1 Photovoltaic model

A PV system, consisting of a number of PV modules that may be connected in parallel and series, produces electrical energy from the solar energy. The circuit diagram of a practical PV module is presented in Fig. 5.2.
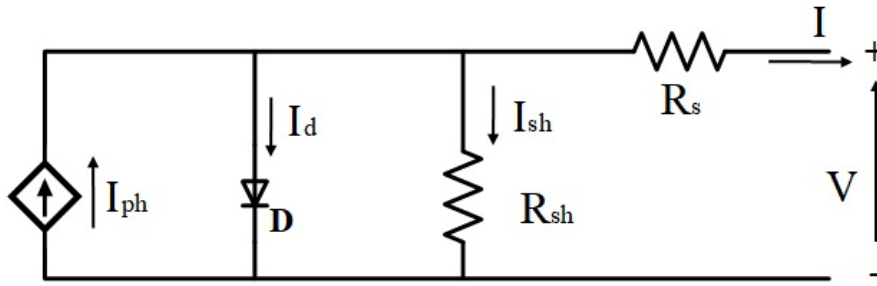
Figure 5.2 The circuit diagram of a PV module

The model consists of a current source connected in parallel with a diode and includes R_s in series and a parallel resistance R_{sh}. The equations, which describe the relationship between the output current and the voltage of the PV module, can be expressed as [130], [131]

$$I = I_{ph} - I_d - I_{sh} \qquad (5.1)$$

$$I = I_{ph} - I_s \left(exp \left(\frac{V+IR_s}{nV_T} \right) - 1 \right) - \left(\frac{V+IR_s}{R_{sh}} \right) \qquad (5.2)$$

where I_{ph} is the photovoltaic current, I_d is the junction diode current, I_{sh} is the shunt current, I_s is the saturation current of the diode, n is the ideality factor of the diode and $V_T = kT/q$ is the thermal voltage, k is a Boltzmann's constant, T is the temperature of the cell and q is an electron charge.

The photovoltaic current depends on the solar irradiance (G) and the temperature of the cell (T). It is described as [132], [133]

$$I_{ph} = \left(I_{sc} + K_I (T - T_{ref}) \right) \frac{G}{G_{ref}} \qquad (5.3)$$

where I_{sc} is the short-circuit current, K_I is the short-circuit current temperature coefficient, T_{ref} and G_{ref} are the reference temperature (25 °C) and reference solar irradiance (1000 W/m²), respectively. The saturation current mainly depends on the cell temperature. The relationship between the saturation current and the cell temperature can be described as

$$I_s = I_{RS} \left(\frac{T}{T_{ref}} \right)^3 exp \left(\frac{qE_g}{nk} \left(\frac{1}{T_{ref}} - \frac{1}{T} \right) \right) \qquad (5.4)$$

where E_g is the band gap for silicon and I_{RS} is the reverse saturation current, which is expressed as

$$I_{RS} = I_{sc} / (exp(qV_{oc}/nkT) - 1) \qquad (5.5)$$

where V_{oc} is the open-circuit voltage. These mathematical equations of the PV module are implemented in Matlab/Simulink for obtaining the current-voltage (I-V) characteristics.

5.1.2 Boost converter model

The DC-DC converter is employed for designing the MPPT controller since the PV module must operate at its maximum power. In this work, a boost converter is used to step up the voltage, which is generated by PV module because the output voltage (V_o) is higher than the PV voltage (V_i). The converter allows the PV system to operate at the maximum power point [134]. The circuit diagram of the boost converter model is illustrated in Fig. 5.3.
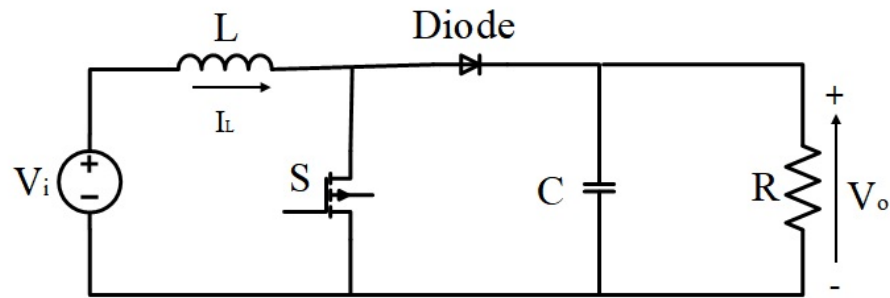
Figure 5.3 DC boost converter

5.2 MPPT controller

The MPPT controller is used to ensure that the system operates at the maximum power point. Various MPPT methods were proposed, which differ in complexity, sensor requirement, costs, and implementations [87], [135]. Among these methods, the perturb and observe (P&O) method is selected due to its simplicity, low computational power need and good performance at constant conditions. The P&O method is the most generally used MPPT algorithm. In a PV system, P&O involves the injection of a perturbation in the operating voltage of the PV array [83], [87]. In this method, the last perturbation and power increment result is used in the decision of estimating the next perturbation. Fig. 5.4 presents the P-V curve of a PV array.
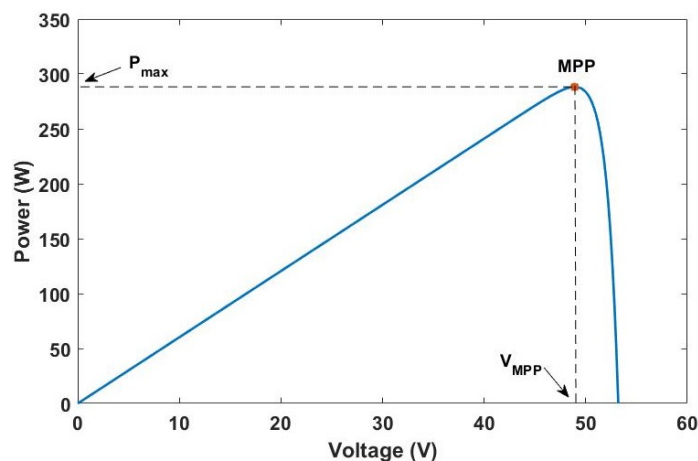
Figure 5.4 P-V characteristic curve [86]

Incrementing voltage will increase the power when the operating point is on the left hand side of the MPP while under voltage incrementation the power decreases when the operating point is on the right hand side [87], [90], [93]. This means that the next perturbation should be kept in the same direction if there is an increment in the power whereas if the power decreases, the perturbation should be reversed. The process is repeated until the MPP is achieved. The following flow chart demonstrates the working of the algorithm.
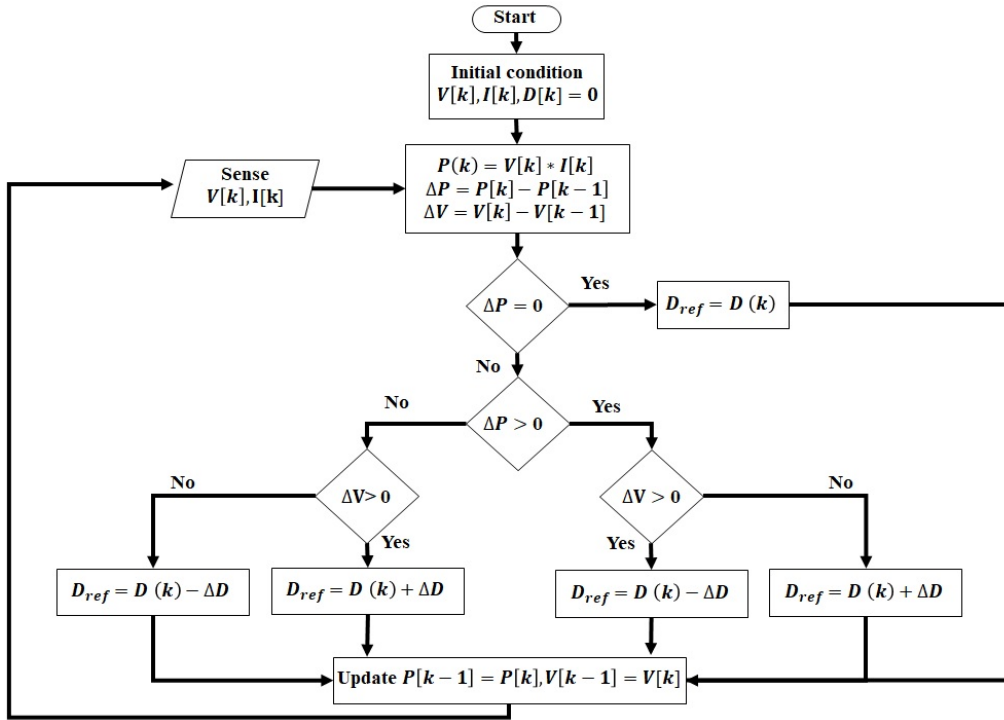
Figure 5.5 P&O MPPT flowchart

5.3 Component sizing

5.3.1 Components

Fig.5.6 shows the system configuration for the hybrid energy storage system including the PV panels, air generator and the air compressor. A Panasonic HIT Slim VBHN250SJ25 (250W) solar panel was selected for this study. The parameters of the PV panel are illustrated in the Appendix C. The PV power, connected to the load via the boost converter, are taken as the primary source. The SS-CAES system, which is also connected to the load through the boost converter, is used as a backup and storage system. Both systems has their control systems using maximum power point tracking (MPPT) strategy. The PV system starts to generate power supplying to the load from sunrise to sunset. A switch S_1 is switched on during this period. When the solar generation exceeds the demanded load power, the switch S_3 is on to turn on the compressor and begins compressing the air, which is delivered to the air tanks. When the power generation is not sufficient for the

power demand, the air generator will begin to produce power using the compressed air in the tank. In this case, the switch S_2 is on while the switch S_3 is off. For the component sizing, only the available excess power from the PV system is considered.
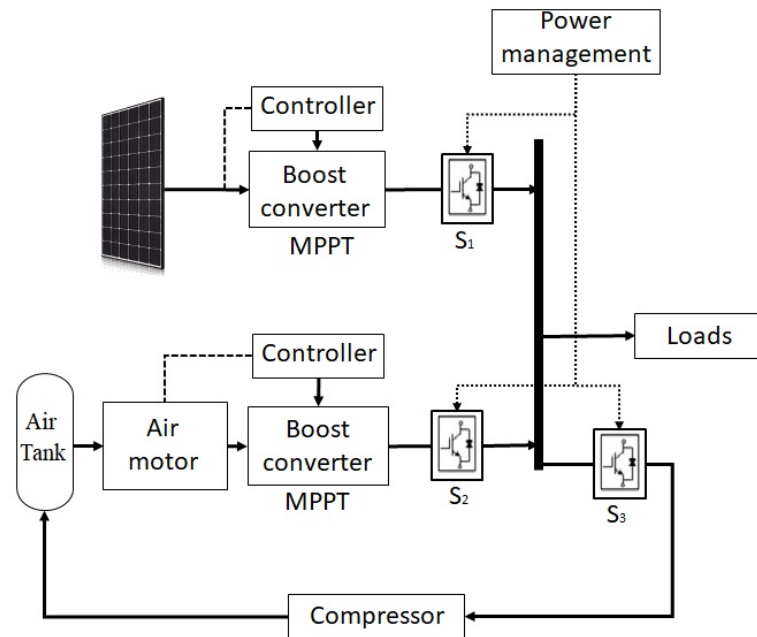
Figure 5.6 Configuration of the proposed PV system with the SS-CAES system

5.3.2 Resource and power demand data

Hourly solar irradiance data in winter, which was collected in the area of Southampton, UK are presented in Fig. 5.7 [136]. The maximum hourly load demand for a typical home in the County of Hampshire and the Isle of Wight was obtained from the Solent Achieving Value from Efficiency (SAVE) project conducted by Rushby et al [128] as presented in Fig.5.8. These data are used in the system component sizing study here. In each hour interval, the power generation and load demand power are assumed to be kept constant.
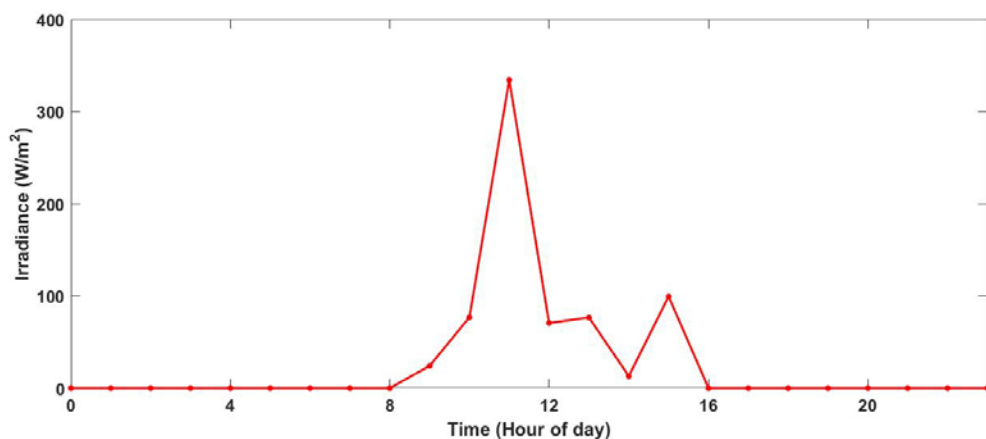
Figure 5.7 Hourly irradiance profile in winter[136]
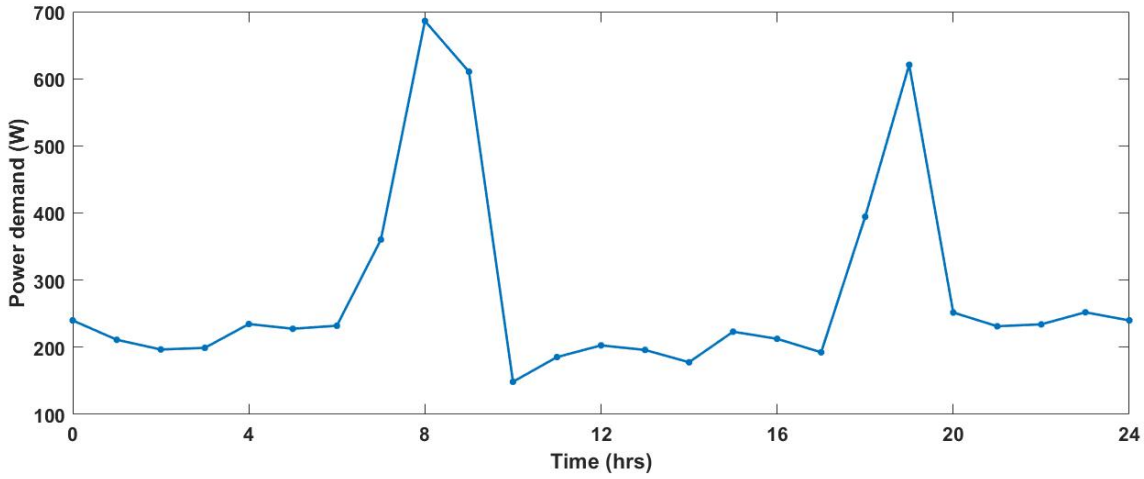
Figure 5.8 The maximum hourly load demand for a typical home [128]

5.3.3 Component sizing technique

The total PV generated power during each hour is first calculated by

$$P_{gen}(t) = N_{pv} \cdot P_{pv}(t) \tag{5.9}$$

Where N_{pv} is the number of PV panel and $P_{pv}(t)$ is the power of the PV at time t. The $P_{pv}(t)$ is calculated by converting the irradiance data, which can be expressed as

$$P_{pv}(t) = \eta_{pv} \cdot A \cdot G(t) \tag{5.10}$$

Where A is the area of a single PV panel, $G(t)$ is the irradiance data at time t , η_{pv} is the efficiency of the PV module [137]. In this study, the PV system is assumed to operate at the MPP and the temperature effects on the PV panel are neglected. Because of the constant power in particular time, the generated and demand energy at time t can be calculated by

$$E_{gen} = \left[\frac{P_{gen}(t) + P_{gen}(t-1)}{2}\right] \cdot \Delta t \tag{5.11}$$

$$E_{dem} = \left[\frac{P_{dem}(t) + P_{dem}(t-1)}{2}\right] \cdot \Delta t \tag{5.12}$$

To determine the number of PV panels and SS-CAES size, the balance between the generated and demand energies need to be considered for the available SS-CAES in the next cycle and the total generated energy from PV panel should be greater than the demand energy ($E_{gen} \geq E_{dem}$). The energy difference (EDF) at time t between the PV and the demand power is used, which can be calculated by

$$EDF(t) = (E_{gen}(t) \cdot \eta_{pvs}) - (E_{dem}(t)/\eta_{co}) \tag{5.13}$$

where η_{pvs} is the average efficiency of the PV power output and η_{co} is the converter's efficiency. The $EDF(t)$ will be positive called the excess energy $\left(E_{ex}(t)\right)$ if the power generated from PV system is greater than the load demand in each hour $\left(P_{pv}(t) > P_{dem}(t)\right)$. Also, it will be negative called the deficit energy $\left(E_{dif}(t)\right)$ if the load demand is higher than power generated from PV system in each hour $\left(P_{dem}(t) > P_{pv}(t)\right)$. The total energy can be expressed as

$$E_{ex} = \sum_{t1}^{t2} EDF(t) \tag{5.14}$$

$$E_{def} = \sum_{t3}^{t4} EDF(t) \tag{5.15}$$

where $t1, t2$ are the start and final times when $P_{pv}(t) > P_{dem}(t)$ and $t3, t4$ are the start and final times when $P_{dem}(t) > P_{pv}(t)$.

When the generated power is higher than the demand power, the excess energy needs to be stored as a compressed air. The compressor will be used to fill the air tank based on the thermodynamic law of the energy conversion of air. The compression process is assumed under isothermal condition. The amount of air stored in the tank, which equals to the excess energy, can be written as

$$m = (E_{ex} \cdot \eta_c \cdot 3600)/\left(R_g T \ln\left(\frac{P_{tank}}{P_a}\right)\right) \tag{5.16}$$

where η_c is the compressor efficiency, E_{ex} is the excess energy stored in the tank, R_g is the specific gas constant, T is the temperature assumed constant, P_{tank} is the tank pressure of 20 bar used in this thesis and P_a is the ambient pressure. Therefore, the size of the tank is estimated using the ideal gas law expressed below [20]:

$$V_t = (mR_g T)/P_{tank} \tag{5.17}$$

where V_t is the volume of the tank. Within the period for storing the excess energy, the power rating of the compressor needs to be specified, which is expressed as:

$$P_{com} = (E_{ex} \cdot \eta_c)/t \tag{5.18}$$

where t is the charging period.

5.4 Simulation results

5.4.1 PV module characteristics

The mathematical models of the PV characteristics are designed and implemented by using Matlab/Simulink. The characteristics of the solar panel Panasonic HIT N250 with a power rating of 250 W [138] are selected in this thesis at various irradiance levels and temperature of 25°. The I-V and P-V characteristics of the PV using Eq. (5.2)-(5.5) are shown in Fig 5.9.

(a) I-V curve   (b) P-V curve
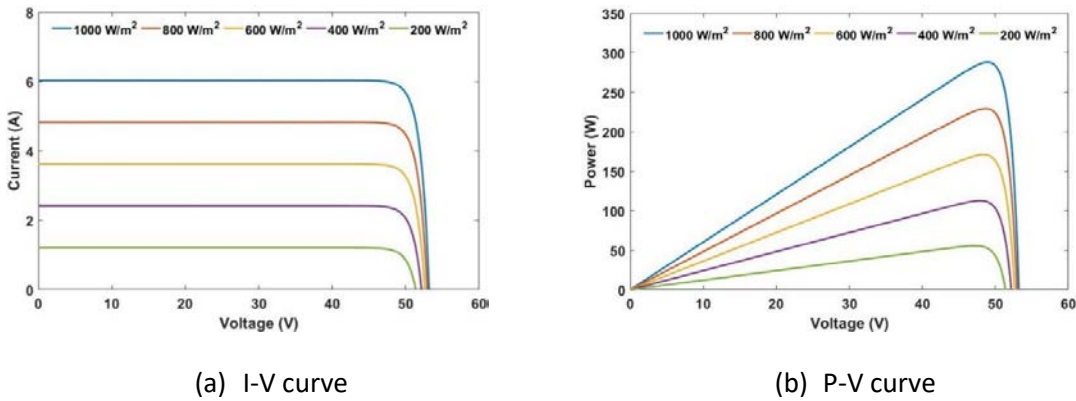
Figure 5.9 The characteristics of PV panel under irradiance variations

It can be noted that the PV current relates to the irradiance levels directly; the current increases when the irradiance level rises up. Therefore, the maximum power also increases since it is proportional to the PV current [135]. However, when the irradiance level is assumed to be constant at 1000 W/m^2, the temperature has an inverse proportion to the open-circuit voltage. It means that the voltage will drop if the temperature increases as illustrated in Fig. 5.10(a). Hence, the maximum power also decreases because of the temperature increase shown in Fig. 5.10(b).

(a) I-V curve   (b) P-V curve
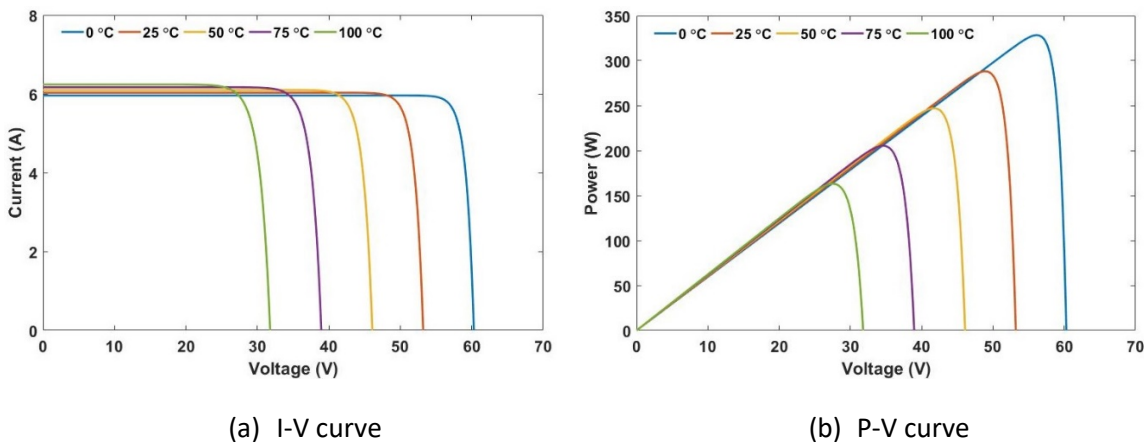
Figure 5.10 The characteristics of PV panel under temperature variations

The mathematical models provide the current-voltage curve similar to the data from the manufacturer. It can be confirmed that the equations of the PV panel are correct, which can be used in this study.

5.4.2 The PV system with MPPT controller

The model of the PV system is implemented using the SimPowerSystem in Matlab/Simulink. The system includes the PV panel model, the boost converter and the MPPT controller. The values of the converter and PV components are presented in Appendix C. The PV system is simulated in both constant and variable irradiances. Fig. 5.11 shows the simulation results of the PV system using the MPPT controller under a constant irradiance of 1000 W/m^2. Clearly, the controller has effectively controlled the PV operation at the MPP.
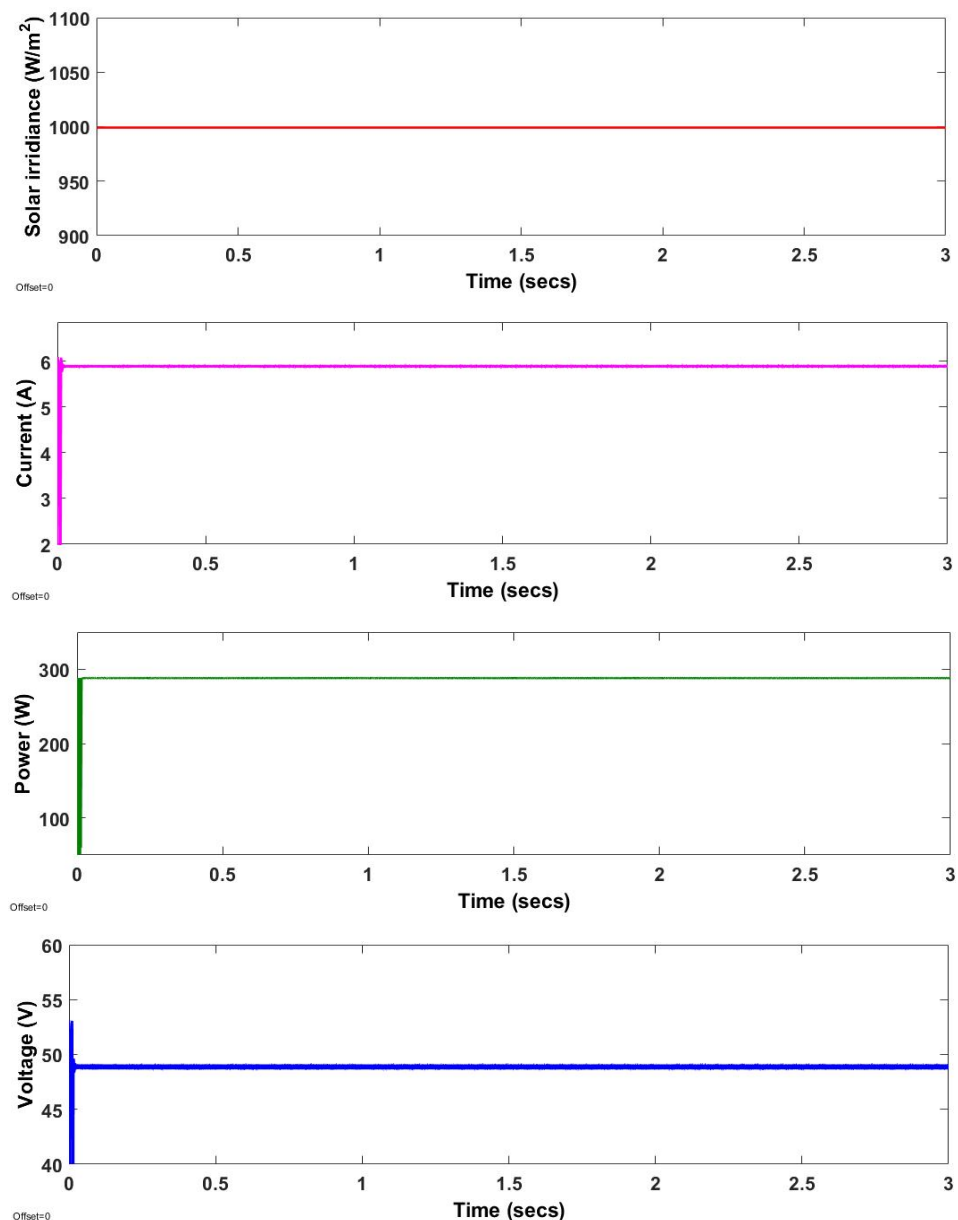
Figure 5.11 Simulation results of the PV system under constant irradiance of 1000 W/m^2

Fig. 5.12 illustrates the current, voltage and power of the PV system under various solar irradiances. When the step solar irradiance changes from 800 to 400 to 1000 to 800 and then to 600 W/m^2, the MPPT controller has successfully controlled the PV system to generate the maximum power at each irradiance level (green). It can be seen that the MPPT controller has successfully controlled under varying irradiance conditions.
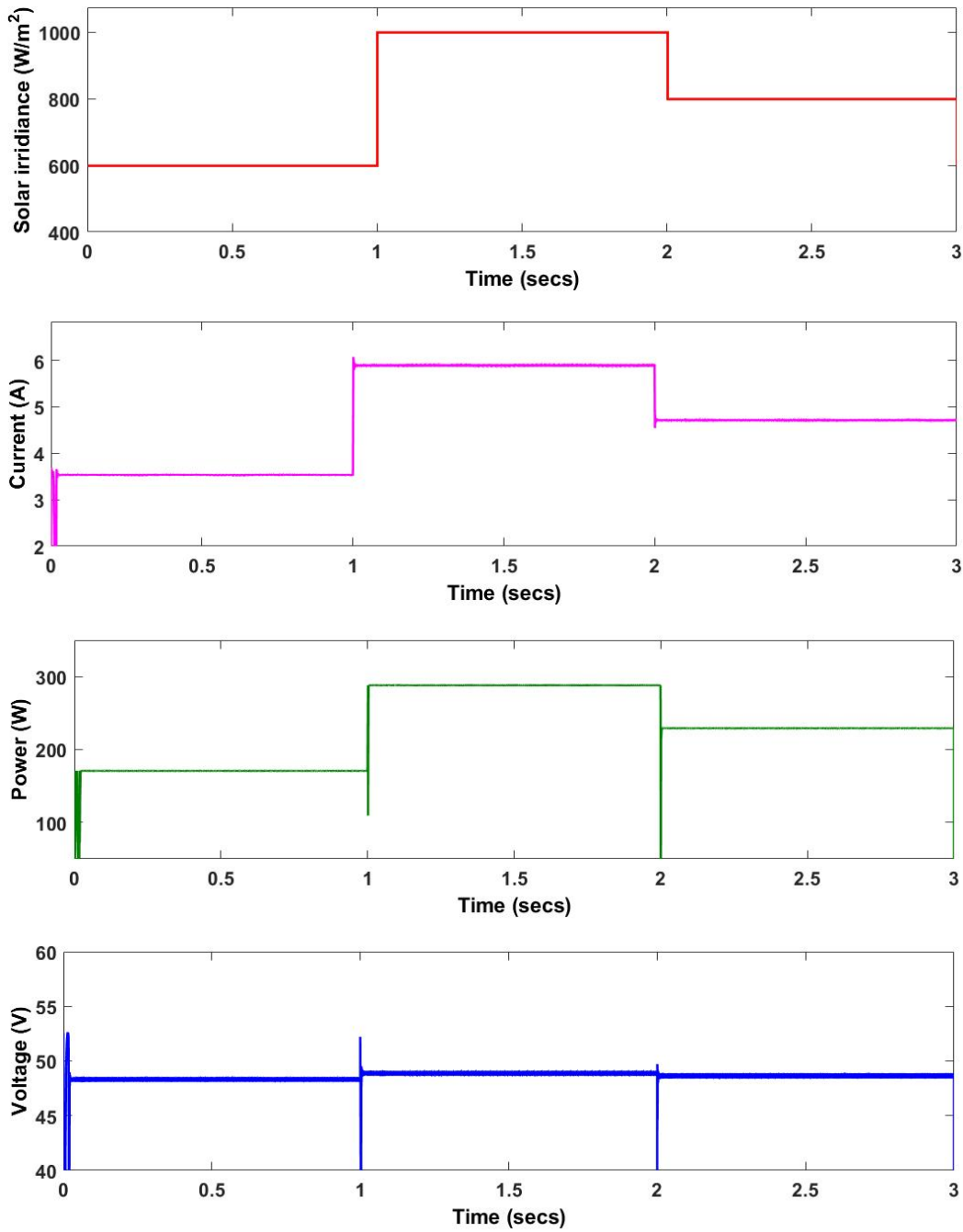
Figure 5.12 Simulation results of the PV system under varying irradiance condition

5.4.3 Component sizing

The household load profile in Section 4.3 is to be matched with the generated powers from different numbers of PV panels. The power generated by PV system in each hour was calculated by using Eq. (5.9) and (5.10). To determine the number of PV panels, five different numbers of PV panels with a power rating of 250 W each are examined. Fig. 5.13 shows the demand power (P_{dem}) and the generated powers (P_{pv}) by different number of PV panels. It can be seen that all generated powers from PV system are lower than the demand from the beginning up to around the 9 hour and from 17 hours to 24 hours. In contrast, the PV power is greater than the demand between 7 to 16 hours.
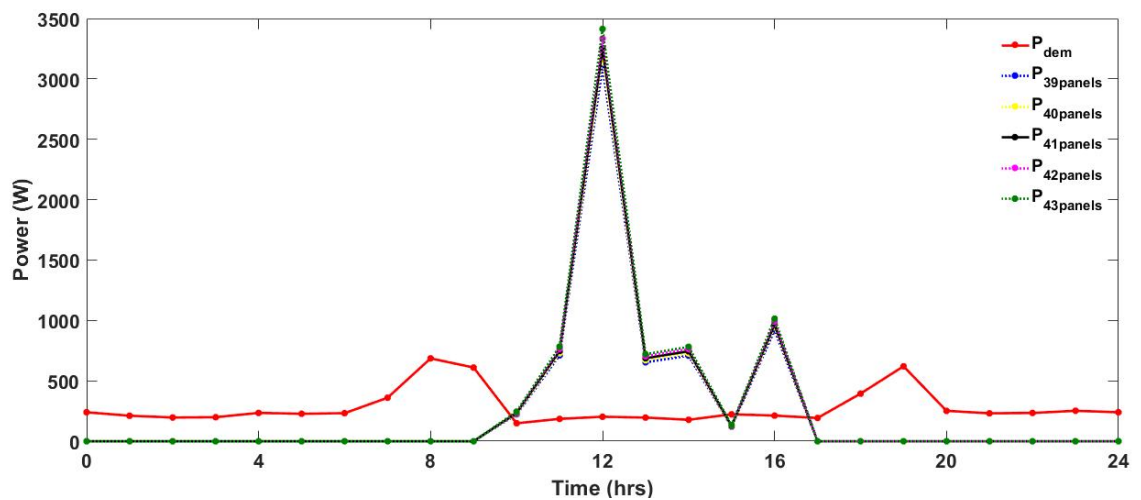
Figure 5.13 The demand and generated powers from different number of PV panels during a day

The calculation of hourly demand energy and generated energy from different number of PV panels throughout a day using Eq. (5.11) and Eq. (5.12) are illustrated in Table 3. The first two columns shows the duration in hour and the calculated demand energy, respectively. In the third, fifth, seven, ninth and eleventh columns, the generated power from the 39, 40, 41, 42 and 43 PV panels are calculated. The energy difference (EDF) between the five different numbers of PV system and demand during each hour using Eq. (5.13) are shown in the fourth, sixth, eighth, tenth and twelfth columns, respectively. As can be seen clearly the EDF can have positive and negative values. The positive values indicate the excess in energy while negative values represent energy deficit. To determine the number of PV panel for the selected load demand and providing the sufficient excess energy for storing in order to compensate the deficit energy, the total energy deficit and excess energy are considered.

Hours of a day	E_dem (Whr)	E_gen (Whr)									
		39 panels	EDF	40 panels	EDF	41 panels	EDF	42 panels	EDF	43 panels	EDF
1	100.4	0	-100.4	0	-100.4	0	-100.4	0	-100.4	0	-100.4
2	204.1	0	-204.1	0	-204.1	0	-204.1	0	-204.1	0	-204.1
3	198.0	0	-198.0	0	-198.0	0	-198.0	0	-198.0	0	-198.0
4	216.9	0	-216.9	0	-216.9	0	-216.9	0	-216.9	0	-216.9
5	231.2	0	-231.2	0	-231.2	0	-231.2	0	-231.2	0	-231.2
6	229.9	0	-229.9	0	-229.9	0	-229.9	0	-229.9	0	-229.9
7	296.4	0	-296.4	0	-296.4	0	-296.4	0	-296.4	0	-296.4
8	523.4	0	-523.4	0	-523.4	0	-523.4	0	-523.4	0	-523.4
9	648.4	0	-648.4	0	-648.4	0	-648.4	0	-648.4	0	-648.4
10	379.7	111.3	-268.3	114.2	-265.5	117.0	-262.6	119.9	-259.8	122.8	-256.9
11	167.1	466.8	299.7	478.8	311.6	490.7	323.6	502.7	335.6	514.7	347.6
12	194.2	1903.6	1709.4	1952.4	1758.2	2001.2	1807.0	2050.0	1855.8	2098.8	1904.6
13	199.5	1875.0	1675.5	1923.1	1723.6	1971.2	1771.6	2019.2	1819.7	2067.3	1867.8
14	186.9	681.5	494.5	699.0	512.0	716.4	529.5	733.9	547.0	751.4	564.4
15	200.5	414.9	214.3	425.5	225.0	436.1	235.6	446.8	246.3	457.4	256.9
16	218.0	520.3	302.3	533.7	315.7	547.0	329.0	560.3	342.3	573.7	355.7
17	202.7	460.1	257.4	471.9	269.2	483.7	281.0	495.5	292.8	507.3	304.6
18	293.6	0	-293.6	0	-293.6	0	-293.6	0	-293.6	0	-293.6
19	507.8	0	-507.8	0	-507.8	0	-507.8	0	-507.8	0	-507.8
20	436.4	0	-436.4	0	-436.4	0	-436.4	0	-436.4	0	-436.4
21	241.6	0	-241.6	0	-241.6	0	-241.6	0	-241.6	0	-241.6
22	232.8	0	-232.8	0	-232.8	0	-232.8	0	-232.8	0	-232.8
23	243.3	0	-243.3	0	-243.3	0	-243.3	0	-243.3	0	-243.3
24	246.2	0	-246.2	0	-246.2	0	-246.2	0	-246.2	0	-246.2

Table 3 Calculation of the energy difference

The total deficit and excess energies of different number of PV panels using Eq. (5.14) and (5.15) are illustrated in Table 4. Clearly, the excess energy is lower than the deficit energy when 40 PV panels or lower panel numbers are employed. This results in insufficient power supply. However, the overall excess energy is greater than the energy deficit when at least 41 PV panels are used. The excess energy increases when increasing the PV panel numbers, which require a large capacity size of the compressed air tank for storing this extra energy. At 41 PV panels, the occurrence of the excess energy is greater than the deficit energy, and the SS-CAES will be ready for the next day. 41 PV panels, therefore, are selected in this thesis.

PV panel No.	Total excess energy (Whr)	Total deficit energy (Whr)	Difference of total energy (Whr)
39	4953.1	-5118.8	-165.6
40	5115.2	-5115.9	-0.7
41	5277.3	-5113.0	164.3
42	5439.4	-5110.2	329.2
43	5601.5	-5107.3	494.2

Table 4 Total excess and deficit energies of different numbers of PV panels

The overall excess energy of 41 PV panels is 5277.3 Whr within a 24 hour period, which needs to be stored as high pressure air in a pressure tank by applying electrical energy to the compressor. The energy can be stored from time of 11 to around 17 hours. Although the charging time is lower than the discharging time, the total charging energy is greater than the discharging energy. This means that there is sufficient energy to compensate for the deficit energy.

The tank size storing this amount of energy can be estimated by using Eq. (5.16) and (5.17). Considering the relationship between pressure and volume, Fig. 5.14 shows the tank size at different pressure levels. It is clearly that the tank size is significant large for storing this excess energy in low pressure. It can be reduced by increasing the pressure, which might be desirable. But beyond about 20 bar, it seems diminishing returns. Therefore, the pressure of 20 bar is selected in this thesis.
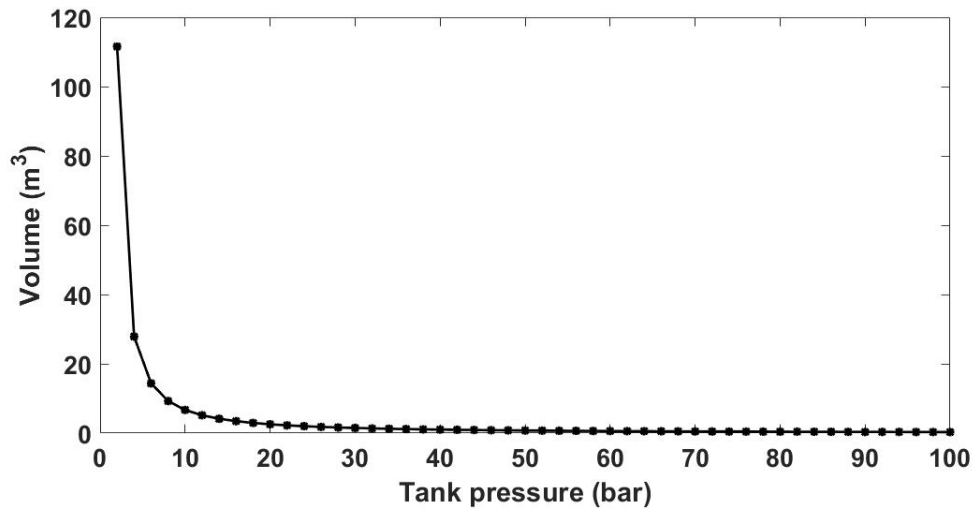
Figure 5.14 The tank volume vs pressure

The total amount of air stored in the tank at the pressure of 20 bar is around 64.9 kg. Hence, the required air tank volume is 2.8 m³, which is calculated by using Eq. (5.17). Moreover, since the compressor is assumed to store the overall excess energy within charging period (7 hours), the power rating of the compressor should be 720 W, calculated by using Eq. (5.18).

5.5 Summary

In this chapter, a PV system is used to supply power to a variable load and charge the SS-CAES system when the PV generated power is greater than the load demand. Non-ideal photovoltaic model with series and parallel resistances is designed to obtain the PV current and voltage as well as the PV characteristics. The simulation results show that the PV current and power are strongly depended on the solar irradiances, i.e., they increase when the irradiance rises up. However, the temperature has an effect to the PV performance. In the other word, the voltage is dropped when the temperature increases leading to the decrease of power.

The MPPT controller is designed to control the PV system operating at the maximum power point. The perturb and observe method is employed by using the P-V characteristics of the PV module. The results show that the controller performs well to control the PV system operating at the MPP under constant irradiance. When the solar irradiance varies, it can effectively control the PV system at each solar irradiance level.

As the PV system operates only during the daytime, the SS-CAES is required to store the excess energy and discharge it during the night-time. All component sizes are calculated to ensure that the hybrid system can supply the sufficient power to the chosen household load profile in the Southern region in the UK. A sizing method, using the difference between the generated and demand powers,

is proposed to calculate the excess energy. The results illustrate that 41 PV panels can supply enough power to the load and provide sufficient excess energy to be stored in the air tank. The air tank size of 2.8 m^2 is employed for storing the overall excess energy based on the thermodynamic law of energy conversion of air and the ideal gas law. Since the compressor is used to convert all excess energy within 11 hours, its power rating is estimated to be equal to 720 W. The next chapter will consider the sizing of the combination of a PV system with a hybrid energy storage system comprising SS-CAES and a battery.

Chapter 6   PV system with a hybrid ESS comprising SS-CAES system and a battery

This chapter presents the component sizing of the discharging process of a PV system combined with a hybrid energy storage system (ESS) comprising the SS-CAES system and a battery. The PV and SS-CAES systems are assumed to operate at their MPP and the temperature effect during discharging process has been neglected. The topology of the hybrid system was proposed to illustrate the overview of the system. Then, a simple sizing method including the system's efficiency is presented for estimating the average power rate of the air motor. It is also used to determining the proper capacity for the battery.

6.1 Topology of the hybrid system
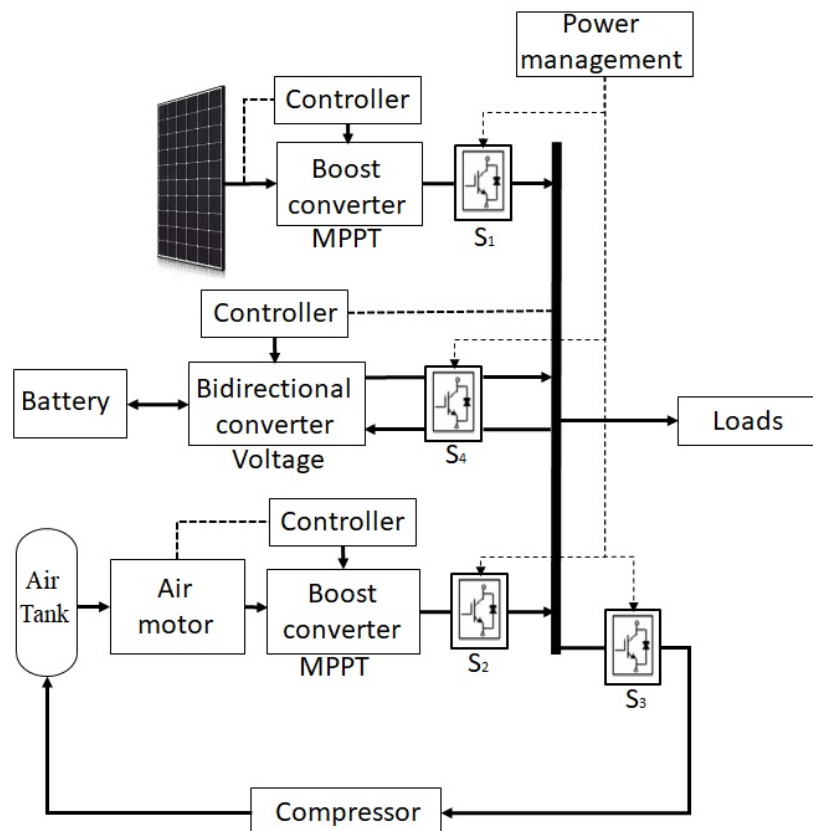
Figure 6.1 Hybrid system structure

Fig. 6.1 illustrates the proposed topology of the hybrid system, which consists of solar panel, battery and SS-CAES system. Each component is connected to the load via the DC-DC converter and has its individual control system. The PV system acts as the primary energy source of the hybrid system connected to the DC bus through a boost converter, which is controlled by a maximum power point

tracking (MPPT) controller. The SS-CAES system as a backup and high-energy storage system is used to supply power when the PV power is insufficient for the load during night-time. It is connected to the load via a boost converter, which is controlled by the MPPT control system. The battery is connected to the load through a bidirectional converter, which supplies power when the generated power from PV and SS-CAES systems is lower than the power demand during the night and hence it stores the excess energy from the SS-CAES. The voltage controller is employed to maintain the output voltage; the current follows the reference values corresponding to the charge and discharge currents.

The power management unit is added to manage the operation of each system by controlling four switches. The switch S_1 is switched on for PV operation during daytime and is switched off during night-time. S_2 is switched on and S_3 is switched off when the load demand power is greater than the PV power. The operations of these two switches are suddenly changed if the PV power is greater than the load demand. S_4 is switched on if the generated power from PV and the stored power in the SS-CAES systems are insufficient for supporting the load and it is switched off otherwise.

6.2 Component sizing

6.2.1 Resource and power demand data

The data for a household load demand and solar irradiance in winter are already illustrated in Sections 4.3 and 5.3, respectively. An hourly household load demand for a typical home in the County of Hampshire and the Isle of Wight was illustrated by Rushby *et al* [128]. Hourly solar irradiance data in winter was collected in the area of Southampton, UK [136]. In this Chapter, these data are used for estimating the sizes of the air motor and the battery and are assumed constant within each hour.

6.2.2 Sizing technique

6.2.2.1 Power rating of the air motor

To determine the power rating of the air motor, the energy difference between the PV power and the demand power is considered. The solar system consists of 41 Panasonic HIT N250 panels with a power rating of 250 W each. The solar irradiance data is converted to PV power using Eq. (5.9) and (5.10). The demand power (P_{dem}) and photovoltaic power (P_{pv}) are shown in Fig. 6.2.
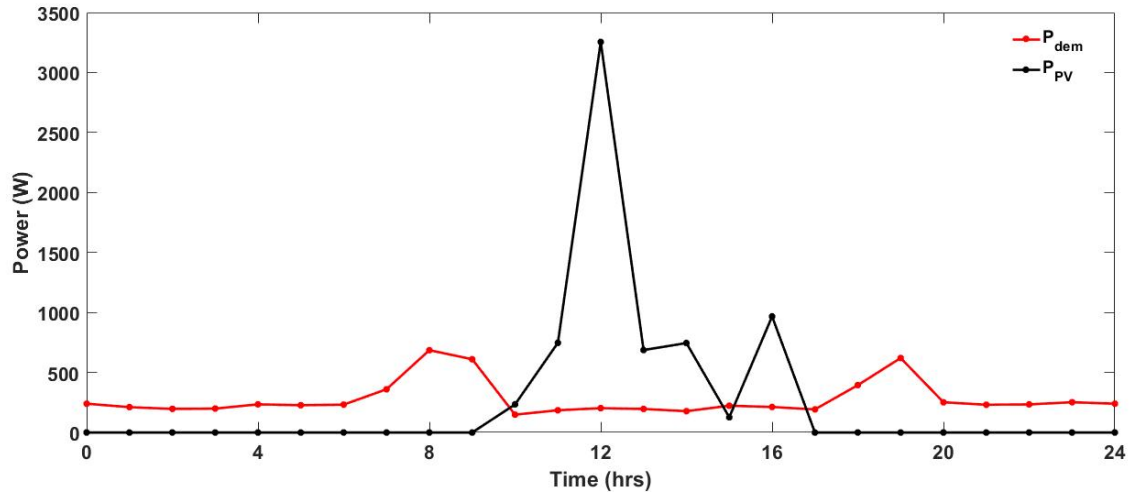
Figure 6.2 Hourly PV-demand powers during a day

Obviously, the PV power strongly depends on the solar irradiance, which can operate during the daytime (between 9 to 17 hrs). The PV power is greater than the load demand from time of 10 hr to 16 hr, which is approximately 7 hours in total. The total amount of energy is used to estimate the sizes of the storage tank and the compressor. However, it is lower than demand between the beginning to the time of 9 hr and from the time of 17 hr to 24 hr. This issue results in using the SS-CAES system for compensating the insufficient power. The power rating of the air motor is estimated from the total deficit energy between the PV and load power demand. Without the temperature effect, the amount of energy deficit (ED_a) at time t for selecting the size of the air motor can be given by

$$EDF_a(t) = (E_{pv}(t) \cdot \eta_{pv}) - (E_{dem}(t)/\eta_{co}) \tag{6.1}$$

where $E_{pv}(t)$ is the PV power, η_{pv} is the average efficiency of the PV power output and η_{co} is the converter efficiency. The total energy deficit is given by

$$ED_a = \sum_1^7 EDF_a(t) + \sum_{18}^{24} EDF_a(t) \tag{6.2}$$

The air motor is assumed to provide the output power at the maximum power point (MPP). The power rating of the air motor is found by using the total energy deficit which can be expressed by

$$P_{am} = ED_a/t \cdot \eta_{am} \tag{6.3}$$

where η_{am} is the efficiency of the air motor.

6.2.2.2 Sizing of the battery

Sizing technique for battery is adopted from the sizing method in Chapter 4. In this system, the renewable PV power is used as the primary source while the SS-CAE needs to supply the power

when the PV power is not available. Since the SS-CAES system operating at the MPP cannot maintain the voltage output when it is only used to support the fluctuating load demand, i.e., the battery needs to buffer load fluctuations while the SS-CAES operates at its MPP. To ensure that there is sufficient electrical power supplying to the load demand, the battery system needs to be sized. If the energy demand is greater than the sum of the available energy produced by the PV system and the SS-CAES, the amount of energy deficit covered by the battery will be:

$$EDF_b\,(t) = \left[(E_{pv}(t) \cdot \eta_{pvs}) + (E_{caes}(t) \cdot \eta_{am})\right] - (E_{dem}(t)/\eta_{co}) \qquad (6.4)$$

where $E_{caes}(t)$ is the SS-CAES power and η_{am} is the efficiency of the air motor. The total deficit energy is expressed as

$$ED_b = \sum_{1}^{t1} EDF_b(t) + \sum_{t2}^{24} EDF_b(t) \qquad (6.5)$$

where $t1, t2$ are the start and final times of the duration when $P_{dem}(t) > P_{pv}(t)$. In this thesis, the PV and SS-CAES systems are assumed to operate at MPP in their operating hour interval.

6.3 Results

6.3.1 Air motor size

The air motor size is estimated by considering the total deficit energy between the load demand and generated energy from the PV system. The energy difference between the hourly load demand and the PV system is illustrated in Table 5. The first two columns present hours of the day and the energy demand, respectively. The third column shows generated energy of PV system and the fourth column shows the energy difference (EDF_a) between generated and demand energies in each hour using Eq. (6.1). The energy demand is greater than the generated energy from the PV system at the beginning since there is no solar irradiance until the sunrise. It is lower that the PV energy during day-time period and it is greater again after the sunset until the end of the day. The negative value represents the insufficient generated energy for supporting the load while the positive value donates the surplus energy.

Since the PV system is unable to supply the energy to these deficit directly, the air motor in SS-CAES system is required to generate the energy for compensating the deficit. To estimate the air motor size, the ED_a is considered only the negative values as shown in the last column. The negative values occur within two periods: from the beginning to the time of 10 hr and from the time of 18 hr to 24 hr. The total energy deficit throughout a day (ED_a) is calculated by using Eq. (6.2). The ED_a reaches 5113.0 Whr within a duration of 17 hr. This amount of deficit can be used to estimate the

power rating of the air motor by using Eq. (6.3). Including the air motor efficiency of 85%, the power rating of the air motor is 353.8 W from this calculation.

Hours of a day	E_{dem} (Whr)	E_{PV} (Whr)	EDF_a (Whr)	ED_a (Whr)
1	100.4	0	-100.4	-100.4
2	204.1	0	-204.1	-204.1
3	198.0	0	-198.0	-198.0
4	216.9	0	-216.9	-216.9
5	231.2	0	-231.2	-231.2
6	229.9	0	-229.9	-229.9
7	296.4	0	-296.4	-296.4
8	523.4	0	-523.4	-523.4
9	648.4	0	-648.4	-648.4
10	379.7	117.0	-262.6	-262.6
11	167.1	490.7	323.6	0
12	194.2	2001.2	1807.0	0
13	199.5	1971.2	1771.6	0
14	186.9	716.4	529.5	0
15	200.5	436.1	235.6	0
16	218.0	547.0	329.0	0
17	202.7	483.7	281.0	0
18	293.6	0	-293.6	-293.6
19	507.8	0	-507.8	-507.8
20	436.4	0	-436.4	-436.4
21	241.6	0	-241.6	-241.6
22	232.8	0	-232.8	-232.8
23	243.3	0	-243.3	-243.3
24	246.2	0	-246.2	-246.2
			Total deficit	-5113.0

Table 5 The calculation of deficit energy for air motor's size estimation

6.3.2 Battery size

Fig. 6.3 shows the load demand and the generated powers of the PV and SS-CAES system. At the beginning, the generated power of the SS-CAES can compensate the deficit power of the PV system. At t = t1, the SS-CAES stops the discharging process and turns into the charging process since the PV power is greater than demand power. The discharging process is restarted when the demand power is higher than the generated power at t = t2. It can be seen that the sum of the PV and SS-CAES powers is insufficient to supply the load and hence the battery is required.
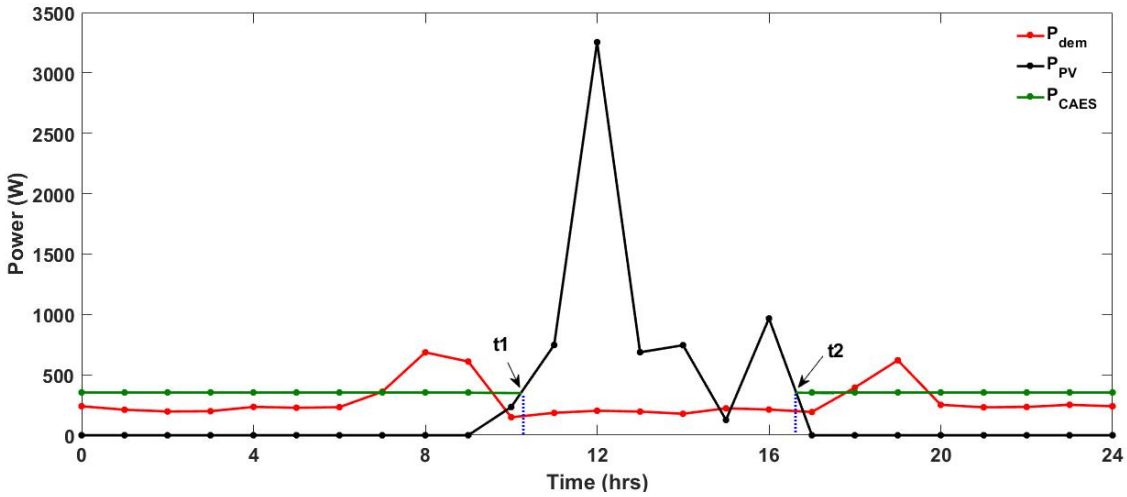
Figure 6.3 The load demand and generated powers

The size of the battery can be determined by considering the energy deficit between the hourly load demand and the sum of the PV power and the average power of the air motor. Consider the energy difference between the hourly load demand and the generated power from the PV and SS-CAES systems illustrated in Table 6. The first two columns present hours of the day and the energy demand, respectively. The generated energy from the PV and SS-CAES systems show in the next two columns, respectively. In the fifth column, the total energy generation from PV and SS-CAES is calculated. The sixth column illustrates the hourly energy difference (EDF_b) between the generation and demand using Eq. (6.4). Obviously, the power generated from both PV and SS-CAES systems is sufficient to supply the required load for several hours as shown on the positive values. However, the generated power is insufficient after the sunset, which is demonstrated on the negative values. The amount of energy deficit (ED_b) is obtained in the last column.

The ED_b is zero within three period, that are from the beginning to the time of 8 hr, the time of 10 hr to 18 hr and the time of 21 hr to the end of a day. These mean that the total power of the SS-CAES system and the PV system is sufficient to support the load. The SS-CAES power compensates the deficit energy between the demand and the PV powers if the demand energy is greater than the PV energy. The ED_b , however, occurs at the two demand peaks, which are from the time of 8 hr to 9 hr and 19 hr to 20 hr. These because the generated powers from both PV and CAES systems cannot meet the power demand. The overall deficit throughout a day reaches approximately 700.0 Whr in 4 hrs. This amount of deficit can be used to estimate the power rating of the battery by using Eq. (6.5). Including the discharge efficiency of 80% and self-discharge loss of 1%, a 900 Whr battery is selected for compensating this amount of the deficit power.

Hours of a day	E_{dem} (Whr)	PV enrgy (Whr)	CAES energy (Whr)	Total Gen.	EDF_b (Whr)	ED_b (Whr)
1	100.4	0	354.0	354.0	253.7	0
2	204.1	0	354.0	354.0	149.9	0
3	198.0	0	354.0	354.0	156.0	0
4	216.9	0	354.0	354.0	137.1	0
5	231.2	0	354.0	354.0	122.8	0
6	229.9	0	354.0	354.0	124.1	0
7	296.4	0	354.0	354.0	57.6	0
8	523.4	0	354.0	354.0	-169.4	-169.4
9	648.4	0	354.0	354.0	-294.4	-294.4
10	379.7	117.0	354.0	471.0	91.4	0
11	167.1	490.7	0	490.7	323.6	0
12	194.2	2001.2	0	2001.2	1807.0	0
13	199.5	1971.2	0	1971.2	1771.6	0
14	186.9	716.4	0	716.4	529.5	0
15	200.5	436.1	0	436.1	235.6	0
16	218.0	547.0	0	547.0	329.0	0
17	202.7	483.7	0	483.7	281.0	0
18	293.6	0	354.0	354.0	60.4	0
19	507.8	0	354.0	354.0	-153.8	-153.8
20	436.4	0	354.0	354.0	-82.4	-82.4
21	241.6	0	354.0	354.0	112.4	0
22	232.8	0	354.0	354.0	121.2	0
23	243.3	0	354.0	354.0	110.7	0
24	246.2	0	354.0	354.0	107.8	0
					Total deficit	-700.0

Table 6 The calculation of deficit energy for battery's size estimation

6.4 Summary

This chapter has investigated the sizing method of the hybrid ESS comprising the SS-CAES system and the battery in the discharging process. The PV system is used as the main energy source while the SS-CAES system is used when the PV power is lower than the load demand. Both systems are assumed to operate at their maximum power points. The battery compensates the deficit power when the total generated powers of the PV and SS-CAES systems cannot meet the load demand.

The sizing method for the air motor, which is the main component of the SS-CAES system in the discharging process, is proposed using the total energy deficit between the PV power and the power demand. The total energy deficit is calculated by the summation of the difference in these powers

in each hour interval. The method includes the system's efficiency, which can accurately estimate the average power rating of the air motor.

The total energy deficit results from the summation of the hourly differences between the total generated power from the PV and SS-CAES systems and the load demand when the latter is greater than the generated power. The battery size is determined by using this calculated energy since the battery has to cover such deficit. Based on these sizing methods and by including efficiencies, the estimated sizes for both components ensure sufficient energy storage for supporting the load within 24 hours.

Chapter 7   Conclusion and future works

7.1   Conclusion

This thesis has been focusing on the HES system comprising the SS-CAES with a battery.

The SS-CAES system and its MPPT controller were studied to understand their operations and designs. A small-signal and state-space averaging analysis of the SS-CAES system with a boost converter were used to achieve the transfer functions for selecting parameters for the controller's stability. The controller's strategy has been selected by comparing between the MEPT and MPPT strategies. It was found that the speed operating point of both controllers are different; the efficiency of the MPPT is 1-3% lower than that of the MEPT at the constant pressure. However, the MEPT requires the accuracy of the air motor characteristics and the use of several sensors such as air flow, pressure and speed sensors. Moreover, the MPPT is more proper for real time tracking since it measures the output power directly.

The MPPT controller was designed by using the P&O method because of its simplicity and popularity. The change of power with respect to the duty cycle of boost converter was used to track the speed operating point. The duty cycle was calculated from the air motor power as a function of boost converter's duty cycle which provides similar results comparing to that from direct measurement. The MPPT controller provided a correct reference speed to control the air motor but it shows a very narrow maximum efficiency peak, which a small deviation from the MPPT leads to the important loss of efficiency.

To improve these issues, the SS-CAES was hybridized with a battery called HES system. The battery can buffer fast load changes while the SS-CAES works at the MPP. The SS-CAES system was connected to the load through a boost converter that controls the air motor's speed to achieve MPP. A bidirectional converter was used to connect the battery to the load and maintain the constant output voltage by the voltage controller. A comparison between the SS-CAES only system controlled in constant voltage mode and hybrid system comprising a SS-CAES with the MPPT controller and a battery with a voltage controller was presented. The results showed that the speed of response of the hybrid system is slightly faster than one using the CAES only system due to the battery supply power to the load during the SS-CAES runs to the MPP. The output power of the proposed hybrid system is matched with the power demand. The battery is charged during the low power demand and is discharged otherwise for maintaining the output voltage while the air motor operates at the MPP. The proposed hybrid system can improve around 47.1% of the SS-CAES efficiency better than that of the SS-CAES controlled by voltage controller.

The component sizes of the hybrid system for a typical household load profile in the Southern region of the UK were estimated within two scenarios, which are the HES only system supplies the load demand during a day and the HES connected in parallel to the PV system supplies the power to the load demand. The difference between the generated power and demand power was used as the method to estimate the sizes of each system's components. The criteria is that the excess energy must be greater than the deficit one. The cost effectiveness is not included in this sizing method.

For using the HES only supplies the load demand, the four power rating of the air motor was compared under the assumption of constant discharge of the air motor for supplying this load profile within 24-hrs period. The results showed that the air motor with power rate at least 270 W was the proper size, which provides the difference between the excess and deficit energies reaching the criteria. The energy deficit was used for determining the battery's size. The overall deficit energy of 1189.3 W-hr was achieved from the sum of that in each hour that needs to be supplied by the 1500 Whr battery including the discharge efficiency around 80% and the self-discharge loss 1%. With these estimating component sizes, the energy storage systems can provide sufficient power for this load.

Another scenario is that the HES connected in parallel to the PV system supplies the power to the load demand. The PV system, which operated at MPP, was used to supply the load and to recharge the SS-CAES while the battery was used during the peak-demand period. The sizing method mentioned previously was used to determine the components' sizes of the whole system for both charging and discharging processes. The PV system consisting of at least 41 PV panels were the minimum numbers that can provide the overall excess energy is greater than the deficit energy. The components' sizes for charging process such as the air tank and compressor were estimated by considering the total excess energy. The results showed that the air tank size of 2.8 m^3 for storing this excess energy was calculated based on the thermodynamic law of the energy conversion and the ideal gas law. To store the overall excess energy within 7 hours, the air compressor with the power rating of 720 W were used.

The component sizes, such as the air motor and battery, have been estimated for discharging process. The power rate of the air motor was determined by considering the deficit energy when the PV system is unavailable. The battery size was also estimated by calculating the deficit energy when the PV and CAES systems are unable to meet the load demand during peak-demand period. The outcomes showed that the air motor with power rate of 353.8 W including the efficiency of 85% was selected to supply the load for 17 hours. In case of peak-demand period, the 900 Whr of

the battery, which include the discharge efficiency around 80% and the self-discharge loss 1% was the appropriate size for compensating the energy in 4 hours.

The sizing method developed in this work can be used as the guideline for other load demand profile, such as the shop or office building.

7.2   Future work

As the aim of this project has been successfully achieved under the limit time, some aspects related to this thesis have not been carried out. The further recommended works are list as follows:

7.2.1   Dynamic investigation for the whole system.

The investigations in this research project are run by the separate simulations of the PV system and hybrid EES comprising SS-CAES and battery. The whole system, which employs the PV system as primary source and hybrid ESS system as the energy storing elements, should be simulated for study the dynamic behaviour of the system. With successful estimations of each component' size, three sources are connected with the household load via the different converters. The PV system is connected through a boost converter to the load while the SS-CAES and battery are connected in parallel through the bidirectional converters. The supervisory controller will be designed to manage the power flow. The system will cooperates smoothly. As a result of doing this, the accuracy of the components' sizes will be confirmed. The hybrid ESS system might be able to meet the desired load demand when the PV system is unavailable.

7.2.2   The experimental model

Since the experimental data for the full hybrid system has not demonstrated, the experimental investigation for a hybrid system is highly recommended for validation. The model of the proposed hybrid ESS system should be built. As a result of doing this, the simulation results of the hybrid SS-CAEs with a battery system will be validated. Then, the model of PV system, which is connected through its converter to the selected household load, will be connected in parallel with the hybrid ESS. In this case, the proposed power rates of the compressor and air motor will be employed for charging and discharging processes, respectively. The experimental results will be used to validate the outcomes of the simulation, which leads to the accuracy of the simulation models.

List of References

[1]   X. Luo, J. Wang, M. Dooner, J. Clarke, and C. Krupke, "Overview of current development in compressed air energy storage technology," *Energy Procedia*, vol. 62, pp. 603–611, 2014.

[2]   M. AbuAisha and A. Rouabhi, "On the validity of the uniform thermodynamic state approach for underground caverns during fast and slow cycling," *Int. J. Heat Mass Transf.*, vol. 142, no. April, p. 81, 2019.

[3]   H. Chen, T. N. Cong, W. Yang, C. Tan, Y. Li, and Y. Ding, "Progress in electrical energy storage system: A critical review," *Prog. Nat. Sci.*, vol. 19, no. 3, pp. 291–312, 2009.

[4]   V. Kokaew, S. M. Sharkh, and M. Moshrefi-Torbati, "A hybrid method for maximum power tracking of a small scale CAES system," *2014 9th Int. Symp. Commun. Syst. Networks Digit. Signal Process. CSNDSP 2014*, pp. 61–66, 2014.

[5]   G. Venkataramani, P. Parankusam, V. Ramalingam, and J. Wang, "A review on compressed air energy storage – A pathway for smart grid and polygeneration," *Renew. Sustain. Energy Rev.*, vol. 62, pp. 895–907, 2016.

[6]   J. J. Wang *et al.*, "Overview of compressed air energy storage and technology development," *Energies*, vol. 10, no. 7, 2017.

[7]   C. Bullough *et al.*, "Advanced Adiabatic Compressed Air Energy Storage for the Integration of Wind Energy AA - CAES = Advanced Adiabatic - Compressed Air Energy Storage No fuel used / no CO 2 emissions at point of storage .," pp. 1–8, 2012.

[8]   Q. Yu, Q. Wang, X. Tan, G. Fang, and J. Meng, "A review of compressed-air energy storage," *J. Renew. Sustain. Energy*, vol. 11, no. 4, 2019.

[9]   M. Budt, D. Wolf, R. Span, and J. Yan, "A review on compressed air energy storage: Basic principles, past milestones and recent developments," *Appl. Energy*, vol. 170, pp. 250–268, 2016.

[10]   X. Zhang *et al.*, "A near-isothermal expander for isothermal compressed air energy storage system," *Appl. Energy*, vol. 225, no. May, pp. 955–964, 2018.

[11]   J. Guanwei, X. Weiqing, C. Maolin, and S. Yan, "Micron-sized water spray-cooled quasi-isothermal compression for compressed air energy storage," *Exp. Therm. Fluid Sci.*, vol. 96, no. September 2017, pp. 470–481, 2018.

List of References

[12]   S. Lemofouet, "Investigation and optimisation of hybrid electricity storage systems based on compressed air and supercapacitors," vol. 3628, p. 11, 2006.

[13]   V. Kokaew, M. Moshrefi-Torbati, and S. M. Sharkh, "Maximum efficiency or power tracking of stand-alone small scale compressed air energy storage system," *Energy Procedia*, vol. 42, no. 0, pp. 387–396, 2013.

[14]   V. Kokaew, S. M. Sharkh, and M. Moshrefi-Torbati, "Maximum Power Point Tracking of a Small-Scale Compressed Air Energy Storage System," University of Southampton, 2016.

[15]   A. Setiawan, A. Priyadi, M. Pujiantara, and M. H. Purnomo, "Sizing compressed-air energy storage tanks for solar home systems," *2015 IEEE Int. Conf. Comput. Intell. Virtual Environ. Meas. Syst. Appl. CIVEMSA 2015*, no. December, 2015.

[16]   B. Küçük, İ. Atacak, and Ç. Elmas, "Simulation of a Hybrid Compressed Air / Li-Ion Battery Energy Storage System for Electric Vehicles," *Isites*, no. January, pp. 319–328, 2015.

[17]   P. Omsin, S. M. Sharkh, and M. Moshrefi-Torbati, "A hybrid ss-caes system with a battery," in *Proceedings of the 16th International Conference on Electrical Engineering/Electronics, Computer, Telecommunications and Information Technology, ECTI-CON 2019*, 2019, pp. 159–162.

[18]   P. Omsin, S. M. Sharkh, and M. Moshrefi-Torbati, "Control and Sizing of a Hybrid Battery and Compressed Air Energy Storage system," pp. 193–198, 2020.

[19]   I. Hadjipaschalis, A. Poullikkas, and V. Efthimiou, "Overview of current and future energy storage technologies for electric power applications," *Renew. Sustain. Energy Rev.*, vol. 13, no. 6–7, pp. 1513–1522, 2009.

[20]   H. Struchtrup, *Thermodynamics and*, vol. 36, no. 1. 1996.

[21]   H. Sedighnejad, T. Iqbal, and J. Quaicoe, "Compressed air energy storage system control and performance assessment using energy harvested index," *Electron.* , vol. 3, no. 1, pp. 1–21, 2014.

[22]   M. Moshrefi-Torbati, "Lecture 30- Compressed Air Energy Storage (CAES)," Southampton, UK, 2019.

[23]   F. Crotogino, K.-U. Mohmeyer, and R. Scharf, "Huntorf CAES: More than 20 Years of Successful Operation," *Solut. Min. Res. Inst. Spring Meet.*, no. April, pp. 351–357, 2001.

[24]   T. M. I. Mahlia, T. J. Saktisahdan, A. Jannifar, M. H. Hasan, and H. S. C. Matseelar, "A review

of available methods and development on energy storage; Technology update," *Renew. Sustain. Energy Rev.*, vol. 33, no. May, pp. 532–545, 2014.

[25]   S. Succar, "Compressed air energy storage," *Large Energy Storage Syst. Handb.*, pp. 111–152, 2011.

[26]   X. Luo, J. Wang, M. Dooner, and J. Clarke, "Overview of current development in electrical energy storage technologies and the application potential in power system operation," *Appl. Energy*, vol. 137, pp. 511–536, 2015.

[27]   M. Nakhamkin, M. Chiruvolu, and C. Daniel, "Available compressed air energy storage (CAES) plant concepts," *Energy*, p. 8, 2007.

[28]   ESPC, "CAES air injection with expander extraction," 2012. [Online]. Available: http://www.espcinc.com/mobile/index.php?option=com_k2&view=item&id=8:caes-air-injection-with-expander-extraction&Itemid=3. [Accessed: 04-Aug-2020].

[29]   M. A. Rosen, "Energy storage technology," *Energy Storage*, no. January 2010, pp. 3–45, 2012.

[30]   Sustainx, "Isothermal CAES Technology," *Energy Storage Association*, 2019. [Online]. Available: http://energystorage.org/energy-storage/technologies/isothermal-caes. [Accessed: 04-Sep-2017].

[31]   Y. M. Kim, J. H. Lee, S. J. Kim, and D. Favrat, "Potential and evolution of compressed air energy storage: Energy and exergy analyses," *Entropy*, vol. 14, no. 8, pp. 1501–1521, 2012.

[32]   Z. Fu, L. I. Jing, C. Da, and L. I. U. Hui, "Image Segmentation Method about Mathematical Morphology Based on Textural Features," *Köln:*, pp. 5–7, 2008.

[33]   D. O. Akinyele and R. K. Rayudu, "Review of energy storage technologies for sustainable power networks," *Sustain. Energy Technol. Assessments*, vol. 8, pp. 74–91, 2014.

[34]   S. D. Lim, A. P. Mazzoleni, J. K. Park, P. I. Ro, and B. Quinlan, "Conceptual design of ocean compressed air energy storage system," *Ocean. 2012 MTS/IEEE Harnessing Power Ocean*, pp. 1–8, 2012.

[35]   V. Vongmanee and V. Monyakul, "A new concept of small-compressed air energy storage system integrated with induction generator," *2008 IEEE Int. Conf. Sustain. Energy Technol. ICSET 2008*, pp. 866–871, 2008.

[36]   P. Barrade, S. Delalay, and A. Rufer, "Direct connection of supercapacitors to photovoltaic

panels with on-off maximum power point tracking," *IEEE Trans. Sustain. Energy*, vol. 3, no. 2, pp. 283–294, 2012.

[37]   M. Martínez, M. G. Molina, and P. E. Mercado, "Dynamic performance of Compressed Air Energy Storage (CAES) plant for applications in power systems," *2010 IEEE/PES Transm. Distrib. Conf. Expo. Lat. Am. T D-LA 2010*, pp. 496–503, 2011.

[38]   V. Kokaew, M. Moshrefi-Torbati, and S. M. Sharkh, "Simulation of a solar powered air compressor," *2011 10th Int. Conf. Environ. Electr. Eng. EEEIC.EU 2011 - Conf. Proc.*, no. 6, pp. 6–9, 2011.

[39]   Y. M. Kim, "Novel concepts of compressed air energy storage and thermo-electric energy storage," vol. 5525, 2012.

[40]   M. V. Dahraie, H. R. Najafi, R. N. Azizkandi, and M. R. Nezamdoust, "Study on compressed air energy storage coupled with a wind farm," *2012 2nd Iran. Conf. Renew. Energy Distrib. Gener. ICREDG 2012*, no. 1, pp. 147–152, 2012.

[41]   Y. M. Kim and D. Favrat, "Energy and exergy analysis of a micro-compressed air energy storage and air cycle heating and cooling system," *Energy*, vol. 35, no. 1, pp. 213–220, 2010.

[42]   M. C. Chen, J. R. Anderson, and M. H. Sohn, "What can a mouse cursor tell us more? Correlation of eye/mouse movements on web browsing," 2001.

[43]   S. Lemofouet and A. Rufer, "A hybrid energy storage system based on compressed air and supercapacitors with maximum efficiency point tracking (MEPT)," *IEEE Trans. Ind. Electron.*, vol. 53, no. 4, pp. 1105–1115, 2006.

[44]   J. D. Van de Ven and P. Y. Li, "Liquid piston gas compression," *Appl. Energy*, vol. 86, no. 10, pp. 2183–2191, 2009.

[45]   C. Qin and E. Loth, "Liquid piston compression efficiency with droplet heat transfer," *Appl. Energy*, vol. 114, pp. 539–550, 2014.

[46]   F. Yang, G. Li, J. Hua, X. Li, and T. Kagawa, "A new method for analysing the pressure response delay in a pneumatic brake system caused by the influence of transmission pipes," *Appl. Sci.*, vol. 7, no. 9, 2017.

[47]   M. Saadat, F. A. Shirazi, and P. Y. Li, "Modeling and trajectory optimization of water spray cooling in a liquid piston air compressor," *ASME 2013 Heat Transf. Summer Conf.*

Collocated with ASME 2013 7th Int. Conf. Energy Sustain. ASME 2013 11th Int. Conf. Fuel Cell Sci. Eng. Technol. HT 2013, vol. 2, no. July, 2013.

[48]   M. Utamura, "Powrn presented THE 1999 0 : NT 1NTERNAT10NAL • v • Œ BURL : NGAME," no. April, 2019.

[49]   B. C. Cheung, R. Carriveau, and D. S. K. Ting, "Parameters affecting scalable underwater compressed air energy storage," *Appl. Energy*, vol. 134, pp. 239–247, 2014.

[50]   Hydrostor, "Underwater Compressed Air Energy Storage," *2019 IEEE 5th World Forum Internet Things*, no. November, pp. 6–19, 2019.

[51]   M. Beaudin, H. Zareipour, A. Schellenberglabe, and W. Rosehart, "Energy storage for mitigating the variability of renewable electricity sources: An updated review," *Energy Sustain. Dev.*, vol. 14, no. 4, pp. 302–314, 2010.

[52]   S. Hajiaghasi, A. Salemnia, and M. Hamzeh, "Hybrid energy storage system for microgrids applications: A review," *J. Energy Storage*, vol. 21, no. December 2018, pp. 543–570, 2019.

[53]   T. Alnejaili, S. Drid, D. Mehdi, L. Chrifi-Alaoui, R. Belarbi, and A. Hamdouni, "Dynamic control and advanced load management of a stand-alone hybrid renewable power system for remote housing," *Energy Convers. Manag.*, vol. 105, pp. 377–392, 2015.

[54]   G. Wang, M. Ciobotaru, and V. G. Agelidis, "Power smoothing of large solar PV plant using hybrid energy storage," *IEEE Trans. Sustain. Energy*, vol. 5, no. 3, pp. 834–842, 2014.

[55]   Y. Y. Chia, L. H. Lee, N. Shafiabady, and D. Isa, "A load predictive energy management system for supercapacitor-battery hybrid energy storage system in solar application using the Support Vector Machine," *Appl. Energy*, vol. 137, pp. 588–602, 2015.

[56]   S. Wang *et al.*, "Design and advanced control strategies of a hybrid energy storage system for the grid integration of wind power generations," *IET Renew. Power Gener.*, vol. 9, no. 2, pp. 89–98, 2015.

[57]   A. Etxeberria, I. Vechiu, H. Camblong, and J. M. Vinassa, "Hybrid energy storage systems for renewable energy sources integration in microgrids: A review," *2010 9th Int. Power Energy Conf. IPEC 2010*, pp. 532–537, 2010.

[58]   R. Hemmati and H. Saboori, "Emergence of hybrid energy storage systems in renewable energy and transport applications – A review," *Renew. Sustain. Energy Rev.*, vol. 65, pp. 11–23, 2016.

List of References

[59]   E. Chemali, M. Preindl, P. Malysz, and A. Emadi, "Electrochemical and Electrostatic Energy Storage and Management Systems for Electric Drive Vehicles: State-of-the-Art Review and Future Trends," *IEEE J. Emerg. Sel. Top. Power Electron.*, vol. 4, no. 3, pp. 1117–1134, 2016.

[60]   H. El Fadil, F. Giri, J. M. Guerrero, and A. Tahri, "Modeling and nonlinear control of a fuel cell/supercapacitor hybrid energy storage system for electric vehicles," *IEEE Trans. Veh. Technol.*, vol. 63, no. 7, pp. 3011–3018, 2014.

[61]   M. Zandi, A. Payman, J. P. Martin, S. Pierfederici, B. Davat, and F. Meibody-Tabar, "Energy management of a fuel cell/supercapacitor/battery power source for electric vehicular applications," *IEEE Trans. Veh. Technol.*, vol. 60, no. 2, pp. 433–443, 2011.

[62]   O. Onar and A. Khaligh, "Hybrid Energy Storage Systems," no. April, pp. 283–316, 2014.

[63]   A. Morandi, L. Trevisani, F. Negrini, P. L. Ribani, and M. Fabbri, "Feasibility of superconducting magnetic energy storage on board of ground vehicles with present state-of-the-art superconductors," *IEEE Trans. Appl. Supercond.*, vol. 22, no. 2, 2012.

[64]   Z. Nie, X. Xiao, Q. Kang, R. Aggarwal, H. Zhang, and W. Yuan, "SMES-Battery energy storage system for conditioning outputs from direct drive linear wave energy converters," *IEEE Trans. Appl. Supercond.*, vol. 23, no. 3, 2013.

[65]   G. N. Prodromidis and F. A. Coutelieris, "Simulations of economical and technical feasibility of battery and flywheel hybrid energy storage systems in autonomous projects," *Renew. Energy*, vol. 39, no. 1, pp. 149–153, 2012.

[66]   H. Lee, B. Y. Shin, S. Han, S. Jung, B. Park, and G. Jang, "Compensation for the power fluctuation of the large scale wind farm using hybrid energy storage applications," *IEEE Trans. Appl. Supercond.*, vol. 22, no. 3, pp. 0–3, 2012.

[67]   M. Sander, R. Gehring, H. Neumann, and T. Jordan, "LIQHYSMES storage unit - Hybrid energy storage concept combining liquefied hydrogen with Superconducting Magnetic Energy Storage," *Int. J. Hydrogen Energy*, vol. 37, no. 19, pp. 14300–14306, 2012.

[68]   M. Martinez, M. G. Molina, F. Frack, and P. E. Mercado, "Dynamic modeling, simulation and control of hybrid energy storage system based on compressed air and supercapacitors," *IEEE Lat. Am. Trans.*, vol. 11, no. 1, pp. 466–472, 2013.

[69]   P. Zhao, Y. Dai, and J. Wang, "Design and thermodynamic analysis of a hybrid energy storage system based on A-CAES (adiabatic compressed air energy storage) and FESS (flywheel energy storage system) for wind power application," *Energy*, vol. 70, pp. 674–

684, 2014.

[70]   IEC, "Executive summary," *Ann. ICRP*, vol. 39, no. 4, pp. 11–12, 2009.

[71]   Atlas Copcp, "Atlas Copco Manual.," 1978. [Online]. Available:
         https://webbox.atlascopco.com/airmotor/airmotor.html. [Accessed: 05-Jun-2018].

[72]   Z. M. Dalala, Z. U. Zahid, W. Yu, Y. Cho, and J. S. Lai, "Design and analysis of an MPPT
         technique for small-scale wind energy conversion systems," *IEEE Trans. Energy Convers.*,
         vol. 28, no. 3, pp. 756–767, 2013.

[73]   F. Paz and M. Ordonez, "Zero oscillation and irradiance slope tracking for photovoltaic
         MPPT," *IEEE Trans. Ind. Electron.*, vol. 61, no. 11, pp. 6138–6147, 2014.

[74]   M. M. R. Singaravel and S. A. Daniel, "MPPT with Single DC-DC Converter and Inverter for
         Grid-Connected Hybrid Wind-Driven PMSG-PV System," *IEEE Trans. Ind. Electron.*, vol. 62,
         no. 8, pp. 4849–4857, 2015.

[75]   A. Merabet, M. A. Islam, and R. Beguenane, "Predictive speed controller for laboratory size
         wind turbine experiment system," *Can. Conf. Electr. Comput. Eng.*, pp. 1–6, 2014.

[76]   C. Xia, C. Xia, Q. Geng, T. Shi, Z. Song, and X. Gu, "Input–Output Feedback Linearization and
         Speed Control of a Surface Permanent-Magnet Synchronous Wind Generator with the
         Boost-Chopper Converter," *IEEE Trans. Ind. Electron.*, vol. 59, no. 9, pp. 3489–3500, 2012.

[77]   S. M. R. Kazmi, H. Goto, H. J. Guo, and O. Ichinokura, "A novel algorithm for fast and
         efficient speed-sensorless maximum power point tracking in wind energy conversion
         systems," *IEEE Trans. Ind. Electron.*, vol. 58, no. 1, pp. 29–36, 2011.

[78]   N. O. Kislovski, A.S., Redl, R., Sokal, *Dynamic analysis of swiitching-mode DC/DC converter*.
         New York: Van Nostrand Reinhold, 1991.

[79]   V. Vorpérian, "Simplified Analysis of Pwm Converters Using Model of Pwm Switch Part I:
         Continuous Conduction Mode," *IEEE Trans. Aerosp. Electron. Syst.*, vol. 26, no. 3, pp. 490–
         496, 1990.

[80]   W. M. Moussa and J. E. Morris, "Comparison between state space averaging and PWM
         switch for switch mode power supply analysis," *Trans. Tech. Sect. Can. Pulp Pap. Assoc.*,
         pp. 15–21, 1990.

[81]   R. H. G. Tan and L. Y. H. Hoo, "DC-DC converter modeling and simulation using state space
         approach," *2015 IEEE Conf. Energy Conversion, CENCON 2015*, no. 2, pp. 42–47, 2015.

List of References

[82]   M. S. Sivagamasundari, P. M. Mary, and V. K. Velvizhi, "Maximum Power Point Tracking For Photovoltaic System by Perturb and Observe Method Using Buck Boost Converter," *Int. J. Adv. Res. Electr. Electron. adn Instrum. Eng.*, vol. 2, no. 6, pp. 2433–2439, 2013.

[83]   F. Fayaz, "Maximum Power Point Tracking Algorithms for Photovoltaic Applications," Aalto University, 2019.

[84]   H. N. Zainudin and S. Mekhilef, "Comparison Study of Maximum Power Point Tracker Techniques for PV Systems," *Proc. 14th Int. Middle East Power Syst. Conf. (MEPCON'10), Cairo Univ. Egypt*, no. 1, pp. 750–755, 2010.

[85]   R. I. Putri, S. Wibowo, and M. Rifa'i, "Maximum power point tracking for photovoltaic using incremental conductance method," *Energy Procedia*, vol. 68, no. June, pp. 22–30, 2015.

[86]   P. Balamurali and C. Ravikumar, "Comparison of Perturb and Observe Mppt for Pv Systems Conjuction With Buck Buck-Boost Converters Abstract :," vol. 3, no. 6, pp. 269–277, 2015.

[87]   T. Esram and P. L. Chapman, "Comparison of photovoltaic array maximum power point tracking techniques," *IEEE Trans. Energy Convers.*, vol. 22, no. 2, pp. 439–449, 2007.

[88]   K. H. Hussein, I. Muta, T. Hoshino, and M. Osakada, "Maximum photovoltaic power tracking: an algorithm for rapidly changing atmospheric conditions," *IEE Proc. Gener. Transm. Distrib.*, vol. 142, no. 1, pp. 59–64, 1995.

[89]   A. Al Nabulsi, R. Dhaouadi, and S. Member, "Nabulsi, Dhaouadi, Member - 2011 - Efficiency Optimization of a DSP-Based Standalone PV System using Fuzzy Logic and Dual-MPPT Control-annotated.pdf," vol. 8, no. 3, pp. 1–12, 2012.

[90]   L. Morales and H. Sudborough, "A quadratic lower bound for Topswops," *Theor. Comput. Sci.*, vol. 411, no. 44–46, pp. 3965–3970, 2010.

[91]   M. A. Elgendy, B. Zahawi, and D. J. Atkinson, "Assessment of the incremental conductance maximum power point tracking algorithm," *IEEE Trans. Sustain. Energy*, vol. 4, no. 1, pp. 108–117, 2013.

[92]   M. A. Elgendy, B. Zahawi, and D. J. Atkinson, "Assessment of perturb and observe MPPT algorithm implementation techniques for PV pumping applications," *IEEE Trans. Sustain. Energy*, vol. 3, no. 1, pp. 21–33, 2012.

[93]   D. P. Hohm and M. E. Ropp, "Comparative study of maximum power point tracking algorithms using an experimental, programmable, maximum power point tracking test

bed," *Conf. Rec. IEEE Photovolt. Spec. Conf.*, vol. 2000-Janua, pp. 1699–1702, 2000.

[94]   M. K. Kazimierczuk, *Power Converters Pulse-width Modulated DC – DC Power Converters*. 2008.

[95]   A. Ang, S., Oliva, *Power-Switching Converters*. FL, USA.: Taylor & Francis, 2005.

[96]   K. J. Astrom and T. HÄgglund, *Advanced PID control*, vol. 26, no. 1. ISA-The Instrumentation System and Automation Society, 2006.

[97]   S. J. Mason, "Feedback theory: Properties of signal flow graphs," *Algorithmic Tech. Polym. Sci.*, vol. 44, no. 7, pp. 75–124, 2014.

[98]   H. Ibrahim, A. Ilinca, and J. Perron, "Energy storage systems-Characteristics and comparisons," *Renew. Sustain. Energy Rev.*, vol. 12, no. 5, pp. 1221–1250, 2008.

[99]   S. Koohi-Fayegh and M. A. Rosen, "A review of energy storage types, applications and recent developments," *J. Energy Storage*, vol. 27, no. October 2019, p. 101047, 2020.

[100]   P. J. Hall and E. J. Bain, "Energy-storage technologies and electricity generation," *Energy Policy*, vol. 36, no. 12, pp. 4352–4355, 2008.

[101]   J. Baker, "New technology and possible advances in energy storage," *Energy Policy*, vol. 36, no. 12, pp. 4368–4373, 2008.

[102]   J. Hou, Y. Shao, M. W. Ellis, R. B. Moore, and B. Yi, "Graphene-based electrochemical energy conversion and storage: Fuel cells, supercapacitors and lithium ion batteries," *Phys. Chem. Chem. Phys.*, vol. 13, no. 34, pp. 15384–15402, 2011.

[103]   N. Nitta, F. Wu, J. T. Lee, and G. Yushin, "Li-ion battery materials: Present and future," *Mater. Today*, vol. 18, no. 5, pp. 252–264, 2015.

[104]   Y. Chang, X. Mao, Y. Zhao, S. Feng, H. Chen, and D. Finlow, "Lead-acid battery use in the development of renewable energy systems in China," *J. Power Sources*, vol. 191, no. 1, pp. 176–183, 2009.

[105]   G. J. May, A. Davidson, and B. Monahov, "Lead batteries for utility energy storage: A review," *J. Energy Storage*, vol. 15, pp. 145–157, 2018.

[106]   R. A. Huggins and S. Edition, *Energy Storage*. .

[107]   X. Wang, D. Yu, S. Le Blond, Z. Zhao, and P. Wilson, "A novel controller of a battery-supercapacitor hybrid energy storage system for domestic applications," *Energy Build.*, vol.

141, pp. 167–174, 2017.

[108] H. Paloheimo and M. Omidiora, "A feasibility study on compressed air energy storage system for portable electrical and electronic devices," *2009 Int. Conf. Clean Electr. Power, ICCEP 2009*, pp. 355–362, 2009.

[109] M. J. Zimbro, D. A. Power, S. M. Miller, G. E. Wilson, and J. A. Johnson, "Difco & BBL Manual: Manual of Microbiological Culture Media," *Citeseer*. p. 289, 2009.

[110] Toyota (GB) PLC., "Toyota Hybrid Cars," 2020. [Online]. Available: https://www.toyota.co.uk/hybrid/. [Accessed: 04-Jul-2020].

[111] M. S. Whittingham, "History, evolution, and future status of energy storage," *Proc. IEEE*, vol. 100, no. SPL CONTENT, pp. 1518–1534, 2012.

[112] S. Vazquez, S. M. Lukic, E. Galvan, L. G. Franquelo, and J. M. Carrasco, "Energy storage systems for transport and grid applications," *IEEE Trans. Ind. Electron.*, vol. 57, no. 12, pp. 3881–3895, 2010.

[113] J. F. Peters, M. Baumann, B. Zimmermann, J. Braun, and M. Weil, "The environmental impact of Li-Ion batteries and the role of key parameters – A review," *Renew. Sustain. Energy Rev.*, vol. 67, pp. 491–506, 2017.

[114] V. Agarwal, K. Uthaichana, R. A. Decarlo, and L. H. Tsoukalas, "Development and validation of a battery model useful for discharging and charging power control and lifetime estimation," *IEEE Trans. Energy Convers.*, vol. 25, no. 3, pp. 821–835, 2010.

[115] X. Han *et al.*, "A review on the key issues of the lithium ion battery degradation among the whole life cycle," *eTransportation*, vol. 1, p. 100005, 2019.

[116] C. Naish, I. McCubbin, O. Edberg, and M. Harfoot, "Outlook of Energy Storage Technologies," *Eur. Parliam. - Policy Dep. - Econ. Sci. Policy*, no. february, pp. 1–57, 2008.

[117] W. Jing, C. H. Lai, W. S. H. Wong, and M. L. D. Wong, "Dynamic power allocation of battery-supercapacitor hybrid energy storage for standalone PV microgrid applications," *Sustain. Energy Technol. Assessments*, vol. 22, no. January 2018, pp. 55–64, 2017.

[118] X. Liu, P. Wang, P. C. Loh, F. Gao, and F. H. Choo, "Control of hybrid battery/ultra-capacitor energy storage for stand-alone photovoltaic system," *2010 IEEE Energy Convers. Congr. Expo. ECCE 2010 - Proc.*, pp. 336–341, 2010.

[119] Z. Jiancheng and J. Liantao, "An effective hybrid energy storage system based on battery-

EDLC for distributed generation systems," *Proc. 2010 5th IEEE Conf. Ind. Electron. Appl. ICIEA 2010*, pp. 819–824, 2010.

[120] F. Nejabatkhah, S. Danyali, S. H. Hosseini, M. Sabahi, and S. M. Niapour, "Modeling and control of a new three-input dc-dc boost converter for hybrid PV/FC/battery power system," *IEEE Trans. Power Electron.*, vol. 27, no. 5, pp. 2309–2324, 2012.

[121] O. Ekren and B. Y. Ekren, "Size optimization of a PV/wind hybrid energy conversion system with battery storage using simulated annealing," *Appl. Energy*, vol. 87, no. 2, pp. 592–598, 2010.

[122] S. Aissou, D. Rekioua, N. Mezzai, T. Rekioua, and S. Bacha, "Modeling and control of hybrid photovoltaic wind power system with battery storage," *Energy Convers. Manag.*, vol. 89, pp. 615–625, 2015.

[123] B. Madaci, R. Chenni, E. Kurt, and K. E. Hemsas, "Design and control of a stand-alone hybrid power system," *Int. J. Hydrogen Energy*, vol. 41, no. 29, pp. 12485–12496, 2016.

[124] N. Bigdeli, "Optimal management of hybrid PV/fuel cell/battery power system: A comparison of optimal hybrid approaches," *Renew. Sustain. Energy Rev.*, vol. 42, pp. 377–393, 2015.

[125] H. Jung, H. Wang, and T. Hu, "Control design for robust tracking and smooth transition in power systems with battery/supercapacitor hybrid energy storage devices," *J. Power Sources*, vol. 267, pp. 566–575, 2014.

[126] S. Moghaddam, M. Bigdeli, M. Moradlou, and P. Siano, "Designing of stand-alone hybrid PV/wind/battery system using improved crow search algorithm considering reliability index," *Int. J. Energy Environ. Eng.*, vol. 10, no. 4, pp. 429–449, 2019.

[127] B. G. Pollet, I. Staffell, and J. L. Shang, "Current status of hybrid, battery and fuel cell electric vehicles: From electrochemistry to market prospects," *Electrochim. Acta*, vol. 84, pp. 235–249, 2012.

[128] A. Rushby, Thomas W and Anderson, Ben and James, P. A. B. and Bahaj, "Solent Achieving Value from Efficiency (SAVE): randomised control trial household electricity demand data 2017-2018.[Data Collection]," Southampton, 2019.

[129] R. I. Putri and M. Rifa'i, "Maximum Power Point Tracking Control for Photovoltaic System Using Neural Fuzzy," *Int. J. Comput. Electr. Eng.*, no. January, pp. 75–81, 2012.

List of References

[130]   W. EL-BASIT, "Mathematical Model for Photovoltaic Cells," *Leonardo J. …*, no. 23, pp. 13–28, 2013.

[131]   V. Khanna, B. K. Das, and D. Bisht, "Matlab/simelectronics models based study of solar cells," *Int. J. Renew. Energy Res.*, vol. 3, no. 1, pp. 30–34, 2013.

[132]   K. Ding, X. Bian, H. Liu, and T. Peng, "A MATLAB-simulink-based PV module model and its application under conditions of nonuniform irradiance," *IEEE Trans. Energy Convers.*, vol. 27, no. 4, pp. 864–872, 2012.

[133]   N. Pandiarajan and R. Muthu, "Mathematical modeling of photovoltaic module with Simulink," *2011 1st Int. Conf. Electr. Energy Syst. ICEES 2011*, pp. 258–263, 2011.

[134]   S. Abouda, F. Nollet, N. Essounbouli, A. Chaari, and Y. Koubaa, "Design, simulation and voltage control of standalone photovoltaic system based MPPT: Application to a pumping system," *Int. J. Renew. Energy Res.*, vol. 3, no. 3, pp. 538–549, 2013.

[135]   M. H. Moradi and A. R. Reisi, "A hybrid maximum power point tracking method for photovoltaic systems," *Sol. Energy*, vol. 85, no. 11, pp. 2965–2976, 2011.

[136]   PVGIS, "Photovoltaic Geographical Information System," *EU Science Hub - European Commission*, 2020. [Online]. Available: https://re.jrc.ec.europa.eu/%0Ahttps://ec.europa.eu/jrc/en/pvgis. [Accessed: 27-Jan-2020].

[137]   D. B. Nelson, M. H. Nehrir, and C. Wang, "Unit sizing and cost analysis of stand-alone hybrid wind/PV/fuel cell power generation systems," *Renew. Energy*, vol. 31, no. 10, pp. 1641–1656, 2006.

[138]   Panasonic, "Panasonic Solar," 2019. [Online]. Available: https://eu-solar.panasonic.net/en/solar-panel-vbhn240sj25-vbhn245sj25.htm. [Accessed: 22-Mar-2020].

Appendix A   The characteristics model of the air motor

The air motor model is also created based on Eq. (3.1) – (3.6) focusing on the pneumatic to mechanical energy conversion. The pressure and air consumption are defined as the air motor input while its outputs are specified as the torque and speed which is equal to the generator's speed because of coupling with the same shaft. The subsystem models of the air motor characteristics are illustrated in Fig. A.1.
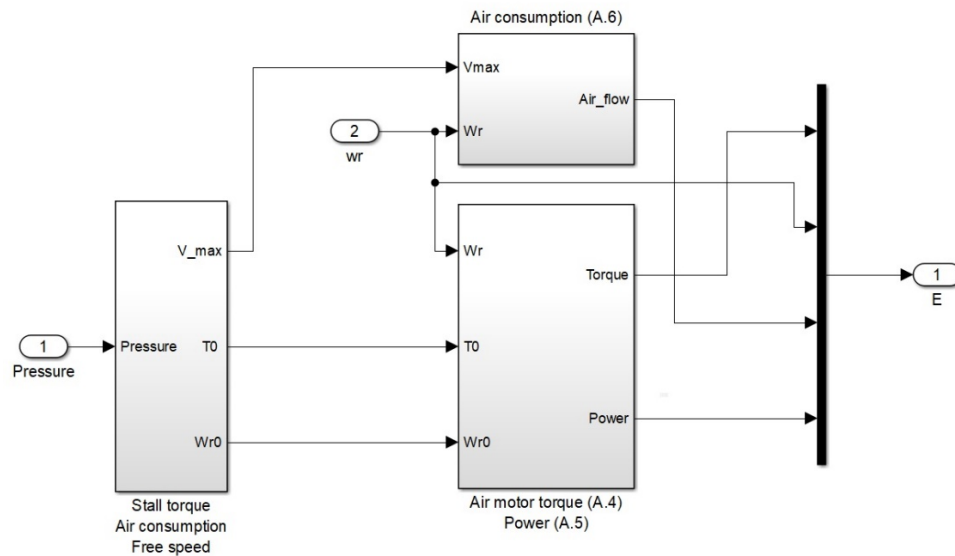

Figure A.7.1 Subsystem of air motor model

As can be seen, there are three subsystem blocks of the mathematical model of the air motor that are the boundary adjustment block, the block of speed to power/torque and air consumption block. Starting with the boundary block adjustment for maximum air consumption, this block is created from Eq. (3.1) – (3.3), as shown in Fig. A.2.
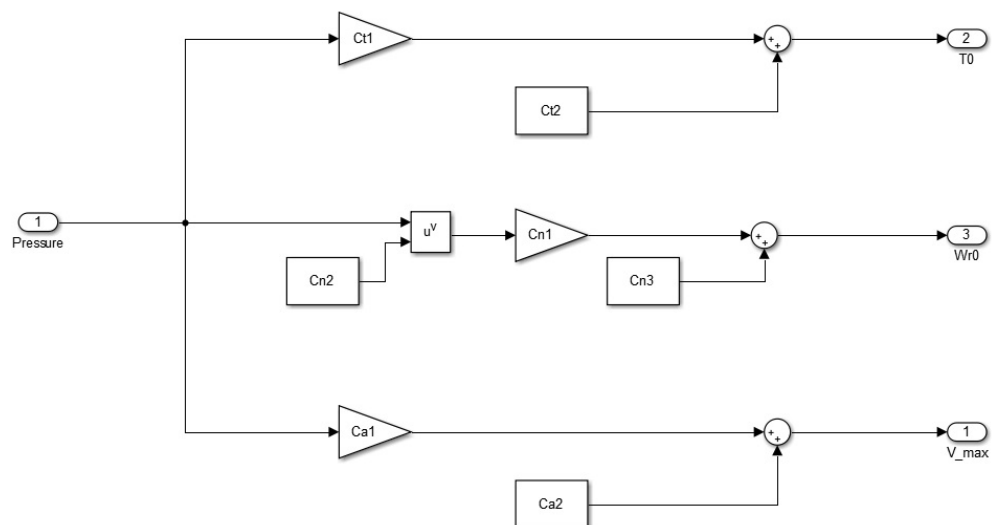
Figure A.7.2 The adjustment of boundary block

The real constant parameters in Fig. A.2 (C_{t1}, C_{t2}, C_{n1}, C_{n2}, C_{n3}, C_{a1} and C_{a2}) are obtained by using the curve-fitting toolbox in Matlab/Simulink. These parameters need to be filled in the function block parameters of the air motor, presented in Fig. A.3, in order to approximate the mathematical model.
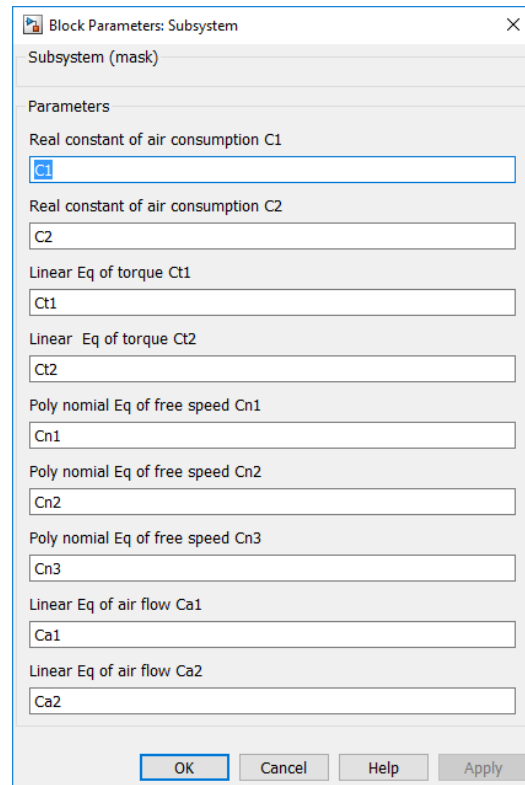
Figure A.7.3 Function block parameters of the air motor

Next, the block of speed to power and torque output is created by using Eq. (3.4) and (3.5) as presented in Fig. A.4.
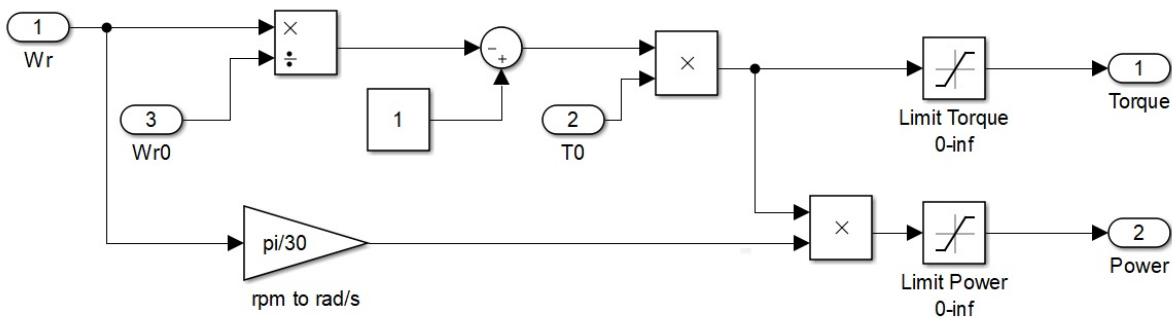
Figure A.7.4 Speed to power/torque output block

Finally, Eq. (3.3) is used to create the air consumption block as shown below:
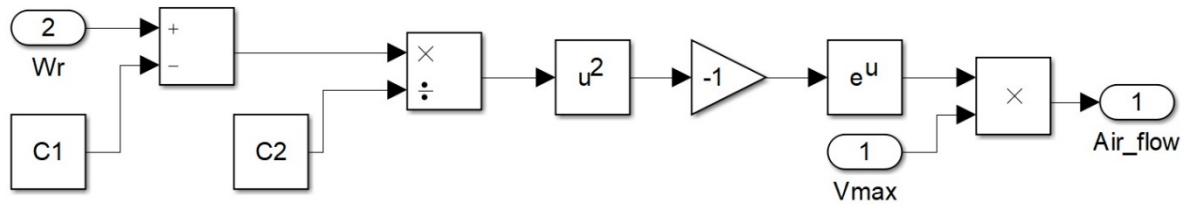
Figure A.7.5 The block of air consumption

Appendix B   Thermodynamic analysis of the air motor conversion efficiency

In order to calculate the efficiency of the air motor conversion, the first and second laws of thermodynamics are applied to an open-loop system. The elementary energy (δw_a) of a unit mass of air is expressed as follows [7], [12], [14]

$$\delta w_a \leq -dh + T_a ds \tag{B.1}$$

Where dh defines the change in specific enthalpy while ds is the change in specific entropy. By integrating the elementary energy in Eq. B.1 from the motor input to output conditions, the specific work (w_a) is presented as

$$w_a \leq (h_i - h_o) - T_s(s_i - s_o) \tag{B.2}$$

Where h_i and s_i define the specific enthalpy and the specific entropy at the input condition, respectively, while h_o and s_o are the specific enthalpy and the specific entropy at the output condition, respectively. In terms of an ideal gas, the change in enthalpy and entropy are expressed by:

$$h_i - h_o = c_p(T_i - T_o) \tag{B.3}$$

$$s_i - s_o = c_p \ln\left(\frac{T_i}{T_o}\right) - R \ln\left(\frac{p_i}{p_a}\right) \tag{B.4}$$

Substituting Eq. (B.3) and Eq. (B.4) into Eq. (B.2) gives:

$$w_a \leq RT_a \left[\ln\left(\frac{p_i}{p_a}\right) + \frac{\gamma}{\gamma-1}\left(\frac{T_i - T_o}{T_a} - \ln\left(\frac{T_i}{T_o}\right)\right)\right] \tag{B.5}$$

In this study, isothermal condition is assumed. It means that the input temperature equals to the ambient temperature $(T_i = T_a)$. Thus, Eq. (B.5) can be rewritten to provide the maximum energy as:

$$w_a = RT_i \left[\ln\left(\frac{p_i}{p_o}\right) + \frac{\gamma}{\gamma-1}\left(1 - \frac{T_o}{T_i} - \ln\left(\frac{T_i}{T_o}\right)\right)\right] \tag{B.6}$$

Where R denotes the gas constant, T_o and T_i are the temperatures, p_i and p_o are the pressures and γ is the ratio of the specific heat that equal to c_p/c_v. The compressed air power $(\dot{w}_a)$ is achieved by multiplying the specific energy (w_a) by the mass flow rate $(\dot{m}_a)$. The continuity equation is applied to the motor for obtaining the mass flow rate $(\dot{m}_a)$ as:

Appendix B

$$\frac{dm_a}{dt} = \dot{m}_a = \rho \dot{V} = \frac{p_i}{RT_a}\dot{V}_i = \frac{p_a}{RT_o}\dot{V}_a \tag{B.7}$$

In practice, the volumetric flow rate is measured at the output condition. Thus, the equation of the mechanical power is given by:

$$\dot{W}_a = w_a \dot{m}_a = p_a \dot{V}_a \frac{T_i}{T_o}\left[\ln\left(\frac{p_i}{p_a}\right) + \frac{\gamma}{\gamma-1}\left(1 - \frac{T_o}{T_i} - \ln\left(\frac{T_i}{T_o}\right)\right)\right] \tag{B.8}$$

Given the high motor speed, the air expansion in adiabatic cycle is considered. Hence, the isentropic process relation $(T_i/T_o) = (p_i/p_a)^{\gamma-1/\gamma}$ is introduced into Eq. (B.8) that can be rewritten by:

$$\dot{w}_a = \frac{\gamma}{\gamma-1} p_a \dot{V}_a \left[\left(\frac{p_i}{p_a}\right)^{\frac{\gamma-1}{\gamma}} - 1\right] \tag{B.9}$$

Finally, the real time pneumatic-to mechanical conversion efficiency (η_{am}) is derived from Eq. (2.5) and Eq. (B.9) as:

$$\eta_{am} = \frac{\dot{W}_m}{\dot{W}_a} = \frac{T_0(p_i)\frac{\pi}{30}\left(\omega_r - \frac{\omega_r^2}{\omega_{ro}(p_i)}\right)}{\frac{\gamma}{\gamma-1}p_a \dot{V}_a\left[\left(\frac{p_i}{p_a}\right)^{\frac{\gamma-1}{\gamma}} - 1\right]} \tag{B.10}$$

As can be seen clearly, in Eq. (B.10), there are three main characteristics that influence the air motor efficiency, namely stall torque (T_0), free speed (ω_{ro}) and the pressure ratio $\left(p_i/p_a\right)$. In order to achieve high efficiency, the air motor should be applied with a high stall torque as well as high free speed in order to tune the speed ratio $\left(\omega_r^2/\omega_{ro}\right)$ to be close to zero. The pressure ratio affects the air consumption in that low-pressure ratio implies less air consumption, which leads to high conversion efficiency.

Appendix C   System parameters

C.1   The air motor model

Parameters	Value
Stall torque coefficient, C_{t1}	0.3732
Stall torque coefficient, C_{t2}	0.04733
Free speed coefficient, C_{n1}	-6782
Free speed coefficient, C_{n2}	-1.08
Free speed coefficient, C_{n3}	4783
Maximum air flow coefficient, C_1	4156
Maximum air flow coefficient, C_2	5487

C.2   The PM-DC generator

Parameters	Value
Generator armature resistance, r_{ag}	0.484 Ω
Inductance of the generator, L_{ag}	585 µH
Torque constant, K_e	0.0691 N.m/A
Back EMF constant, K_m	0.086 V.s/rad
Total moment of inertia, J_t	8.31×10^{-5} kg.m²
Viscous friction coefficients, B_t	0.0055 N.m.s/rad

C.3   The boost and bidirectional converters

Parameters	Value
Inductance of the converter, L	5 mH
Capacitance of the converter, C_o	2000 µF
Resistive load of the converter, R_L	10 Ω

Minimum inductor current, I_m	1 A
MOSFET switching frequency, f	100 kHz
Sampling frequency, f_z	200 kHz

C.4 The ideal gas parameters

Parameters	Value
Pressure, P	20 bar
Temperature, T	298 K
Specific gas constant, R_g	287 J/(kg. K)
Compressor's efficiency, η_c	85 %

C.5 The PV panel

Parameters	Value
Open-circuit voltage, V_{oc}	53.2 V
Short-circuit current, I_{sc}	6.03 A
Temperature coefficient, k_i	0.055%/°C
Temperature coefficient, k_v	-0.235%/°C
Electron charge, q	$1.6 \cdot 10^{-9}$ C
Boltzmann's constant, k	$1.38 \cdot 10^{-23}$ J/K
Ideality factor, n	1.1
Band-gap energy of Si solar cell, E_g	1.10 eV
Series resistance, R_s	0.001 Ω
Parallel resistance, R_{sh}	300 Ω
Reference temperature, T_{ref}	298 K
Module area, A	1.26 m²
Quantity per panel, N_s	40 pcs.
Module efficiency, η_{pv}	19.8 %

Appendix D   Matlab/Simulink implementation

D.1   Controllers

D.1.1   Speed regulator controller
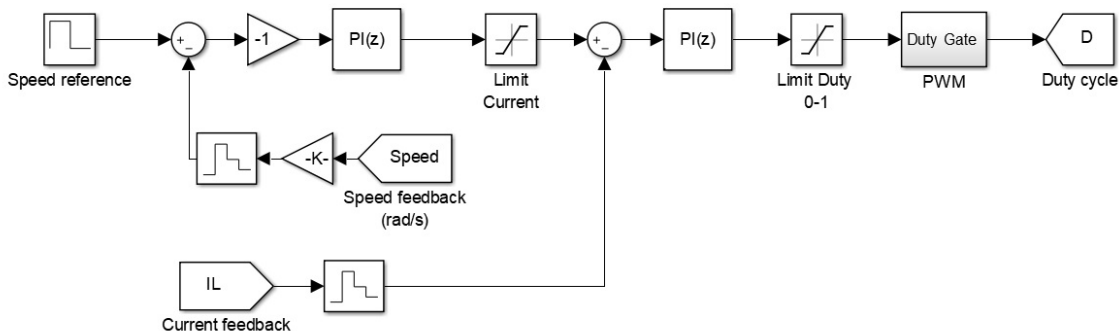
Figure D. 1 Speed regulator controller

D.1.2   Matlab script

```
clear all
close all
clc

%%%%%%%%%%%%%%%%%%%%%%%%%%%%%%%%%%%%%%%%%%%%%%%%%%%%%%%%

Gamma = 1.4;
Pa = 1.01325e5;

%%%%%%%%%%%%%%%%%%%%%%%%%%%%%%%%%%%%%%%%%%%%%%%%%%%%%%%%
% DC Generator maxon parameters 24V, 3090 rpm, 250W
%%%%%%%%%%%%%%%%%%%%%%%%%%%%%%%%%%%%%%%%%%%%%%%%%%%%%%%%
Rag = 0.28;                 %(Ohm)
Lag = 0.369e-3;             %(H)
Ke  = 136e-3;               %(Nm/A)
Km  = 0.45;                 %(V-sec/red)
J   = 0.000476;             %(kg-m^2)
Bt  = 0.0663;               %(N-m-s/rad)

%%%%%%%%%%%%%%%%%%%%%%%%%%%%%%%%%%%%%%%%%%%%%%%%%%%%%%%%
% Air motor model parameters
%%%%%%%%%%%%%%%%%%%%%%%%%%%%%%%%%%%%%%%%%%%%%%%%%%%%%%%%
```

Appendix D

```matlab
Ct1 = 0.3732;              %Stall torque coefficient

Ct2 = 0.04733;             %Stall torque coefficient

Cn1 = -6782;               %Free speed coefficient

Cn2 = -1.08;               %Free speed coefficient

Cn3 = 4783;                %Free speed coefficient

Ca1 = 1.701;               %Air flow coefficient

Ca2 = -1.375;              %Air flow coefficient

C1  = 4156;                %Maximum air flow coefficient

C2  = 5487;                %Maximum air flow coefficient

%%%%%%%%%%%%%%%%%%%%%%%%%%%%%%%%%%%%%%%%%%%%%%%%%%
% Boost converter parameters
%%%%%%%%%%%%%%%%%%%%%%%%%%%%%%%%%%%%%%%%%%%%%%%%%%

fs = 100e3;

Ts = 1/fs;                 %switching frequency

Tsz = 1/200e3;             %sampling frequency

Vin = 20;                  %Input Voltage

Vout = 230;                %Output Voltage

iL = 10;

Delta_iL = 1;              %@10% of full load

Delta_v = 5;               %@10% of full load

d =(Vout-Vin)/Vout;        %Voltage ratio of Boost converter = 0.6

L = (Vin*(Vout-Vin))/(fs*Delta_iL*Vout);       % inductance

C = (iL*(Vout-Vin))/(fs*Delta_v*Vout);         % capacitance

rL = 0.01;                 %Internal inductor resistance

rC = 0.05;                 %Internal capaacitor resistance

R = (Vout^2)/250;          %Maximum load 250W

Cf = 33e-6;                %Filter

%%%%%%%%%%%%%%%%%%%%%%%%%%%%%%%%%%%%%%%%%%%%%%%%%%%%%%%%%%%%%%%%%%%%%%
% Tranfer function of speed regulation with boost converter in
% small signal state space model
%%%%%%%%%%%%%%%%%%%%%%%%%%%%%%%%%%%%%%%%%%%%%%%%%%%%%%%%%%%%%%%%%%%%%%
% Defining parameters as Lt, Ta, M and Im
Lt = Lag+L;                %Total inductors

M = 1*((R*(1-d))/(Rag+(R*(1-d)^2))); %Duty cycle ratio
```

```matlab
%%%%%%%%%%%%%%%%%%%%%%%%%%%%%%%%%%%%%%%%%%%%%%%%%%%%%%%%%%%%%%%%%%%%%%%%
% The transfer function of the storage equipment and the dynamic
% DC machine
%%%%%%%%%%%%%%%%%%%%%%%%%%%%%%%%%%%%%%%%%%%%%%%%%%%%%%%%%%%%%%%%%%%%%%%%
Gst = tf([0 R],[R*C 1]);          %The storage RLC
Gd = tf(1,[J Bt]);                 %The dynamic DC machine


%%%%%%%%%%%%%%%%%%%%%%%%%%%%%%%%%%%%%%%%%%%%%%%%%%%%%%%%%%%%%%%%%%%%%%%%
% State space average
%%%%%%%%%%%%%%%%%%%%%%%%%%%%%%%%%%%%%%%%%%%%%%%%%%%%%%%%%%%%%%%%%%%%%%%%
G1 = ((R/(M^2))-Rag)/Lt;

G2 = (Lt+(Rag*R*C))/(R*C*Lt);

G3 = (Rag+(R/(M^2)))/(R*C*Lt);

G4 = Vin/(Rag+(R/(M^2)));

G5 = tf([1 G1],[1 G2 G3]);

Gvd11 = G4*G5;                     %Duty cycle to output voltage open-loop tf.

G6 = 2/(R*C);

G7 = tf([1 G6],[1 G2 G3]);

Gid11 = G4*G7;                     %Duty cycle to inductor current open-loop tf.

G8 = 1/Lt;

G9 = Rag/(Lt^2);

Gig = tf([G8 G9],[1 G2 G3]);%Input voltage to inductor current open-loop
tf.

Gvi = tf([1 G6],[1 G1]);%output voltage to inductor current open-loop tf.
%%%%%%%%%%%%%%%%%%%%%%%%%%%%%%%%%%%%%%%%%%%%%%%%%%%%%%%%%%%%%%%%%%%%%%%%
% Filter design is estimated using Matlab tool in Filter Design& Analysis
% Tool for eliminating aliasing wave form which are generated by a high
% switching and auxilary power supply.
Hf = tf(10*pi,[1 10*pi]);         %cut off 5 rad/s

Hfz = c2d(Hf,Tsz,'zoh');
%%%%%%%%%%%%%%%%%%%%%%%%%%%%%%%%%%%%%%%%%%%%%%%%%%%%%%%%%%%%%%%%%%%%%%%%
% Open loop transfer function of inner loop is
%%%%%%%%%%%%%%%%%%%%%%%%%%%%%%%%%%%%%%%%%%%%%%%%%%%%%%%%%%%%%%%%%%%%%%%%
Gip_o = (Gid11)/(1+(Gvi*Gst)+(M*Km*Ke*Gig*Gd));  %To normalise the order
of transfer function
```

Appendix D

```matlab
Gip = minreal(Gip_o,Ts);

Gipz = c2d(Gip,Tsz,'zoh');

Gipz = minreal(Gipz,Ts);


% The PI of current loop is designed using command sisotool(Gipz*Hfz)

OPT_i = pidtuneOptions('CrossoverFrequenc',2.63e4,'PhaseMargin',40);

Gciz = pidtune(Gipz*Hfz,'pi',OPT_i);

Kpiag1 = Gciz.Kp;

Kiiag1 = Gciz.Ki;

Gci = d2c(Gciz,'zoh');

%%%%%%%%%%%%%%%%%%%%%%%%%%%%%%%%%%%%%%%%%%%%%%%%%%%%%%%%%%%%%%%%%%%%%%%%%%%%

% Open loop transfer function of outerloop with the PI controller of

% inner loop feedback is

%%%%%%%%%%%%%%%%%%%%%%%%%%%%%%%%%%%%%%%%%%%%%%%%%%%%%%%%%%%%%%%%%%%%%%%%%%%%

Gwp = (Gci*Gid11*Ke*Gd*M)/(1+(Gvi*Gst)+(Gci*Gid11*Hf)+(M*Km*Ke*Gig*Gd));

Gwp = minreal(Gwp,Ts);

Gwpz = c2d(Gwp,Tsz,'zoh');

OPT_w = pidtuneOptions('CrossoverFrequenc',4.38e4,'PhaseMargin',60);

Gcwz = pidtune(Gwpz,'pi',OPT_w);

Kpw1 = Gcwz.Kp;

Kiw1 = Gcwz.Ki;

%%%%%%%%%%%%%%%%%%%%%%%%%%%%%%%%%%%%%%%%%%%%%%%%%%%%%%%%%%%%%%%%%%%%%%%%%%%%
```

D.1.3   MPPT
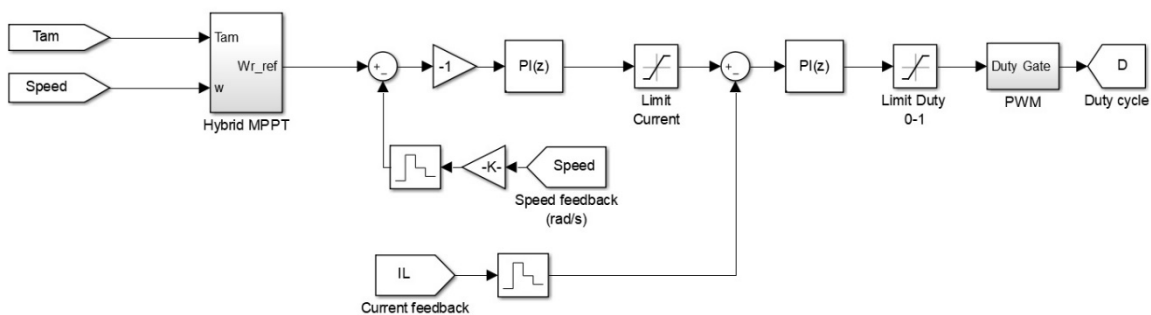

Figure D. 2 MPPT speed controller

126
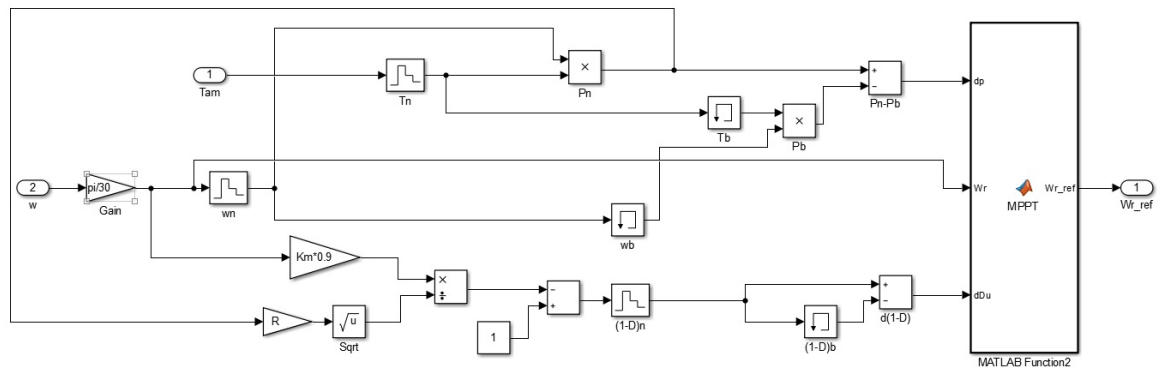
Figure D. 3 Hybrid MPPT block

D.1.4 MPPT Matlab script

```matlab
function Wr_ref = MPPT(dp,Wr,dDu)

Delta_f = 5;

Delta_c = 20;

sigma = 1;

if abs(dp)<sigma

if dp==0

Wr_ref = Wr;

else

if dp>0

if dDu<0

Wr_ref = Wr+Delta_f;

else

Wr_ref = Wr-Delta_f;

end

else

if dDu<0

Wr_ref = Wr-Delta_f;

else

Wr_ref = Wr+Delta_f;

end

end

end

else
```

```
if dp>0
if dDu<0
Wr_ref = Wr+Delta_c;
else
Wr_ref = Wr-Delta_c;
end
else
if dDu<0
Wr_ref = Wr-Delta_c;
else
Wr_ref = Wr+Delta_c;
end
end
end
```

D.1.5   Voltage controller
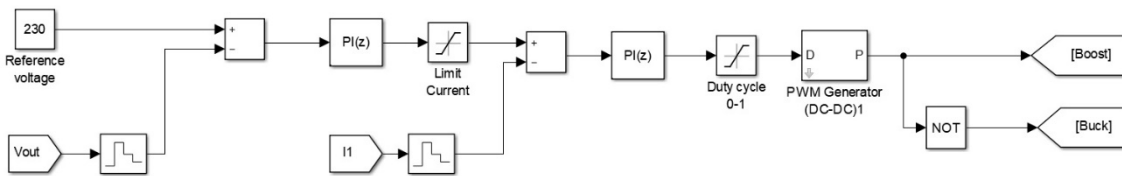
Figure D. 4 Voltage controller